Title
All-inorganic perovskite by vapor phase deposition for optoelectronic applications

Author
Wang, Yiliu

Publication Date
2019

UNIVERSITY OF CALIFORNIA

Los Angeles

All-inorganic perovskite by vapor phase deposition for optoelectronic applications

A dissertation submitted in partial satisfaction of the
requirements for the degree Doctor of Philosophy
in Chemistry

by

Yiliu Wang

2019

ABSTRACT OF THE DISSERTATION

All-inorganic perovskite by vapor phase deposition for optoelectronic applications

by

Yiliu Wang

Doctor of Philosophy in Chemistry

University of California, Los Angeles, 2019

Professor Xiangfeng Duan, Chair

All-inorganic perovskites have attracted tremendous interest for their tunable optical properties and remarkable stability when compared with its hybrid counterpart. Although considerable efforts have been devoted to synthesizing micro-crystalline domains and various nanostructures, it remains a considerable challenge to produce high-quality monocrystalline thin films that are indispensable for functional electronics and optoelectronics. Furthermore, due to the fragility of metal halide perovskites, it remains a standing challenge to use conventional lithography to create reliable electrical contacts, rendering the intrinsic electrical transport properties of such perovskite materials are often seriously convoluted/plagued by poor electrical contacts. Starting from the vapor phase deposition of cesium lead halide $CsPbX_3$ (X=Cl, Br, I) microplates, we demonstrated the growth of large-area monocrystalline all-inorganic perovskite thin films on muscovite mica. We show highly oriented $CsPbBr_3$ square microplates can be readily grown on the (001) surface of muscovite with an epitaxial relationship of $CsPbBr_3$-(001) paralleled to muscovite-(001), $CsPbBr_3$-[100] paralleled to muscovite-[100] and $CsPbBr_3$-[010] paralleled to muscovite-[010], which eventually merge together to form a continuous monocrystalline thin film. Time resolved photoluminescence (TRPL) decay measurements give a carrier lifetime of 170 ns, considerably longer than that in spin-coated thin films and well comparable to that in the highest quality bulk crystals. Aiming to resolve the problem of poor electrical contacts, we have further developed a simple physical transfer approach to create high-quality van der Waals (vdW) contacts, where the prefabricated thin film gold electrodes are directly laminated onto the perovskite thin films with minimum interfacial damage to produce electrical contacts for functional devices. The electrical and photoelectrical transport studies demonstrated an extraordinary photocurrent gain exceeding 10^6. The van der Waals contacts enable not only accurate measurements at room temperature but also the exploration of electrical properties at cryogenic conditions. A record-high carrier mobility exceeding 2,000 cm^2/Vs has been achieved at 80 K and a quantum interference induced weak localization behavior in halide perovskite materials with a coherence length up to 49 nm has also been revealed for the first time by magnetotransport studies at 3.5 K. The growth of large-area high-quality perovskite thin films and the integration of the damage-free metal integration approach mark important steps for both the fundamental investigation and potential applications of the perovskite materials in integrated optoelectronics.

The dissertation of Yiliu Wang is approved.

Jeffrey I. Zink

Richard B. Kaner

Yu Huang

Xiangfeng Duan, Committee Chair

University of California, Los Angeles

2019

Dedicated to my farther Changlong Wang, mother Liqun Liu,

for their unconditional love and support,

to my families and friends,

for their encouragement and enlightenment.

Table of contents

List of Figures

Chapter 4. Electrical transport probing carrier and photocarrier dynamics in lead halide perovskite thin films with van der Waals contacts……………………………………………53

Acknowledgement

It has been my honor to be a graduate student in the Department of Chemistry and Biochemistry, University of California, Los Angeles. The past five years have been a significant period when I learned a lot in my life. Life of PhD is not easy but finally I made it. I would like to take this opportunity to express my appreciation to the people who helped me to pull through and make these five years memorable.

First of all, I would like to thank my advisor, Prof. Xiangfeng Duan, for his invaluable guidance on my research. Throughout my long journey as a graduate student, I have always been impressed by his profound knowledge and keen insight to find interesting scientific problems. His passion and faith in science and work is incomparable which leads to a great success as both scientist and mentor. That he picked up me from CSST research program, assigned me research topic when I was undergraduate and eventually enrolled me as his student is what I would appreciate in my whole life. I admire his constant enthusiasm for exploring new things, and his persistence in thinking about crazy ideas and bringing them into reality. It has been a great privilege to join his lab and learn from such a creative, enthusiastic and inexhaustible mind. For the five years, he informed me of his expectation for graduate student, “try whatever you can to make your research complete no matter how difficult it is”, which has been encouraging and impressing me a lot.

I would like to thank the members on my thesis committee, Prof. Jeffrey Zink, Prof. Richard Kaner and Prof. Yu Huang, for reading my thesis and providing valuable feedback. They have been of great help on my oral qualification exam, 4th year meeting, final dissertation and the career plan.

I have enjoyed working with an outstanding group of highly motivated people. In particular, Dr. Zhong Wan and Dr. Qi Qian taught me plenty of knowledge of condensed matter physics. Dr. Zhaoyang Lin showed me the true meaning of hard working and being the true expert of one's own research field. Dr. Gongming Wang taught me many experimental details in electrochemistry and helped me a lot in many aspects in both science and life, for which I have been always grateful. I admire Dr. Chuancheng Jia for his outstanding research capability and respectful working attitude. The collaboration with him in several single-molecule device research projects did expand my scope and bring me more passion in the work. Dr. Yuan Liu has always been a source of rich experience in research. Dr. Jian Guo, Peiqi Wang and Dr. Yang Liu taught me electrical measurement technologies.

Dr. Rui Cheng and Dr. Mufan Li helped me to quickly adapt to the new environment when I first came here. Dr. Chain Lee is a good friend of mine and helped me a lot on the career plan. Dr. Dehui Li is a very nice person who helped me quite much in my experiment. I would thank Dr. Mengning Ding, an excellent researcher, for his opinion and comment on my research. Dr. Benjamin Papandrea, Dr. Boris Volosskiy, Dr. Udayabagya Halim, Dr. Zipeng Zhao introduced me to the group and unselfishly helped me. I also want express my appreciation to Dr. Peng Chen, Chengzhang Wan, Guangyan Zhong, Sungjoon Lee, Bocheng Cao, Frank Song, Dan Zhu, Dan Bauman and Wang Xue, Jin Huang.

Last but not least, I am enormously grateful to my parents, my families and my friends for their constant encouragement and support. Especially I want to express my great appreciation to my parents, Changlong Wang and Liqun Liu for the understanding that I was not able to go back to China to meet them for these years.

VITA

2014 B.S. in Materials Science and Engineering, Zhejiang University, Hangzhou

2015 M.S. in Chemistry, University of California, Los Angeles

2016 Excellence in Second Year Academics and Research

2018 Dissertation Year Fellowship

Chapter 1. Introduction

1.1 The emerging of hybrid perovskite as a class of unique optoelectronic materials

Perovskite, originating from the Russian mineralogist Lev Perovski, firstly referred to a calcium titanium oxide mineral composed of $CaTiO_3$. It is also applied to the class of compounds which have the same type of crystal lattice as $CaTiO_3$. The oxide perovskites have been investigated for over 150 years, while the halide perovskites draw the attentions of researchers since its first application in photovoltaic field, which was reported in 2009[1]. As a new class of semiconductors, it gained plenty of applications in photovoltaic, light emitting and radiation detection fields. Halide perovskites share the same crystal structure and chemical formula ABX_3 to oxide perovskite. Cation A, which is usually methylammonium ion (MA^+) or formamidinium ion (FA^+), occupies the corner sites; cation B, usually the Pb^{2+} or Sn^{2+}, takes up the body center; while all the halogen anions are at the face center. The BX_6^{4-} octahedron forms the framework and the A cations fill between to balance the charge and stabilize the whole lattice structure (**Figure 1.1**)[2].

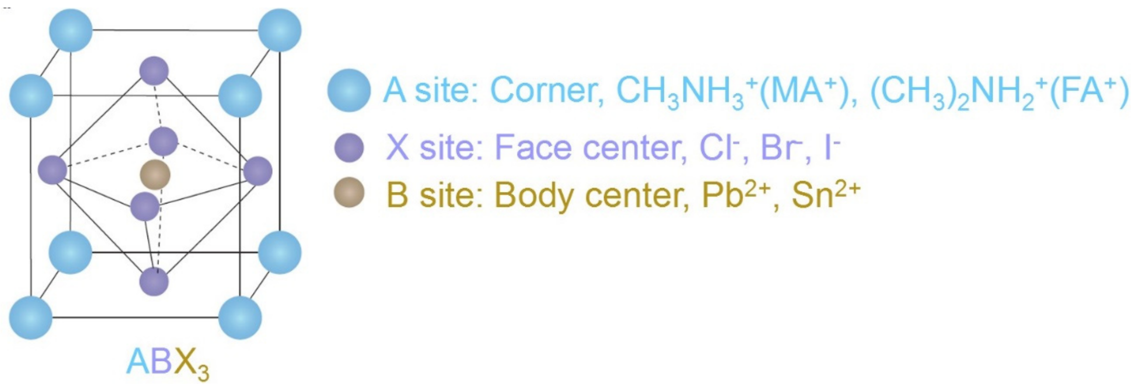

Figure 1.1. Crystal structure of typical metal halide perovskite material. Cation A is at the corner site, cation B is at the body center site and anion X is at the face center site. Adapted from Ref. 2.

Furthermore, the tolerance factor *t* is calculated by taking all radiuses of A (r_A), B (r_B) and X (r_X) ions into consideration, shown in the following equation:

$$t = \frac{r_A + r_X}{\sqrt{2}(r_B + r_X)} \qquad (1)$$

Ideally, we want the tolerance factor t to fall into the range of 0.9 to 1 so that a perovskite phase with unique optoelectronic properties is able to form, which raises requirements to the radiuses on ions. This also explains why the options of ions to from the perovskite crystal are limited.

Fortunately, halogen ions are able to fit in the perovskite lattice and the composition of them can vary. For the perovskite semiconductors with direct band gap, the energy band gap is mainly determined by the anion composition, which is indicated by the wavelength of emission light (**Figure 1.2**)[2]. Therefore, by alloying the halogen ions, we have the ability to tune the band gap of perovskites to cover the entire visible light region. The band gap tunability, together with the high charge carrier mobility, long carrier lifetime and high tolerance to defects, makes the perovskites achieve excellent performances for optoelectronic applications.

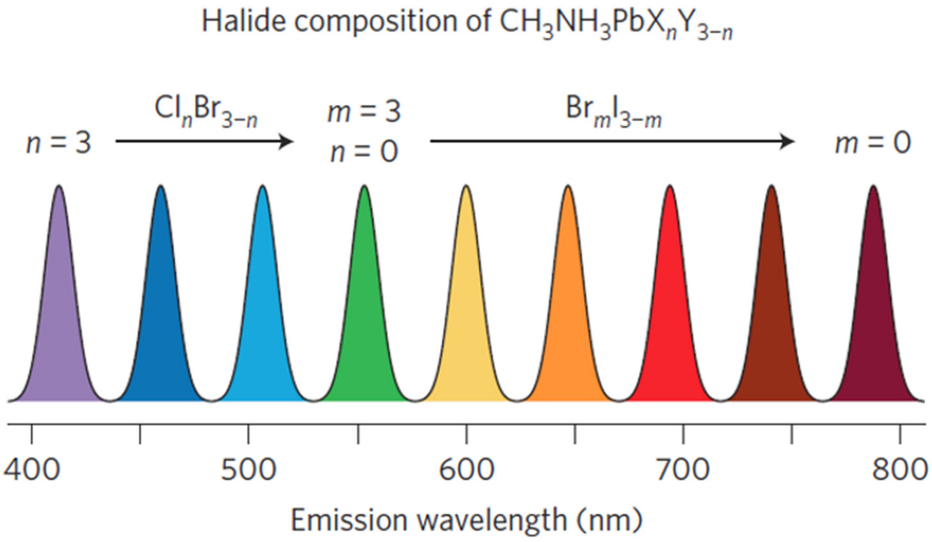

Figure 1.2. Different emission wavelengths of perovskites with different anion composition. The emission light starts from ~400 nm and end at ~800 nm, covering the whole visible light range. Adapted from Ref. 2.

The application of metal halide perovskite was firstly reported in 2009, as an absorber utilized in dye sensitized solar cell (DSSC) -like solar cell with power conversion efficiency is about 3%[1]. Later on, perovskite solar panel with efficiency exceeding 15% has been reported. The state-of-art efficiency reached 23.1% recently (*NREL Efficiency Chart*), which is comparable to that of monocrystalline silicon solar panel. At the meantime, light emitting devices have been investigated as well. For example, both light emitting diode (LED) based on $MAPbI_3$ emitting red light and LED based on $CsPbBr_3$ emitting green light have been reported with peak quantum efficiency exceeding 20%[3, 4]. Besides, the metal halide perovskites bulk crystals were utilized in the field of high energy radiation detection. For instance, gamma-ray detector has been fabricated with $MAPbI_3$ bulk crystal owing to the high charge carrier mobility-lifetime product, low dark density, low trap density and high absorptivity from lead and iodine atoms of perovskite[5]. X-ray imaging has been realized as well with the utilization of $MAPbI_3$ thick film in combination with a conventional thin film transistor substrate[6].

1.2. Instability of hybrid perovskite

In spite of the eye-catching demonstrations, the instability is still a severe problem preventing the hybrid perovskite from practical applications. Due to the existence of organic cations in the lattice, the hybrid perovskite is readily to react with the moisture in atmosphere, and decomposes into lead halide[7].

Besides, the hybrid perovskite will also decompose at relatively high temperature because of the volatilization of organic cations[8]. This thermal instability challenges the practical application of perovskite solar cell since the temperature of solar panel could readily reach 80 °C under strong light illumination. High-quality packaging technique could effectively isolate the perovskite from moisture in the atmosphere while it seems the solution to the thermal instability relies on the improvement of materials themselves.

Furthermore, light-induced phase segregation frequently happens in the mixed-anion perovskites[9] that meets the bandgap requirements well. Domains with different bandgap form after phase segregation, inducing barriers to the charge transport which is detrimental to the practical applications.

A solution of replacing the organic cation with Cs^+ was proposed and the radius of Cs^+ meets the requirements of tolerance factor. Both the moisture stability and thermal stability have been improved a lot. And the tolerance to high temperature of all-inorganic perovskite enables a high temperature vapor phase deposition. The addition of Cs+ will increase the entropy of the whole system so that stabilize the perovskite to prevent light-induced phase segregation under illumination.

1.3. Device fabrication on metal halide perovskite materials

Metal halide perovskites are generally soluble in various solvents and incompatible with typical lithography processes that are necessary for microscopic device fabrications. Therefore, shadow mask deposition is usually utilized to fabricate electrodes on perovskites. While metal halide perovskites are highly delicate and prone to degradation during the conventional vacuum metal deposition processes[10-13], which typically involve high-energy atom/cluster bombardments and strong local heating that could seriously damage the underlying halide perovskite materials.

1.4. Characterization of charge carrier transport properties of perovskites

Since it remains a standing challenge to use conventional lithography to fabricate reliable electrical contacts on halide perovskites, the intrinsic electrical transport properties of such perovskite materials could not be accurately probed with direct electrical measurements and have not been fully understood so far. Although there are some measurements being established to characterize the electrical properties of metal halide perovskites, the limitations of them are apparent and require complicated analysis to derive parameters properly.

For example, the space charge limited current (SCLC) model based on Mott-Gurney law are usually used to estimate the carrier density and mobility of various metal halide perovskites due to the simplicity of the device geometry with perovskite layer sandwiched by two metal electrodes, while this model is not valid for deriving the carrier density and mobility without several critical assumptions which are hard to achieved in the reported measurements. For instance, the contacts are required to be Ohmic, or the Mott-Gurney law cannot be directly used without accounting for non-ideal injection. Even worse for the typical perovskite devices, substantial current-voltage (I-V) hysteresis loop emerging under large bias voltage could also further convolute with SCLC, bringing additional complications in interpreting the I-V characteristics and compromising the accuracy of the SCLC modeling and reliability of the relevant derivations[14-16]. Furthermore, it's difficult to establish the relationships of light illumination and carrier dynamics (generation/recombination and transport) with SCLC method since the measurements are conducted without light illumination, though such relationships are critical in most optoelectronic applications of perovskites. On the other hand, the non-contact spectroscopic techniques based on tera Hertz/microwave conductivity have been explored to probe the basic charge carrier behavior without the contact complication, although these approaches only give an indirect evaluation of local carrier dynamics and often require complex mathematic modeling and derivations[17-19]. A more direct electrical probing long-range charge transport properties is desirable but remains challenging to date.

Hall measurements, which have been well established for several decades, represent the most direct and preferred method for probing charge carrier behavior with minimum derivations and reduced uncertainties, as well demonstrated and adopted for the evaluation of most conventional semiconductors such as Si and GaAs[20-22]. Despite some pioneering efforts in Hall measurements on perovskite with shadow-mask evaporation defined electrodes, these studies are usually complicated and sometimes dictated by the excessive contact resistance, raising uncertainties on the accuracy of the Hall measurements[23, 24]. For example, large error would be introduced if there exists high contact resistance comparable to the internal resistance of voltmeter, which usually happens in devices based on metal halide perovskites.

1.5. Overview of this dissertation

In this dissertation, I will mainly focus on the vapor phase deposition of all-inorganic metal halide perovskites for optoelectronic applications and the method on conducting reliable electrical measurements on the platform of vapor phase deposited all-inorganic perovskite.

In Chapter 2, we report a single-step chemical vapor deposition approach for the growth of $CsPbX_3$ micro crystals. Optical microscopy studies show that the resulting perovskite crystals predominantly adopt a square microplate morphology. Powder X-ray diffraction studies show highly crystalline nature of the resulting crystals, with $CsPbCl_3$, $CsPbBr_3$ and $CsPbI_3$ showing the tetragonal, monoclinic and orthorhombic phases, respectively. Scanning electron microscopy and atomic force microscopy studies show that the resulting microplates exhibit well-faceted structures with lateral dimensions on the order of 10-50 μm, thickness around 1 μm, and ultra-smooth surface, suggesting the absence of obvious grain boundary and a single crystalline nature of the individual microplate. Photoluminescence (PL) image and spectroscopy studies show uniform and intense emission consistent with the expected band edge transition. Additionally, PL images show brighter emission around the edge of microplates, demonstrating the wave-guiding effect in the crystals of high quality. With well-defined geometry and ultra-smooth surface, the square microplate structure can function as whisper gallery mode cavity with a quality factor up to 2863 to support laser emission at room temperature. Lastly, we demonstrated such microplates can be readily grown on a variety of substrates, including silicon, graphene and other two-dimensional materials such as molybdenum disulfide, which can readily allow us to construct heterostructure optoelectronic devices, including a graphene/perovskite/graphene vertical stack photodetector with photoresponsivity > 10^5 A/W (corresponding to a gain of 3.9×10^5). The extraordinary optical properties of $CsPbX_3$ microplates, combined with the ability to be grown on diverse materials to form functional heterostructures, will open up exciting opportunities for broad optoelectronic applications.

In Chapter 3, we demonstrated the first growth of large-area monocrystalline all-inorganic perovskite thin film for functional electronics and optoelectronics. We show highly aligned micro-crystal domains can be readily grown on muscovite mica substrate using a chemical vapor deposition process, which can further grow and eventually merge into a large-area monocrystalline $CsPbBr_3$ thin film with an excellent optical quality. With the excellent chemical stability, we show that $CsPbBr_3$ thin film is compatible with standard lithography, making it a potential platform for the massive integration of functional electronic and optoelectronic devices. We further demonstrate that an electron beam lithography patterning approach can be used to enable selective anion-exchange to produce lateral heterojunctions with a clear rectification behavior. The capability to grow $CsPbBr_3$ monocrystalline thin film and to conduct the selective anion-exchange to form well-defined heterostructures creates a robust material platform for both the fundamental investigation of their optoelectronic properties and potential applications in integrated optoelectronic systems.

In Chapter 4, we report a vdW integration approach to realize high-performance contacts on monocrystalline halide perovskite thin films with minimum interfacial damage and atomically clean interface. The transport studies show that the vdW contacts greatly reduce the contact resistance by 2-3 orders of magnitude when compared with the deposited contacts at both the room and cryogenic temperatures, allowing systematic electrical studies to probe their transport properties in a wide temperature range. The photoelectrical transport studies demonstrate a record-high Hall mobility exceeding 2,000 cm^2/Vs, a polaron-protected ultralow bimolecular recombination rate of 3.5×10^{-15} cm^3/s, and a record-high photocurrent gain $> 10^6$ in perovskite thin films. Furthermore, enabled by high quality vdW contacts, magnetotransport studies reveal a quantum interference induced weak localization behavior with a phase coherence length up to 49 nm at 3.5 K, comparable to black phosphorus or InSe at a similar carrier density, suggesting the "soft-lattice" halide perovskites as an exciting class of electronic materials. The growth of monocrystalline perovskite thin films and the damage-free integration of high-quality contacts mark important steps towards unraveling the fundamental transport properties of perovskites and define the technical foundation for exploring new physics in this unique class of "soft-lattice" materials.

1.6. References

1. Kojima, A.; Teshima, K.; Shirai, Y.; Miyasaka, T. *J. Am. Chem. Soc.* **2009,** *131*, 6050-6051.

2. Sutherland, B. R.; Sargent, E. H. *Nat. Photonics* **2016,** *10*, 295.

3. Lin, K.; Xing, J.; Quan, L. N.; de Arquer, F. P. G.; Gong, X.; Lu, J.; Xie, L.; Zhao, W.; Zhang, D.; Yan, C. *Nature* **2018,** *562*, 245.

4. Cao, Y.; Wang, N.; Tian, H.; Guo, J.; Wei, Y.; Chen, H.; Miao, Y.; Zou, W.; Pan, K.; He, Y. *Nature* **2018,** *562*, 249.

5. Yakunin, S.; Dirin, D. N.; Shynkarenko, Y.; Morad, V.; Cherniukh, I.; Nazarenko, O.; Kreil, D.; Nauser, T.; Kovalenko, M. V. *Nat. Photonics* **2016,** *10*, 585.

6. Kim, Y. C.; Kim, K. H.; Son, D.-Y.; Jeong, D.-N.; Seo, J.-Y.; Choi, Y. S.; Han, I. T.; Lee, S. Y.; Park, N.-G. *Nature* **2017,** *550*, 87.

7. Yang, J.; Siempelkamp, B. D.; Liu, D.; Kelly, T. L. *ACS Nano* **2015,** *9*, 1955-1963.

8. Fan, Z.; Xiao, H.; Wang, Y.; Zhao, Z.; Lin, Z.; Cheng, H.-C.; Lee, S.-J.; Wang, G.; Feng, Z.; Goddard III, W. A. *Joule* **2017,** *1*, 548-562.

9. Bischak, C. G.; Hetherington, C. L.; Wu, H.; Aloni, S.; Ogletree, D. F.; Limmer, D. T.; Ginsberg, N. S. *Nano Lett.* **2017,** *17*, 1028-1033.

10. Zan, R.; Ramasse, Q. M.; Jalil, R.; Georgiou, T.; Bangert, U.; Novoselov, K. S. *ACS Nano* **2013,** *7*, 10167-10174.

11. Spicer, W.; Chye, P.; Garner, C.; Lindau, I.; Pianetta, P. *Surf. Sci.* **1979,** *86*, 763-788.

12. Haick, H.; Niitsoo, O.; Ghabboun, J.; Cahen, D. *J. Phys. Chem. C* **2007,** *111*, 2318-2329.

13. Haick, H.; Ambrico, M.; Ghabboun, J.; Ligonzo, T.; Cahen, D. *Phys. Chem. Chem. Phys.* **2004,** *6*, 4538-4541.

14. Mott, N. F.; Gurney, R. W., *Electronic Processes in Ionic Crystals*. 1940.

15. Murgatroyd, P. *J. Phys. D* **1970,** *3*, 151-156.

16. Mark, P.; Helfrich, W. *J. Appl. Phys.* **1962,** *33*, 205-215.

17. Herz, L. M. *ACS Energy Lett.* **2017,** *2*, 1539-1548.

18. Manser, J. S.; Kamat, P. V. *Nat. Photonics* **2014,** *8*, 737-743.

19. Guo, D.; Bartesaghi, D.; Wei, H.; Hutter, E. M.; Huang, J.; Savenije, T. J. *J. Phys. Chem. Lett.* **2017,** *8*, 4258-4263.

20. Umansky, V.; Heiblum, M.; Levinson, Y.; Smet, J.; Nübler, J.; Dolev, M. *J. Cryst. Growth.* **2009,** *311*, 1658-1661.

21. Green, M. A. *J. Appl. Phys.* **1990,** *67*, 2944-2954.

22. Putley, E.; Mitchell, W. *Proc. Phys. Soc.* **1958,** *72*, 193-200.

23. Chen, Y.; Yi, H.; Wu, X.; Haroldson, R.; Gartstein, Y.; Rodionov, Y.; Tikhonov, K.; Zakhidov, A.; Zhu, X.-Y.; Podzorov, V. *Nat. Commun.* **2016,** *7*, 12253.

24. Yi, H. T.; Wu, X.; Zhu, X.; Podzorov, V. *Adv. Mater.* **2016,** *28*, 6509-6514.

Chapter 2. Vapor phase deposition growth of single-crystalline cesium lead halide microplates and heterostructures for optoelectronic applications

2.1. Introduction

Organic-inorganic hybrid lead halide perovskites have recently re-emerged as an exciting class of materials for low-cost solution processable solar cells[1-5], with a remarkable 23.1% power conversion efficiency achieved in just a few years. Additionally, such perovskite materials have also been explored for a variety of optoelectronic applications including bright light-emitting diodes (LEDs)[6], low-threshold lasers[7], photodetectors[8], and high-sensitivity X-ray detectors[9] with a highly respectable performance. The extraordinary performances of diverse devices made from organic–inorganic perovskites have been attributed to their high charge-carrier mobility[10], long carrier diffusion length[11-13], and high tolerance to defects[14, 15]. Despite their exciting potential and considerable progress to date, organic-inorganic hybrid perovskite-based materials suffer from poor environmental stability and are generally incompatible with typical lithography processes that are necessary for fabricating very complicated optoelectronic devices. Moisture[16], thermal[17], and photon instability[18] hinder the practical applications of this exciting material system. To this end, all-inorganic perovskites (e.g., cesium lead halides: $CsPbX_3$) have been developed and shown to exhibit significantly improved stability. To date, most all-inorganic perovskites have been prepared by a co-evaporation[19, 20] or spin coating process[21], with the resulting films typically showing polycrystalline structures that may contain a large number of undesirable defects and trap states. To probe the intrinsic electronic and optical properties of perovskites and demonstrate the superior optoelectronic performance of perovskite-based materials, it is desirable to produce single crystalline materials[22-25]. Thus, a variety of solution chemical approaches have been developed for the synthesis of $CsPbX_3$ perovskite single crystals with controlled shape and size, including

$CsPbX_3$ quantum dots[26-28], nanowires[29, 30], nanoplates[31-33], and microwires[34, 35]. It has also been shown that the anion composition of $CsPbX_3$ can be systematically tuned by anion exchange to produce perovskites with photoluminescence (PL) emissions covering the entire visible spectrum. Although high quality $CsPbX_3$ crystals have been obtained by wet chemistry methods, the purity or quality of the resulting materials may be complicated by the requirement of solvents, surfactants, or other unintentional uncontrolled impurities in the solution phase. On the other hand, a chemical vapor deposition (CVD) method that is generally utilized to grow high-quality electronic materials, may offer an alternative pathway to high quality all-inorganic perovskite crystals. Although vapor phase synthesis has been applied for hybrid perovskite[36], it has not been sufficiently explored for the growth of $CsPbX_3$ materials until recently[37].

Here we report a single-step CVD growth of $CsPbX_3$ microplates on a variety of substrates, including Si/SiO_2 wafer, reduced graphene oxide, graphene and two-dimensional (2D) semiconductor molybdenum disulfide (MoS_2). Strong PL was obtained from all $CsPbX_3$ microplates with tunable emission in blue, green and red. We further show the $CsPbBr_3$ microplate can function as the gain medium and whisper gallery mode cavity to support lasing emission at room temperature, and demonstrate that graphene/$CsPbBr_3$/graphene heterostructures can be used to construct vertical photodetectors with large photocurrent gain.

2.2. Experimental section

Chemicals. CsCl (>99%), CsBr (>99%), CsI (>99%), $PbCl_2$ (>98%), $PbBr_2$ (>98%), PbI_2 (>98%) were all purchased from Sigma-Aldrich. All the chemicals were used as received without further purification.

Vapor phase deposition system. The growth was conducted in a home-built chemical vapor deposition (CVD) system consisting of a tube furnace (Thermo Scientific Lindberg Blue M) with a 1-inch diameter quartz tube (**Figure 2.1**).

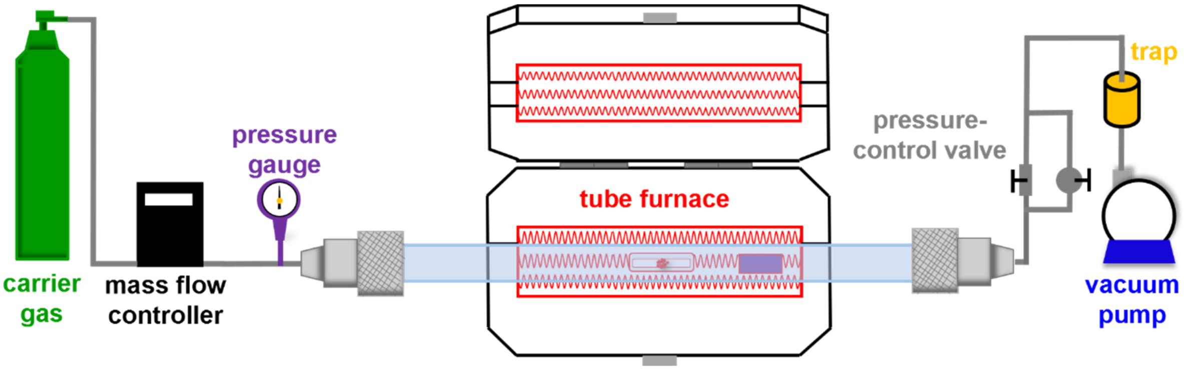

Figure 2.1. Schematic diagram of the CVD system for the deposition. Argon is used as the carrier gas, a mass flow controller (MFC), a pressure gauge, the valve system and a mechanical pump are used to maintain the pressure of the system. The reactant sources evaporate at the center of tube furnace when heating. Vaporized sources will deposit on the substrate at the downstream. The trap is installed to prevent the reactants from entering the vacuum pump.

Deposition of $CsPbX_3$ microplates. The precursor powder (mixed powder of CsCl and $PbCl_2$, CsBr and $PbBr_2$, or CsI and PbI_2 in a 1:1 molar ratio for $CsPbI_3$, $CsPbBr_3$, and $CsPbI_3$, respectively) was placed at the center of the tube furnace under a controlled temperature (550, 600, and 650 °C for $CsPbI_3$, $CsPbBr_3$, and $CsPbCl_3$, respectively). Argon was used as carrier gas at a flow rate of 100 sccm to transport the reactant vapor downstream in the quartz tube. A variety of substrate materials (Si/SiO_2, reduced graphene oxide, patterned CVD graphene, MoS_2, mica, GaN, and glass) were placed at the downstream end (~400 °C) compared to the growth substrate, on which the cooled reactant vapor could nucleate and grow into single crystal microplates. The quartz tube was pumped down to about 10 mbar and flushed with argon for three times to eliminate oxygen and moisture in the tube before ramping up the temperature. The growth was carried out at an optimized pressure (200 mbar for $CsPbI_3$, 130 mbar for $CsPbBr_3$ and $CsPbCl_3$) and maintained at the set temperature for 10 min. The furnace was then cooled naturally to room temperature under a continuous argon flow before the samples were collected.

Characterization. Characterizations were carried out using scanning electron microscopy (SEM, ZEISS Supra 40VP) with energy dispersive spectroscopy (EDAX), powder X-ray diffraction (PXRD, Bruker D8 Discover Powder X-ray Diffractometer) and atomic force microscopy (AFM, Bruker Dimension FastScan Scanning Probe Microscope).

Optical measurement. All the optical and PL images were captured on a home-built microscope system. A xenon light (OLYMPUS U-RX-T) was used as illumination light. A cube equipped with two long pass filters and one dichroic prism was employed to eliminate the influence from the incident light, so that only the emission light was able to reach the CCD (OLYMPUS DP73) where the images were captured (**Figure 2.2**).

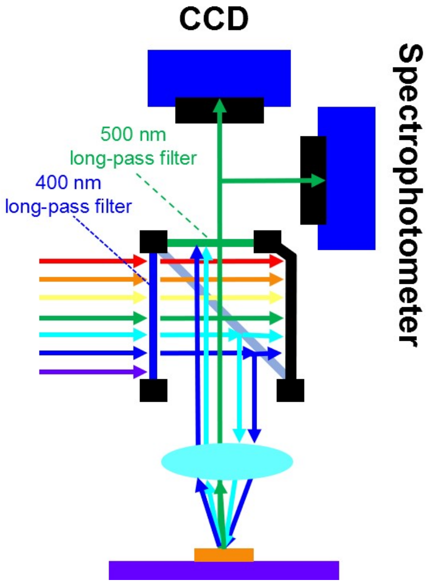

Figure 2.2. Schematic diagram of the cube for capturing the PL image of $CsPbBr_3$. Blue light is filtered out from the Xenon light source to excite the sample, emission after 500 nm is allowed to penetrate the cube and can arrive the CCD and spectrophotometer so that the spectrum could be taken at the same time.

All PL and lasing were performed with a confocal μ-PL system (WITec, alpha-300) (**Figure 2.3**). A mode-locked Ti: Sapphire laser (Tsunami) at 800 nm (pulse width 80 fs, repetition frequency 80 MHz) was amplified by a regenerative amplifier (Spitfire Ace 100, 1KHz) and then introduced into an optical parameter amplifier (OPA, TOPAS Prime). The output laser from OPA could be continuously tuned from 300 to 2,600 nm while used for lasing measurements. The laser at 470 nm (pulse width 80 fs, repetition frequency 1 kHz) was used to pump the $CsPbBr_3$ microplates. The pumping source was focused obliquely on the $CsPbBr_3$ microplate by a lens. The PL and lasing signals were collected by a 20× objective lens and captured by CCD through a high-resolution spectrometer (1,800 g/mm grating).

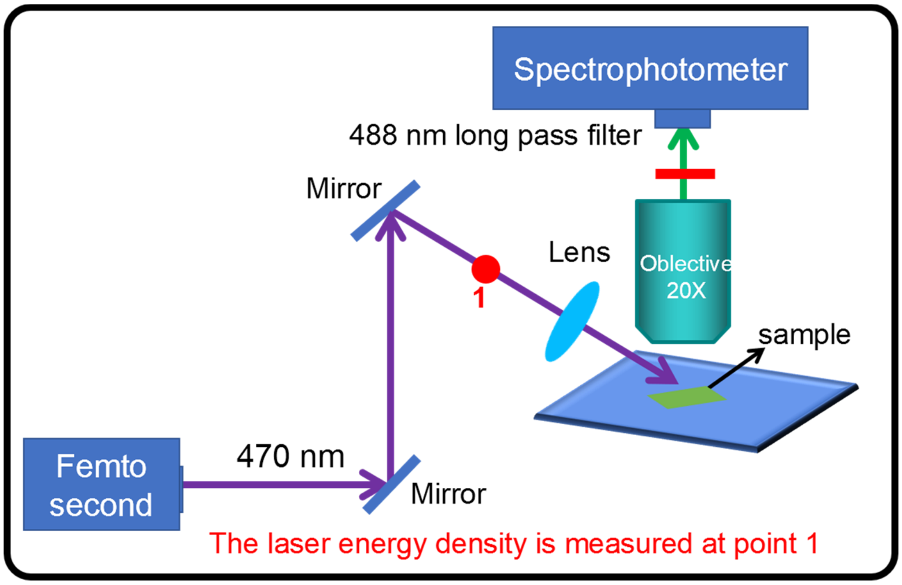

Figure 2.3. Schematic diagram of the femto-second laser system for measuring the laser and PL. The femtosecond laser pulse is used as the pump source and reflected to the microscope. The laser beam is focused on the microplate with a 20× objective lens. The laser signal is also collected with the objective lens and captured by the spectrophotometer.

Device fabrication. The fabrication of sandwiched graphene/$CsPbBr_3$/graphene were fabricated with the following procedures: (1) Bottom graphene was exfoliated with Scotch tape and transferred to the Si/SiO_2 substrate; (2) $CsPbBr_3$ microplates were deposited on the as-prepared substrate with $CsPbBr_3$ partially overlapping with bottom graphene; (3) Top graphene was exfoliated and transferred to the sacrifice substrate and was cover by PMMA layer; (4) PMMA layer with graphene embedded in it was picked up and dropped on the $CsPbBr_3$, with the embedded graphene overlapping with $CsPbBr_3$ to ensure electrical contact; (5) Electrode patterns were define with electron beam lithography (EBL) to fabricated the extended electrodes on graphene to realize electrical measurements; (6) Ti/Au double-metal layer was deposited with electron beam evaporation (EBE) for the extended electrodes, followed by standard lift-off procedure in Chloroform.

Electrical measurements. Electrical measurements were carried out in a commercial probe station (Lakeshore, TTP4) equipped with a semiconductor laser at 473 nm. The power density of the illumination was determined with a power meter (Newport Optical Power Meter 1916-R with a measurement head 818-SL). The electrical measurements were conducted with a precision source/measure unit (Agilent, B2902A).

2.3. Results and discussion

Figure 2.4(a)-(c) show the optical microscope images of the resulting $CsPbCl_3$, $CsPbBr_3$, and $CsPbI_3$ crystals grown on SiO_2/Si (300 nm SiO_2 on Si) wafers. In general, the resulting crystals primarily exhibit a square microplate morphology. Some incomplete microplates can also be observed in all samples. All $CsPbX_3$ microplates exhibit a golden color accompanied with some dark crystals under illumination of a halogen light. Since all $CsPbX_3$ with different anion compositions show the same color, we can rule out the possibility that the color is induced by absorption and emission. The golden color is derived from the back reflection of the illumination light, which occurs on the smooth, mirror-like top surface of the microplates that is perpendicular to the illumination light beam. The incomplete microplates with smooth facets facing directions other than the objective lens reflected away the illumination light, thus resulting in dark crystals.

The lateral illumination of the crystals makes the dark crystals shining, which further supports the existence of a mirror-reflection by the smooth microplate surface and indicates high quality mirror-like facets that are important for laser cavity operations. The thickness of the resulting microplates with different anion compositions was determined using AFM. For $CsPbCl_3$ and $CsPbBr_3$, all the microplates that appeared golden under optical microscope showed a thickness of about 1.5 μm for the entire microplate (insets in **Figure 2.4(a), (b)**). In contrast, golden $CsPbI_3$ microplates showed a typical thickness of about 1.0 μm (inset in **Figure 2.4(c)**), smaller than that of the other two halide-based perovskites. The $CsPbX_3$ square microplates generally exhibited a smooth surface with sharp rectangular corners, and were free of apparent grain boundaries, as shown in the corresponding SEM images (**Figure 2.4(d)-(f)**), suggesting well-faceted single crystals. The edge length of typical $CsPbBr_3$ and $CsPbCl_3$ microplates was between 25 and 30 μm, and that of $CsPbI_3$ microplates fell in the range of 10-15 μm. SEM studies further revealed the morphology of incomplete microplates or polygons (**Figure 2.5**). In general, all such incomplete microplates showed at least one corner with largely right angles, confirming that they are indeed part of an incomplete square microplate structure.

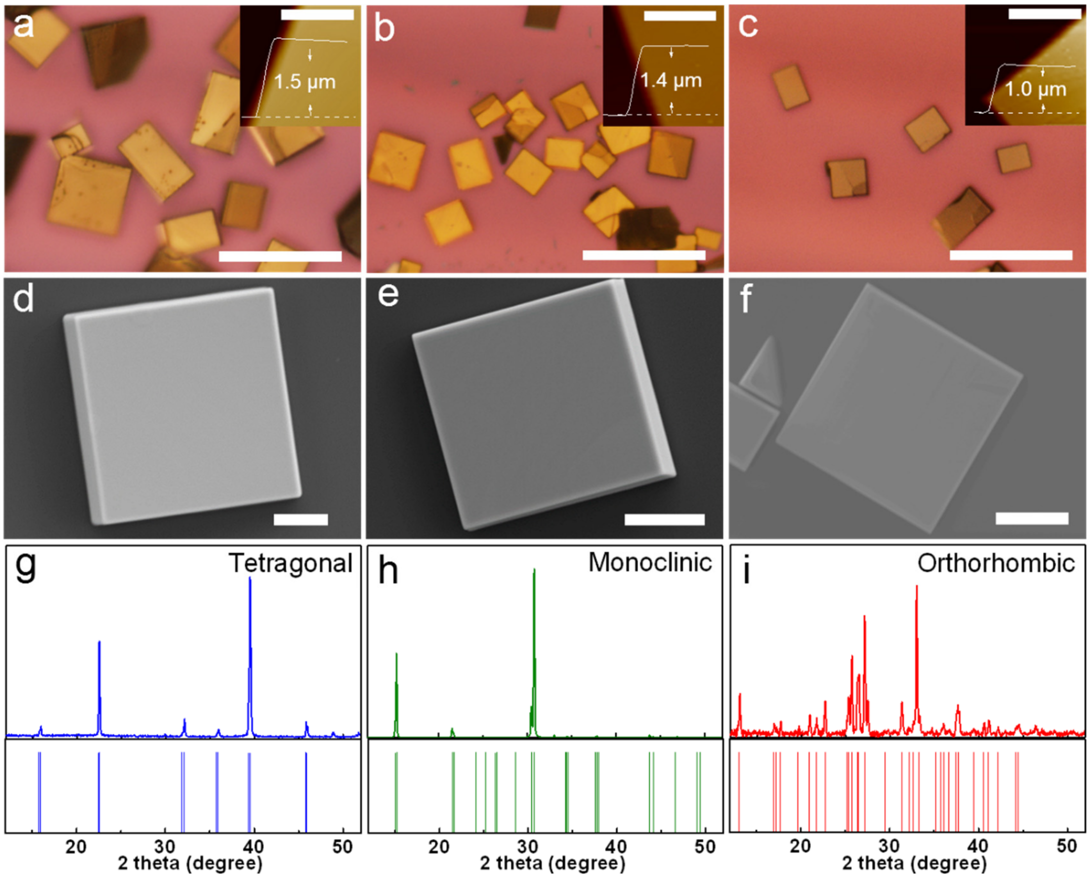

Figure 2.4. Morphology and structural characterization of all-inorganic perovskite microplates. Photographs of (a) $CsPbCl_3$, (b) $CsPbBr_3$, and (c) $CsPbI_3$ microplates with the inset AFM images and curves showing their thicknesses; scale bars in all photographs are 50 µm, while in AFM images are 6 µm. SEM images of (d) $CsPbCl_3$, (e) $CsPbBr_3$, and (f) $CsPbI_3$ showing high smooth surfaces without apparent grain boundaries. Scale bars in SEM images are 5 µm. The XRD patterns of the as-grown microplates are indexed to (g) tetragonal $CsPbCl_3$, (h) monoclinic $CsPbBr_3$, and (i) orthorhombic $CsPbI_3$, respectively.

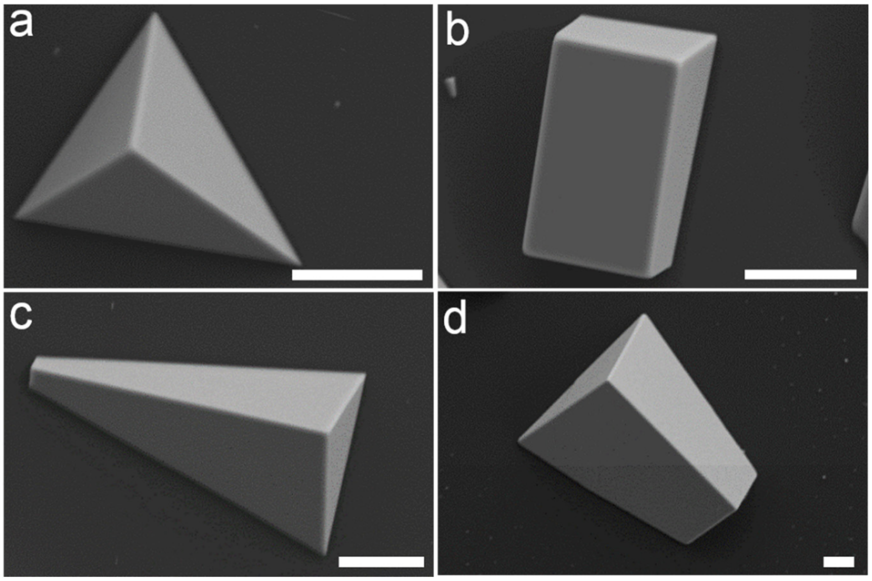

Figure 2.5. SEM images of incomplete microplates or polygons of (a-c) $CsPbBr_3$ and (d) $CsPbCl_3$, Scale bars are 5 μm.

The $CsPbX_3$ crystals typically exhibited complex phase transitions, similar to their hybrid counterparts. In general, $CsPbCl_3$, $CsPbBr_3$, and $CsPbI_3$ all adopted a cubic perovskite phase at elevated temperatures. The pale yellow $CsPbCl_3$ crystals underwent cubic to tetragonal, tetragonal to orthorhombic, and orthorhombic to monoclinic phase transitions at 47, 42, and 37 ° C, respectively, without any color change[38, 39]. $CsPbBr_3$ undergoes a cubic to tetragonal phase transition at 130 ° C and a tetragonal to orthorhombic phase transition at 88 ° C, and retains an orange color with reducing temperature[39, 40]. For $CsPbI_3$, the cubic to orthorhombic phase transition, which is the so-called black to yellow phase transition[41], occurs at a temperature as high as 328° C. Therefore, at room temperature, $CsPbI_3$ usually adopts an orthorhombic yellow phase. The change of crystal structure is relatively small in such phase transitions. The phase transition can be particularly complicated for the vapor phase grown $CsPbX_3$ microplates, since they were grown at a temperature higher than the highest phase transition temperatures, which should result in cubic phase in the as-grown crystals. Although the high temperature phases are thermodynamically metastable at room temperature and can transit to the low temperature phase, they may still be retained if the cooling rate is too fast due to slow phase transition kinetics. Powder PXRD was used to determine the crystal structures of the resulting crystals on the substrate (**Figure 2.4(g)-(i)**). The PXRD patterns of $CsPbCl_3$ crystals can be indexed to the tetragonal phase. The $CsPbBr_3$ crystals can be indexed to the monoclinic phase. The observed monoclinic $CsPbBr_3$ ($a = b = 0.583$ nm, $c = 0.589$ nm, $\alpha = \beta = 90°$, $\gamma = 89.65°$) is very close to the cubic $CsPbBr_3$ ($a = b = c = 0.561$ nm, $\alpha = \beta = \gamma = 90°$), and has not been previously reported at room temperature. The PXRD pattern of $CsPbI_3$ can be indexed to the orthorhombic phase (**Figure 2.4(i)**), which should be PL-inactive[28, 41]. Nonetheless, we observed strong PL from this material, although the exact origin is yet to be fully understood.

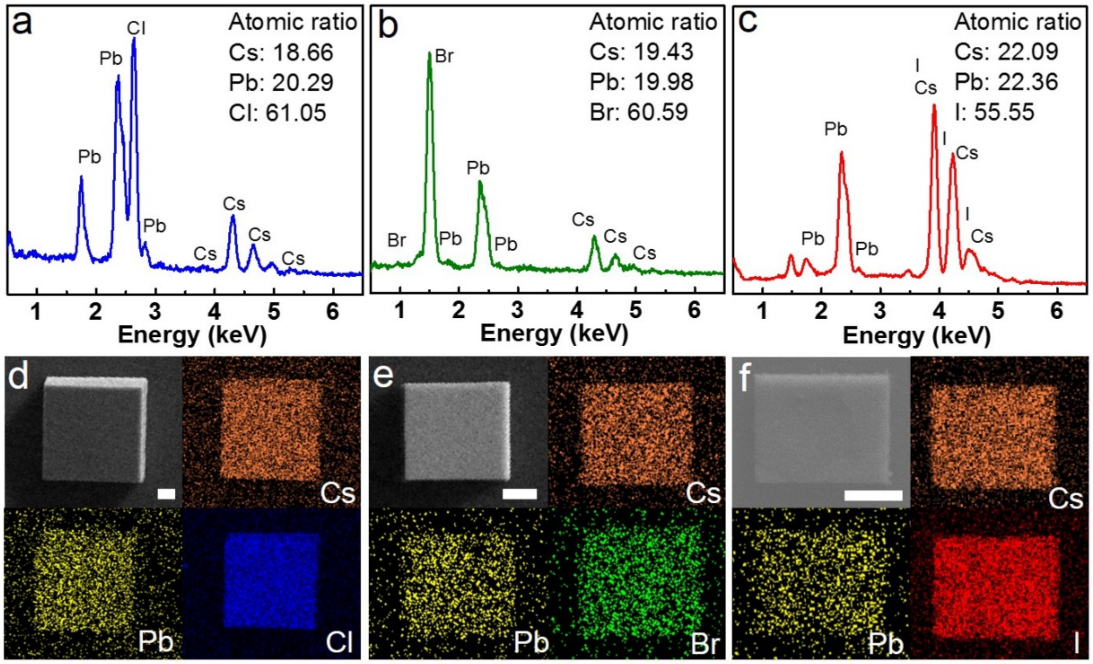

Figure 2.6. Composition analysis of inorganic perovskite microplates. EDS spectra showing the atomic ratios of Cs, Pb, and X (X = Cl, Br, I), and EDS mapping showing the elements distribution; orange for Cs, yellow for Pb, blue, green, and red for Cl, Br, and I respectively. (a) $CsPbCl_3$ microplate with an atomic ratio (%) of Cs:Pb:Cl of 18.66:20.29:61.05; (b) $CsPbBr_3$ microplate with an atomic ratio (%) of Cs:Pb:Br of 19.43:19.98:60.59; (c) $CsPbI_3$ microplate with an atomic ratio (%) of Cs:Pb:I of 20.09:22.36:55.55. All elements were highly uniformly distributed throughout the entire microplates. Scale bars are 5 μm.

The elemental composition of individual $CsPbX_3$ microplates was further analyzed using EDAX. The signals of Cs, Pb, and the corresponding halogens were clearly identified from the EDS spectra. The integration of the elemental characteristic peaks gave quantified atomic ratios (%) of Cs:Pb:Cl, Cs:Pb:Br, and Cs:Pb:I corresponding to 22.09:22.36:55.55, 18.66:20.29:61.05, and 19.43:19.98:60.59 for $CsPbCl_3$, $CsPbBr_3$, and $CsPbI_3$, respectively (**Figure 2.6(a)-(c)**), all of which are consistent with the expected stoichiometric ratio of $CsPbX_3$. Furthermore, the EDAX mapping of individual microplate crystals showed that all the elements are homogeneously distributed throughout the entire microplates (**Figure 2.6(d)-(f)**).

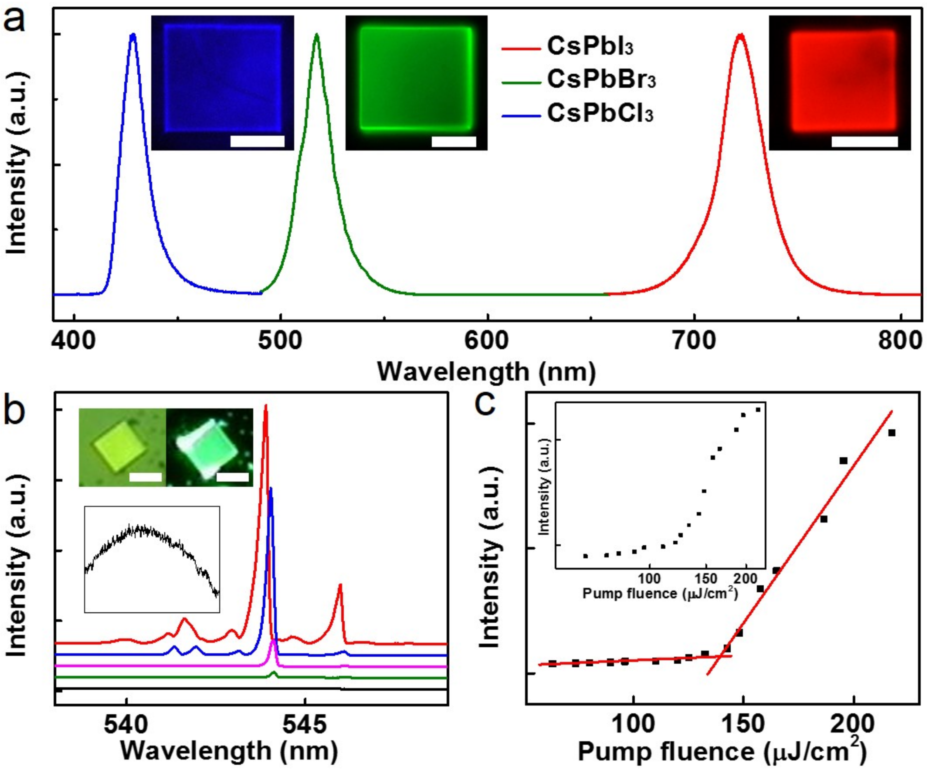

Figure 2.7. Optical properties of inorganic perovskite microplates. (a) PL spectra together with the corresponding inset fluorescence images, scale bars are 10 μm. Highly uniform blue, green, and red emissions are clearly seen for $CsPbCl_3$, $CsPbBr_3$, and $CsPbI_3$ microplates with a peak wavelength at 425, 530, and 705 nm, respectively. The FWHMs for chloride, bromide, and iodide are 14, 17, and 23 nm, respectively. (b) Emission spectra of a $CsPbBr_3$ microplate at five different optical pump fluencies, black for 80 μJ/cm², green for 125 μJ/cm², rose for 142.5 μJ/cm², navy for 165 μJ/cm², and red for 212 μJ/cm². The top inset shows the optical and PL image of the microplate (scale bar is 20 μm), while the lower inset shows a zoom-in spectrum of the spontaneous emission at a pump power of 80 μJ/cm². (c) Nonlinear response of the laser output power with increasing

pump fluence, showing a threshold region of 142 μJ/cm^2 as a "kink" between the two linear regions of the spontaneous and lasing emissions. The inset shows a typical "S" curve of the log–log plot of the input-output curve.

Next, we investigated the optical properties of the resulting microplates using PL spectroscopy. Under a broad field UV excitation, the $CsPbCl_3$, $CsPbBr_3$, and $CsPbI_3$ microplates clearly showed uniform blue, green, and red emissions inside the microplates (**Figure 2.7(a)**, insets), suggesting highly uniform optical properties throughout the entire microplate. Additionally, the edges of the microplates generally showed considerably brighter emission, suggesting the existence of a wave-guiding effect in square microplates. These studies further demonstrate the formation of high-quality crystals with few defects and trap states that are detrimental to radiative recombination of photon-generated electron-hole pairs. The PL spectra showed single intense emission peaks at 425, 530, and 705 nm for $CsPbCl_3$, $CsPbBr_3$, and $CsPbI_3$ microplates (**Figure 2.7(a)**), corresponding to the expected band edge transition at 2.91, 2.33, and 1.75 eV, respectively. The full width at half maximum (FWHM) for $CsPbCl_3$, $CsPbBr_3$, and $CsPbI_3$ microplates were as small as 14, 17, and 23 nm, respectively, implying high optical quality of crystals. Owing to the smooth mirror-like surface in the square plate morphology, the microplates can function as an effective optical cavity with whispering gallery modes to support lasing emission, when the gain medium, e.g., the perovskite microplate itself, is pumped with sufficient power. To further probe the optical properties and cavity performance of the resulting perovskite microplates, we used a $CsPbBr_3$ microplate as an example to conduct lasing characterization under the excitation of a Ti: Sapphire laser (470 nm) (**Figure 2.7(b)**). A single broad emission peak was observed at about 540 nm, when the pump fluence was less than 125 μJ/cm^2 (**Figure 2.7(b)**, inset). Significantly, once the pump fluence was increased to about 125 μJ/cm^2, narrow oscillation peaks were clearly observed around $\lambda = 545$ nm, which represent the optical modes selectively amplified by the optical feedback in the microplate cavity. Upon further increasing the pump fluence to 142.5 μJ/cm^2, the oscillation peak intensity sharply increased together with the further narrowing of the peak width, demonstrating the onset of the lasing action (**Figure 2.7(b)**). As the pump fluence reached 165 μJ/cm^2, the FWHM of the dominant emission peak was as small as $\delta\lambda = 0.19$ nm, comparable to previous reports on semiconductor micro-cavities[42], while the volume of our microplate is much larger than the microplate in the literature (about an order lager), which means the photon-generated carrier density in our microplate is much lower if both microplates are at the same pump energy density. The quality factor was calculated to be 2,863, implying high optical quality. The peak emission intensity versus pump fluence showed a "kink" between the two linear regions that corresponds to spontaneous and lasing emissions, respectively (**Figure 2.7(c)**). The turning between the two linear regimes indicates a lasing threshold of 142.5 μJ/cm^2. The exponential plot of the emission intensity vs. pumping power showed a typical "S" shape (**Figure 2.7(c), inset**) depicting the transition from the spontaneous emission dominating the region at low pump fluence to the stimulated emission dominating the region at high pump fluence. Overall, these studies demonstrate the excellent optical properties of the obtained perovskite microplates.

Owing to the relatively mild growth conditions at 400 °C (the temperature of the substrates when depositing), the growth of inorganic perovskite microplates can be readily expanded beyond SiO_2/Si substrates. For example, $CsPbBr_3$ microplates were successfully grown on diverse materials including reduced graphene oxide, graphene, and MoS_2 (**Figure 2.8(a)-(c)**), as well as muscovite mica, GaN, and glass (**Figure 2.9**).

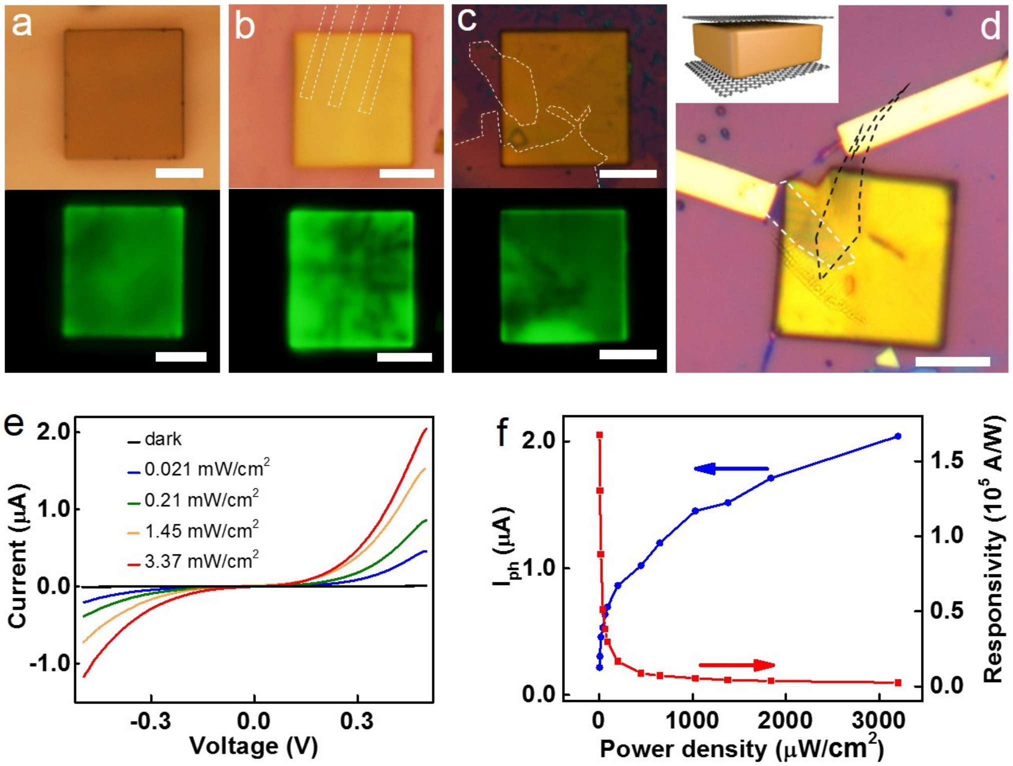

Figure 2.8. Growth of inorganic-perovskite-microplate/2D-material heterostructures as devices. $CsPbBr_3$ grown on (a) reduced graphene oxide, (b) patterned CVD grown graphene (labeled with the white dash line), and (c) CVD grown MoS_2 (labeled with the white dash line), and the corresponding PL images. Scale bars are 25 μm. (d) Optical microscope image of a vertical device constituted of a graphene/$CsPbBr_3$/graphene vertical heterostructure. The top and bottom graphene layers are labeled with white and black dashed lines, respectively. The scale bar is 10 μm. The inset shows a schematic illustration of the vertical device. (e) Photocurrent versus bias in the dark and under different illumination light power densities. (f) Power density dependence of the photocurrent and responsivity under the applied bias of 0.5 V.

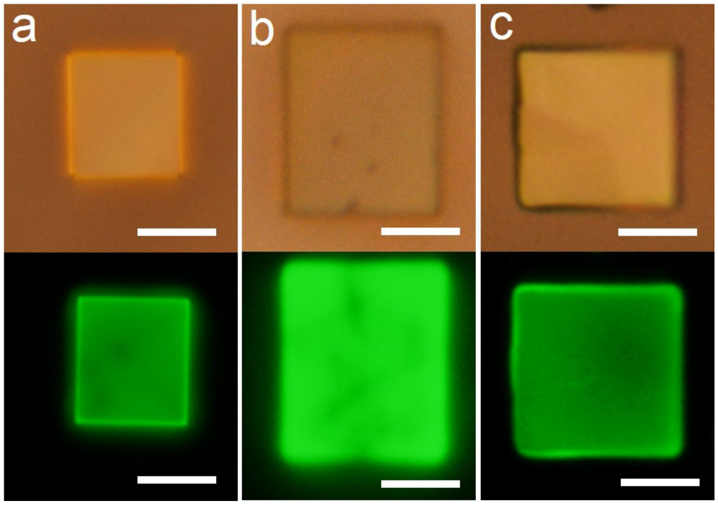

Figure 2.9. $CsPbBr_3$ microplates grown on (a) muscovite mica, (b) GaN and (c) glass with the corresponding PL images, scale bars are 10 μm.

With respect to the growth of perovskite/2D material heterostructures, the respective 2D materials (e.g., reduced graphene oxide, graphene, MoS_2, GaN, etc.) were first deposited on the SiO_2/Si substrates using either a solution deposition or a chemical vapor deposition approach[43-45], and then used as substrates for the direct growth of the perovskite microplates on top. The PL images of the resulting heterostructures showed a strong PL emission with some darker regions corresponding to the heterostructure areas (**Figure 2.8(b), (c)**), which can be attributed to the partial quenching of the perovskite emission by the underlying 2D materials (graphene or MoS_2). The ability to directly grow perovskite crystals on such diverse electronic and optoelectronic materials to form heterostructures can readily enable the construction of functional optoelectronic devices from perovskite single crystals. For example, by first growing $CsPbBr_3$ microplates on an exfoliated graphene flake, followed by the dry transfer of a second layer of graphene on top of the $CsPbBr_3$ microplates, we created a graphene/$CsPbBr_3$/graphene sandwiched vertical device (**Figure 2.8(d)**). Such vertically structured sandwiched devices could be explored as interesting photoresponsive devices for photodetection, with a large photoactive area and short charge extraction length in comparison with lateral devices. The electrical measurements of the vertical device showed nearly zero current in the dark and clear photocurrent under light irradiation (**Figure 2.8(e)**). The photocurrent rapidly increased with the light power and the photocurrent to-dark ratio could reach up to three orders of magnitude. It should also be noted that the photocurrent versus bias curves are nonlinear, indicating the presence of a contact barrier. In contrast to $CH_3NH_3PbI_3$ thin film photoconductors where a huge hysteresis always exists, the hysteresis in our $CsPbBr_3$ single crystal microplates is negligible (**Figure 2.10**), which can be attributed to the excellent crystalline quality of the samples, leading to a very low density of defects (vacancies) and considerably suppressed ion migration responsible for the hysteresis.

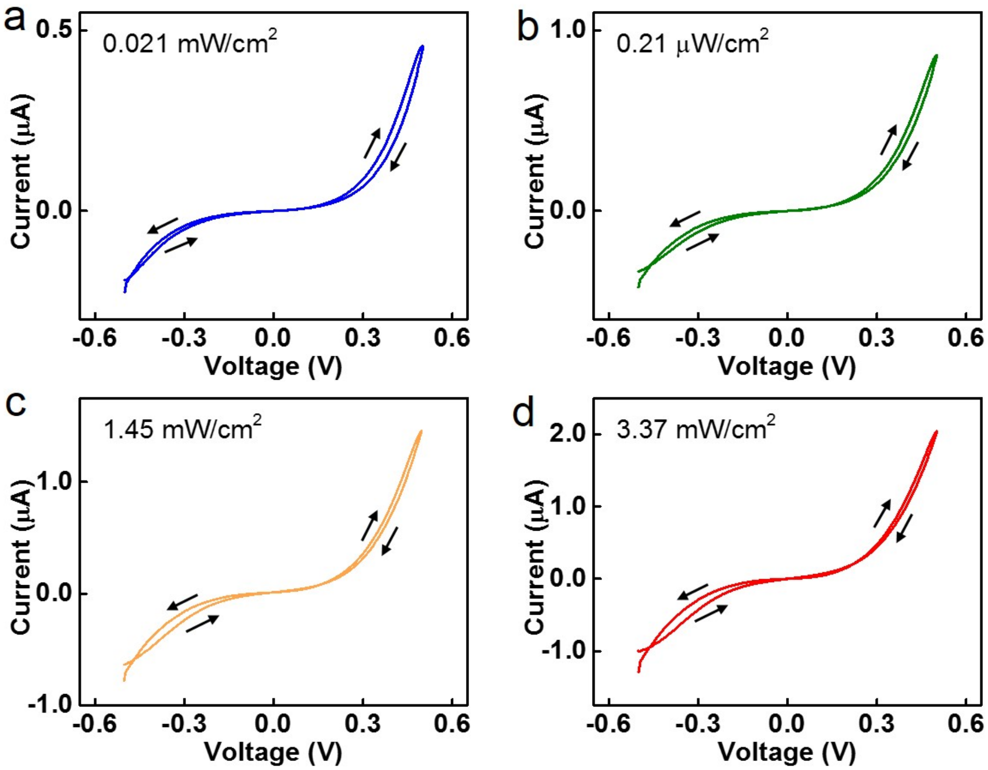

Figure 2.10. Negligible hysteresis in graphene/$CsPbBr_3$/graphene photodetector under illumination of (a) 21.0μW/cm^2, (b) 210.4 μW/cm^2, (c) 1452.1 μW/cm^2 and (d) 3367.2 μW/cm^2.

Compared to the photocurrent, the responsivity, which is defined as the ratio of photocurrent to the light power, takes the light power into consideration and directly represents the sensitivity of a photoconductor. It is evident that the responsivity decreases with the increasing light power density (**Figure 2.8(f)**), which might be due to the increasing carrier-carrier scattering or the reduction of the extraction efficiency arising from the heating effect. The maximum responsivity exceeds 10^5 A/W, which is two orders of magnitude larger than that of hybrid perovskite devices[46] and comparable to that of the CdS nanobelt photoconductor[47, 48]. Compared with the photocurrent in $CsPbBr_3$ nanowire devices, in our device the photocurrent was over three orders of magnitude larger, and the photocurrent density (normalized by the geometric area of the microplate) was about an order of magnitude larger than that of hybrid perovskite thin film photodetectors. This extraordinarily large photocurrent in our device can be ascribed to the short photocarrier extraction length and the excellent crystalline quality due to the high temperature growth and absence of solvent during the synthesis processes. Additionally, the responsivity may be further improved with the optimization of the contact barrier.

2.4. Conclusion

In summary, a single-step vapor phase synthesis has been developed to prepare single-crystalline $CsPbX_3$ microplates. High quality squared microplates with a smooth surface were produced with an edge length on the order of 10 μm and thickness around 1 μm. PL images and spectroscopic studies showed excellent optical properties with uniform and intense blue, green, and red emissions for $CsPbCl_3$, $CsPbBr_3$, and $CsPbI_3$, respectively. Owing to the high optical quality, the squared microplate structure with a smooth surface can function as an excellent optical whispering gallery mode cavity with a quality factor up to 2,863 to support laser emission at room temperature. Lastly, we demonstrated that such microplates can be readily grown on a variety of substrates, including silicon, graphene, and other 2D materials such as MoS_2, readily allowing the construction of heterostructure optoelectronic devices, including a graphene/perovskite/graphene vertical stack photodetector with a high photoresponsivity > 10^5 A/W (corresponding to a gain of 3.9×10^5). The extraordinary optical properties of $CsPbX_3$ microplates, combined with their ability to be grown on diverse materials to form functional heterostructures, could lead to exciting opportunities for broad optoelectronic applications. The vapor phase deposition method could be expanded to the growth of cesium lead halides with different cation or anion compositions and fully tunable optical and electronic properties. Other lead-free all-inorganic perovskites may also be prepared using a single-step vapor phase deposition approach.

2.5. References

1. Kojima, A.; Teshima, K.; Shirai, Y.; Miyasaka, T. *J. Am. Chem. Soc.* **2009,** *131*, 6050-6051.

2. Bai, S.; Wu, Z.; Wu, X.; Jin, Y.; Zhao, N.; Chen, Z.; Mei, Q.; Wang, X.; Ye, Z.; Song, T. *Nano Res.* **2014,** *7*, 1749-1758.

3. Nie, W.; Tsai, H.; Asadpour, R.; Blancon, J.-C.; Neukirch, A. J.; Gupta, G.; Crochet, J. J.; Chhowalla, M.; Tretiak, S.; Alam, M. A. *Science* **2015,** *347*, 522-525.

4. Yan, W.; Li, Y.; Li, Y.; Ye, S.; Liu, Z.; Wang, S.; Bian, Z.; Huang, C. *Nano Res.* **2015,** *8*, 2474-2480.

5. Zhou, H.; Chen, Q.; Li, G.; Luo, S.; Song, T.-b.; Duan, H.-S.; Hong, Z.; You, J.; Liu, Y.; Yang, Y. *Science* **2014,** *345*, 542-546.

6. Tan, Z.-K.; Moghaddam, R. S.; Lai, M. L.; Docampo, P.; Higler, R.; Deschler, F.; Price, M.; Sadhanala, A.; Pazos, L. M.; Credgington, D. *Nat. Nanotechnol.* **2014,** *9*, 687.

7. Zhu, H.; Fu, Y.; Meng, F.; Wu, X.; Gong, Z.; Ding, Q.; Gustafsson, M. V.; Trinh, M. T.; Jin, S.; Zhu, X. *Nat. Mater.* **2015,** *14*, 636.

8. Dou, L.; Yang, Y. M.; You, J.; Hong, Z.; Chang, W.-H.; Li, G.; Yang, Y. *Nat. Commun.* **2014,** *5*, 5404.

9. Wei, H.; Fang, Y.; Mulligan, P.; Chuirazzi, W.; Fang, H.-H.; Wang, C.; Ecker, B. R.; Gao, Y.; Loi, M. A.; Cao, L. *Nat. Photonics* **2016,** *10*, 333.

10. Stranks, S. D.; Burlakov, V. M.; Leijtens, T.; Ball, J. M.; Goriely, A.; Snaith, H. J. *Phys. Rev. Appl.* **2014,** *2*, 034007.

11. Xing, G.; Mathews, N.; Sun, S.; Lim, S. S.; Lam, Y. M.; Grätzel, M.; Mhaisalkar, S.; Sum, T. C. *Science* **2013,** *342*, 344-347.

12. Stranks, S. D.; Eperon, G. E.; Grancini, G.; Menelaou, C.; Alcocer, M. J.; Leijtens, T.; Herz, L. M.; Petrozza, A.; Snaith, H. J. *Science* **2013,** *342*, 341-344.

13. Dong, Q.; Fang, Y.; Shao, Y.; Mulligan, P.; Qiu, J.; Cao, L.; Huang, J. *Science* **2015,** *347*, 967-970.

14. Leijtens, T.; Stranks, S. D.; Eperon, G. E.; Lindblad, R.; Johansson, E. M.; McPherson, I. J.; Rensmo, H.; Ball, J. M.; Lee, M. M.; Snaith, H. J. *ACS Nano* **2014,** *8*, 7147-7155.

15. Shi, D.; Adinolfi, V.; Comin, R.; Yuan, M.; Alarousu, E.; Buin, A.; Chen, Y.; Hoogland, S.; Rothenberger, A.; Katsiev, K. *Science* **2015,** *347*, 519-522.

16. Yang, J.; Siempelkamp, B. D.; Liu, D.; Kelly, T. L. *ACS Nano* **2015,** *9*, 1955-1963.

17. Deretzis, I.; Alberti, A.; Pellegrino, G.; Smecca, E.; Giannazzo, F.; Sakai, N.; Miyasaka, T.; La Magna, A. *Appl. Phys. Lett.* **2015,** *106*, 131904.

18. Merdasa, A.; Bag, M.; Tian, Y.; Källman, E.; Dobrovolsky, A.; Scheblykin, I. G. *J. Phys. Chem. C* **2016,** *120*, 10711-10719.

19. Nikl, M.; Nitsch, K.; Chval, J.; Somma, F.; Phani, A.; Santucci, S.; Giampaolo, C.; Fabeni, P.; Pazzi, G.; Feng, X. *J. Phys. Condens. Matter* **2000,** *12*, 1939.

20. Somma, F.; Nikl, M.; Nitsch, K.; Giampaolo, C.; Phani, A.; Santucci, S. *Superficies y vacío* **1999**, 62-64.

21. Eperon, G. E.; Paterno, G. M.; Sutton, R. J.; Zampetti, A.; Haghighirad, A. A.; Cacialli, F.; Snaith, H. J. *J. Mater. Chem. A* **2015,** *3*, 19688-19695.

22. Feng, J.; Yan, X.; Zhang, Y.; Wang, X.; Wu, Y.; Su, B.; Fu, H.; Jiang, L. *Adv. Mater.* **2016,** *28*, 3732-3741.

23. Li, D.; Wang, G.; Cheng, H.-C.; Chen, C.-Y.; Wu, H.; Liu, Y.; Huang, Y.; Duan, X. *Nat. Commun.* **2016,** *7*, 11330.

24. Li, D.; Wu, H.; Cheng, H.-C.; Wang, G.; Huang, Y.; Duan, X. *ACS Nano* **2016,** *10*, 6933-6941.

25. Wang, G.; Li, D.; Cheng, H.-C.; Li, Y.; Chen, C.-Y.; Yin, A.; Zhao, Z.; Lin, Z.; Wu, H.; He, Q. *Sci. Adv.* **2015,** *1*, e1500613.

26. Akkerman, Q. A.; D'Innocenzo, V.; Accornero, S.; Scarpellini, A.; Petrozza, A.; Prato, M.; Manna, L. *J. Am. Chem. Soc.* **2015,** *137*, 10276-10281.

27. Nedelcu, G.; Protesescu, L.; Yakunin, S.; Bodnarchuk, M. I.; Grotevent, M. J.; Kovalenko, M. V. *Nano Lett.* **2015,** *15*, 5635-5640.

28. Protesescu, L.; Yakunin, S.; Bodnarchuk, M. I.; Krieg, F.; Caputo, R.; Hendon, C. H.; Yang, R. X.; Walsh, A.; Kovalenko, M. V. *Nano Lett.* **2015,** *15*, 3692-3696.

29. Zhang, D.; Eaton, S. W.; Yu, Y.; Dou, L.; Yang, P. *J. Am. Chem. Soc.* **2015,** *137*, 9230-9233.

30. Zhang, D.; Yang, Y.; Bekenstein, Y.; Yu, Y.; Gibson, N. A.; Wong, A. B.; Eaton, S. W.; Kornienko, N.; Kong, Q.; Lai, M. *J. Am. Chem. Soc.* **2016,** *138*, 7236-7239.

31. Akkerman, Q. A.; Motti, S. G.; Srimath Kandada, A. R.; Mosconi, E.; D'Innocenzo, V.; Bertoni, G.; Marras, S.; Kamino, B. A.; Miranda, L.; De Angelis, F. *J. Am. Chem. Soc.* **2016,** *138*, 1010-1016.

32. Bekenstein, Y.; Koscher, B. A.; Eaton, S. W.; Yang, P.; Alivisatos, A. P. *J. Am. Chem. Soc.* **2015,** *137*, 16008-16011.

33. Shamsi, J.; Dang, Z.; Bianchini, P.; Canale, C.; Di Stasio, F.; Brescia, R.; Prato, M.; Manna, L. *J. Am. Chem. Soc.* **2016,** *138*, 7240-7243.

34. Eaton, S. W.; Lai, M.; Gibson, N. A.; Wong, A. B.; Dou, L.; Ma, J.; Wang, L.-W.; Leone, S. R.; Yang, P. *Proc. Natl. Acad. Sci. U.S.A.* **2016,** *113*, 1993-1998.

35. Fu, Y.; Zhu, H.; Stoumpos, C. C.; Ding, Q.; Wang, J.; Kanatzidis, M. G.; Zhu, X.; Jin, S. *ACS Nano* **2016,** *10*, 7963-7972.

36. Xing, J.; Liu, X. F.; Zhang, Q.; Ha, S. T.; Yuan, Y. W.; Shen, C.; Sum, T. C.; Xiong, Q. *Nano Lett.* **2015,** *15*, 4571-4577.

37. Zhang, Q.; Su, R.; Liu, X.; Xing, J.; Sum, T. C.; Xiong, Q. *Adv. Funct. Mater.* **2016,** *26*, 6238-6245.

38. Fujii, Y.; Hoshino, S.; Yamada, Y.; Shirane, G. *Phys. Rev. B* **1974,** *9*, 4549.

39. MØLLER, C. K. *Nature* **1958,** *182*, 1436.

40. Sakata, M.; Nishiwaki, T.; Harada, J. *J. Phys. Soc. Jpn.* **1979,** *47*, 232-233.

41. Trots, D.; Myagkota, S. *J. Phys. Chem. Solids* **2008,** *69*, 2520-2526.

42. Agarwal, R.; Barrelet, C. J.; Lieber, C. M. *Nano Lett.* **2005,** *5*, 917-920.

43. Duan, X.; Wang, C.; Shaw, J. C.; Cheng, R.; Chen, Y.; Li, H.; Wu, X.; Tang, Y.; Zhang, Q.; Pan, A. *Nat. Nanotechnol.* **2014,** *9*, 1024.

44. Shaw, J. C.; Zhou, H.; Chen, Y.; Weiss, N. O.; Liu, Y.; Huang, Y.; Duan, X. *Nano Res.* **2014,** *7*, 511-517.

45. Zhou, H.; Wang, C.; Shaw, J. C.; Cheng, R.; Chen, Y.; Huang, X.; Liu, Y.; Weiss, N. O.; Lin, Z.; Huang, Y. *Nano Lett.* **2014,** *15*, 709-713.

46. Cheng, H.-C.; Wang, G.; Li, D.; He, Q.; Yin, A.; Liu, Y.; Wu, H.; Ding, M.; Huang, Y.; Duan, X. *Nano Lett.* **2015,** *16*, 367-373.

47. Li, L.; Wu, P.; Fang, X.; Zhai, T.; Dai, L.; Liao, M.; Koide, Y.; Wang, H.; Bando, Y.; Golberg, D. *Adv. Mater.* **2010,** *22*, 3161-3165.

48. Li, D.; Zhang, J.; Zhang, Q.; Xiong, Q. *Nano Lett.* **2012,** *12*, 2993-2999.

Chapter 3. Large-area monocrystalline all-inorganic halide perovskite thin films and heterojunctions

3.1. Introduction

Methylammonium lead tri-iodide hybrid perovskite has attracted intensive research interests due to its extraordinary performances in the photovoltaic field[1-11], with a certified power conversion efficiency rapidly soaring up to 22.1% in just a few years[12]. Despite this extraordinary progress, the hybrid perovskite-based devices[13-16] are currently plagued by their poor environment stability. Recent studies have shown that the replacement of organic cations with inorganic cations to produce all-inorganic perovskite[17, 18], such as $CsPbX_3$ (X = Cl, Br, I), could lead to considerably improved stability. Although significant efforts have been devoted to synthesizing micro-crystal domains[19, 20] and various nanostructures[21-28], it remains a substantial challenge to produce high-quality monocrystalline thin films, which is essential for exploring these new materials for diverse optoelectronic applications. Here we report the first growth of large-area monocrystalline all-inorganic perovskite thin film for functional electronics and optoelectronics. We show highly aligned micro-crystal domains can be readily grown on muscovite mica substrate using a vapor phase deposition process, which can further grow and eventually merge into a large-area monocrystalline $CsPbBr_3$ thin film with an excellent optical quality. The $CsPbBr_3$ square microplates can be readily grown on the (001) surface of muscovite mica with an epitaxial relations of $CsPbBr_3$ [100]//mica [100] and $CsPbBr_3$ [010]//mica[010], which eventually merge together to form a continuous monocrystalline thin film with increasing growth time. Cs^+ occupies the K^+ vacancies from the peeled mica, providing the original nucleation sites of $CsPbBr_3$. Using the lithography approach (though some acceptable damages were introduced), functional electronic devices (transistors) and optoelectronic devices can be readily fabrication with respectable carrier mobility, photocurrent gain and response speed, making it a potential platform for the massive integration of functional electronic and optoelectronic devices. Photoresponse studies show rapid photoresponse with a photocurrent gain about 29 and response time smaller than 20 ms. The transistor measurement shows a strong gate modulation with an on/off ratio of 11 and carrier mobility of about 0.26 cm^2/Vs. We further demonstrate that an electron beam lithography patterning approach can be used to enable selective anion-exchange to produce lateral heterojunctions with a clear rectification behavior. The capability to grow $CsPbBr_3$ monocrystalline thin film and to conduct the selective anion-exchange to form well-defined heterostructures creates a robust material platform for both the fundamental investigation of their optoelectronic properties and potential applications in integrated optoelectronic systems.

3.2. Experimental section

Chemicals: CsBr (>99%), $PbBr_2$ (>98%) were all purchased from Sigma-Aldrich. All the chemicals were used as received without further purification, Poly(methyl methacrylate) (PMMA, A8), isopropyl alcohol(IPA, certified ACS), methyl isobutyl ketone (MIBK, ≥99.5%, HPLC).

Preparation of precursor: The precursors, CsBr and $PbBr_2$, were well mixed together with a molar ratio of 1:1. The mixture was brought to 380 ^{o}C and the temperature was maintained for 12 hours to ensure the solid-state reaction of the two precursors was completed to form $CsPbBr_3$ powder. The $CsPbBr_3$ powder was used as the vaporized source for deposition.

Preparation of substrate: Muscovite mica (Grade V1) was purchased from Electron Microscopy Sciences. The muscovite was exfoliated right before the growth to expose the fresh surface with minimum absorbents for the growth.

Deposition of $CsPbBr_3$ film: The growth of $CsPbBr_3$ thin film was conducted in a home-built tube furnace system via a one-step vapor phase deposition process under controlled pressure. $CsPbBr_3$ powder source was placed at the center of the furnace in a 1-inch quartz tube, and the exfoliated muscovite with freshly exposed surface was placed downstream as the growth substrate. The system was pumped down and flushed with argon gas for three times before stabilized at 200 mbar with 100 sccm of argon gas as the carrier gas. The furnace was ramped to 560 °C and kept at this temperature for 60 minutes for the completion of a $CsPbBr_3$ thin film with the thickness of 1 μm (substrate temperature < 560 °C).

Characterization: Characterizations were carried out using Optical microscopy (Olympus BX51), SEM (Zeiss Supra 40 VP, FE-SEM), TEM (Titan S/TEM FEI; acceleration voltage, 300 KV), PXRD (Panalytical X'Pert Pro X-ray Powder Diffractometer, Bruker D1 High Resolution Diffractometer with Graded Mirror and Dual (220) Si Incident Beam Optics, Bruker D1 Parallel Beam Diffractometer with Graded Mirror Incidence Beam Optics), AFM (Bruker Dimension FastScan Scanning Probe Microscope), PL spectroscopy (Horiba, 488 nm laser wavelength).

Preparation of iodide solution. CsI was dissolved in IPA as the anion exchange solution with excess of CsI appeared at the bottom of the container, implying the CsI is saturated in IPA.

Formation selective windows. Certain patterns were designed with AutoCAD software. PMMA was spread on $CsPbBr_3$ thin film by spin coating. The patterns were defined with EBL and developed in IPA: MIBK (3:1) developer.

Device fabrication: Au electrodes were deposited on $CsPbBr_3$ thin film with a shadow mask in electron beam evaporator. PMMA was spread to cover the thin film and Au electrodes, area of interest was patterned with EBL and exposed to conduct anion exchange.

Characterization: The electrical measurements were conducted with a precision source/measure unit (Agilent, B2902A).

3.3. Results and discussion

To monitor the growth process including the intermediate morphologies during different stages of $CsPbBr_3$ thin film growth, we interrupted the growth at 15 min and 30 min after the growth started to record the products. We found the growth started as separated domains with a square or rectangular morphology, as shown under both optical microscope and SEM (**Figure 3.1(a), (d)**).

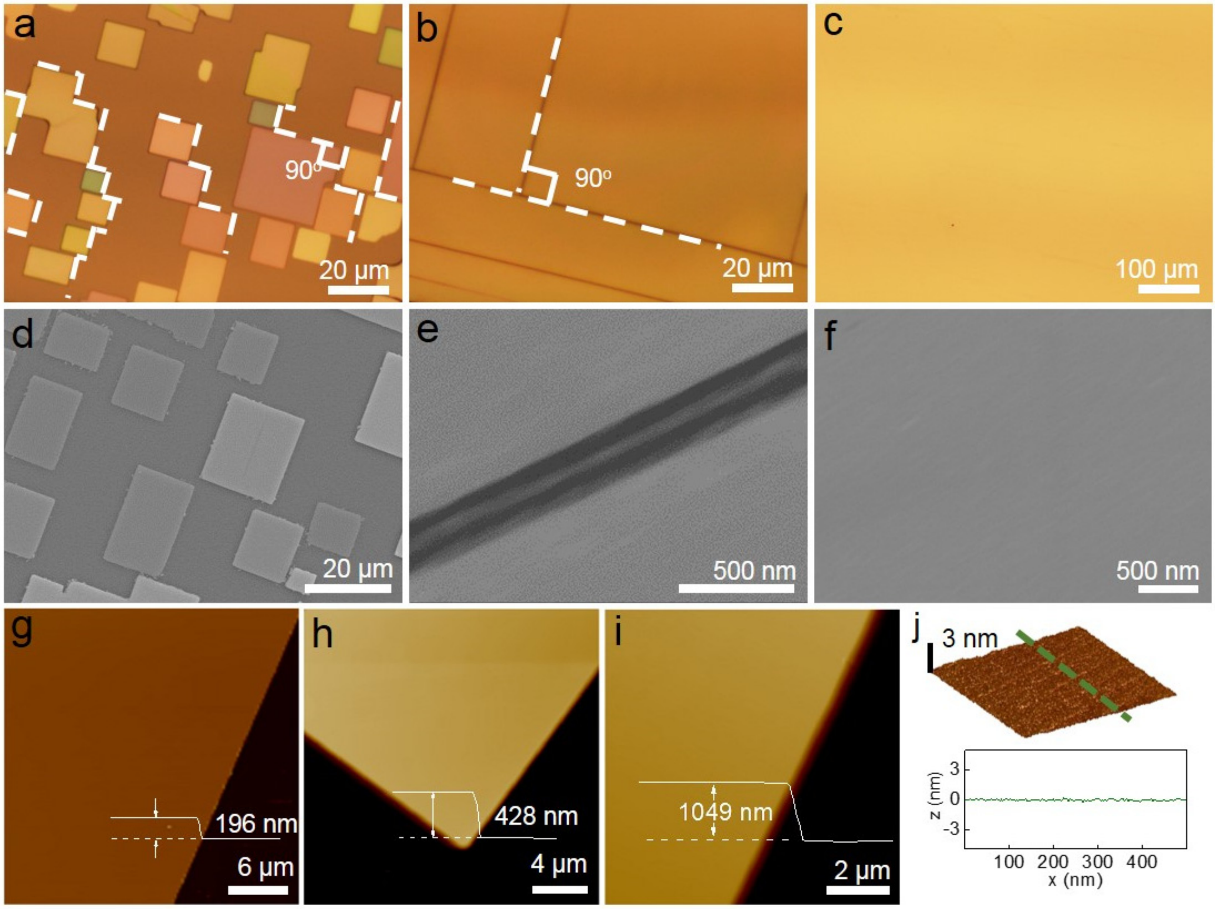

Figure 3.1. Images of the intermediate growth process. (a) Oriented $CsPbBr_3$ microplates grown on muscovite; (b) Incomplete thin film with gutters between neighboring domains; (c) Complete $CsPbBr_3$ thin film; The SEM images of (d) separated $CsPbBr_3$ microplates, (e) incomplete thin film with gutters, and (f) completed thin film. AFM images show the thickness of (g) the isolated domains, (h) incomplete thin film and (i) completed thin film are typically about 196 nm, 428 nm and 1048 nm, respectively; (j) 3D image of the surface topography of the $CsPbBr_3$ thin film (upper)

with the corresponding line profile plot (lower), highlighting an ultra-smooth surface with a small root mean square roughness of 0.19 nm.

Interestingly, all the domains, with size in the range of 10 μm to 30 μm, were well-oriented with each other, as highlighted by perpendicular zigzag guidelines with the exact right angles, suggesting a guided growth with a certain fixed crystallographic orientation towards the underlying muscovite. The isolated domains expand with increasing growth time, gradually growing towards each other with some perpendicular gutters indicating the incomplete mergence (**Figure 3.1 (b), (e)**), and eventually fully merging together to result in a highly continuous thin film without any obvious grain boundaries over large area (**Figure 3.1 (c), (f)**).

The thicknesses of the isolated domains, incomplete thin film and completed thin film are typically about 196 nm, 428 nm and 1048 nm, respectively, as determined with AFM studies (**Figure 3.1(g)-(i)**). High-resolution AFM studies show the surface of the resulting thin film is nearly atomically flat, with root mean square roughness ~ 0.19 nm (**Figure 3.1(j)**). Such ultra-smooth surface is essential for ensuring intimate contact with the laminated electrodes and enabling the formation of high-performance devices to be discussed in next chapter.

XRD studies show that the resulting film can be indexed to cubic phase $CsPbBr_3$ (JCPDS # 00-054-0752) (**Figure 3.2(a)**), with a *d*-spacing of 5.83 Å for (001) plane. The full width at half maximum (FWHM) of the (001) diffraction peak is 0.06°, closely comparable to that of the $CsPbBr_3$ bulk single crystal (0.05°)[29], implying high crystalline quality of the resulting thin film. The diffraction peaks of muscovite, crystalizing into monoclinic phase (JCPDS # 00-002-0056) with (001) plane exposed, are also shown in the same diagram and marked by star. It is important to note that only the {001} family planes of cubic phase $CsPbBr_3$ show up in the XRD pattern, suggesting a highly oriented thin film growth consisting of multiple merged domains with the identical out-of-plane crystal orientation, with the (001) plane of $CsPbBr_3$ in parallel to the (001) plane of muscovite. To further investigate the single crystallinity of the resulting thin film, the rocking curve of the (110) peak was measured by omega scan, showing a FWHM of 0.15° (**Figure 3.2(b)**). The small FWHM is comparable to that of the epitaxial GaN film by MOCVD[30], further confirming the high crystallinity of the as-grown $CsPbBr_3$ thin film. To further determine the in-plane orientation of the film, we also conducted parallel beam reflection diffraction studies. The resulted (110) pole figure of the $CsPbBr_3$ film clearly shows the four poles with a 90° interval, corresponding to the four equivalent {110} planes (**Figure 3.2(c)**). The symmetrical pole figure strongly supports that the resulting thin film is monocrystalline.

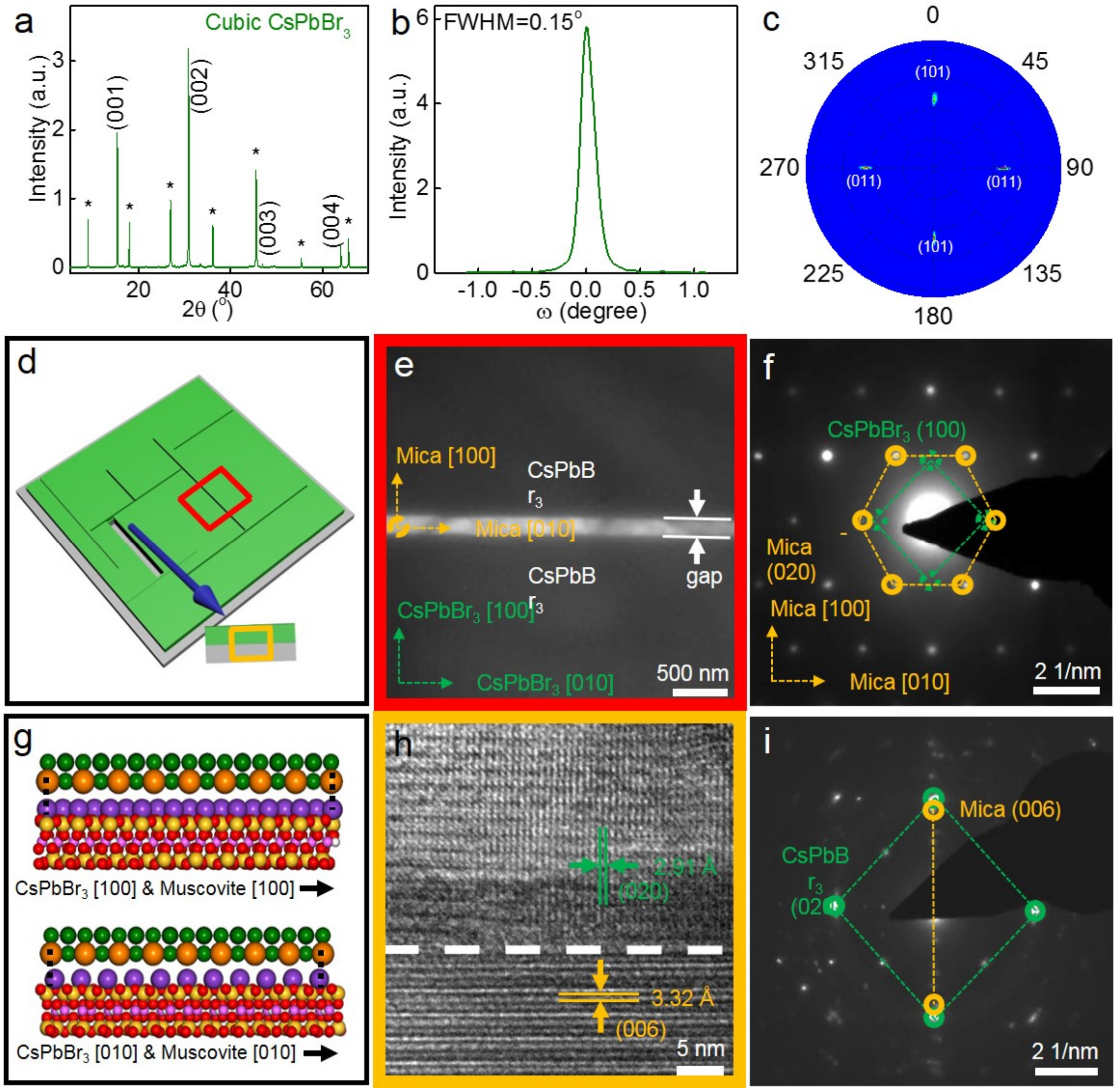

Figure 3.2. Crystal structures characterization of CsPbBr$_3$ on muscovite mica. (a) PXRD patterns of completed CsPbBr$_3$ film on muscovite mica. Peaks from mica substrate were marked by '*'; (b) (110) rocking curve of CsPbBr$_3$ with omega scan, the FWHM was determined to be 0.15°; (c) (110) pole figure of CsPbBr$_3$, 4 poles corresponding to symmetrical planes of {110} family are shown with equal interval; (d) Schematic illustration of the planar view of CsPbBr$_3$/muscovite and CsPbBr$_3$/muscovite slice prepared by focused ion beam cutting, showing the slice was cut in parallel with the flat edge. The red rectangle highlights the area for the planar view (e) and the orange rectangle highlights the area for cross sectional view in (h); (e) TEM image of CsPbBr$_3$ with flat edge on muscovite, the white stripe is the incomplete gutter that allow electron beam transmission, and dark regions corresponds to two unmerged CsPbBr$_3$ domains that block the electron beam; (f) Electron diffraction pattern of muscovite in the gutter with simulated CsPbBr$_3$ diffraction patterns (dashed green circles); (g) Crystal model of CsPbBr$_3$/muscovite interface showing the epitaxial relationship, viewed along [100] and [010] directions, respectively; (h) Cross sectional HRTEM image of the CsPbBr$_3$/muscovite slice of the area highlighted by orange rectangle in (d); (i) Corresponding electron diffraction of CsPbBr$_3$/muscovite slice, showing that [001] of CsPbBr$_3$ is in parallel with [001] of muscovite. Other unidentified diffractions spots are resulted from rapid degradation of the perovskite sample under electron beam irradiation.

To verify the in-plane relative orientation of $CsPbBr_3$ thin film on muscovite, we conducted TEM characterization on the $CsPbBr_3$ thin film peeled off from muscovite. Due to the affinity of $CsPbBr_3$ to muscovite, a thin layer of muscovite was also peeled off together with $CsPbBr_3$. We located a position with incompletely merged rectangular $CsPbBr_3$ domains with bare muscovite in the 'gutter' between them for TEM analysis. The planar view TEM image of the gutter region (highlighted by the red rectangle in **Figure 3.2(d)**) clear show the thin gutter region where the electron beams can readily pass through (with a light contrast in TEM image in **Figure 3.2(e)**), while the two perovskite domains next to the gutter are too thick for electron beam to pass through (with a dark contrast in TEM image in **Figure 3.2(e)**). Selected-area electron diffraction (SAED) pattern of the muscovite in the 'gutter' between two $CsPbBr_3$ domains (**Figure 3.2(f))** with zero rotation from the image (**Figure 3.2(e)**) reveals the crystallographic orientations of muscovite, with the [010] direction of muscovite oriented in parallel to the flat 'banks' of the incomplete $CsPbBr_3$ film. Considering the $CsPbBr_3$ crystalized into cubic phase, and the intercepted 'gutters' in the incomplete film are perpendicular to each other, it's reasonable to assume that the flat edge of $CsPbBr_3$ domain is along the [010] direction of cubic $CsPbBr_3$, which means the [010] direction of $CsPbBr_3$ is in parallel to the [010] direction of muscovite. Based on these analyses, the diffraction patterns of $CsPbBr_3$, same to the simulated patterns (dashed green circles) in **Figure 3.2(f)**, would have appeared if not limited by the large thickness of the sample. Now that $CsPbBr_3$-[010]//muscovite-[010], the $CsPbBr_3$-[100] must be parallel to muscovite-[100] considering the alpha angles of $CsPbBr_3$ and muscovite are both 90º. These analyses suggest an epitaxial growth relationship: $CsPbBr_3$ laterally expands along [100] and [010] directions, which are in parallel to [100] and [010] directions of muscovite, respectively.

A further analysis of the lattice spacing (**Figure 3.2(g)**) suggests that, along $CsPbBr_3$ [100] direction, 8 periodicities of $CsPbBr_3$ (100) matches nearly perfectly with 9 periodicities of muscovite (100) with negligible lattice mismatch of only 0.04%; while along $CsPbBr_3$ [010] direction, 8 periodicities of $CsPbBr_3$ (010) planes match with 5 periodicities of muscovite (010) planes with a lattice mismatch of 3.3%. Although with different lattice symmetries, the lattice matching along these specific directions appears sufficient to guide the epitaxial growth of the $CsPbBr_3$ thin films on muscovite over large-area to produce high quality mono-crystalline thin film.

To further verify that the flat edge of the microplates is along [010] direction of $CsPbBr_3$, we conducted cross sectional TEM and electron diffraction studies on a slice of $CsPbBr_3$/muscovite cut from the $CsPbBr_3$ film on muscovite in parallel with the flat edge of $CsPbBr_3$ (**Figure 3.2(d)**) shows the schematic, highlighted by the orange rectangle). The [010] and [001] directions of $CsPbBr_3$ and the [001] direction of muscovite can be clearly indexed on high-resolution TEM image (**Figure 3.2(h)**) and the SAED pattern (**Figure 3.2(i)**) of the slice, further confirming the flat edge is paralleled to [010] direction of the cubic $CsPbBr_3$ and epitaxial relationship determined above.

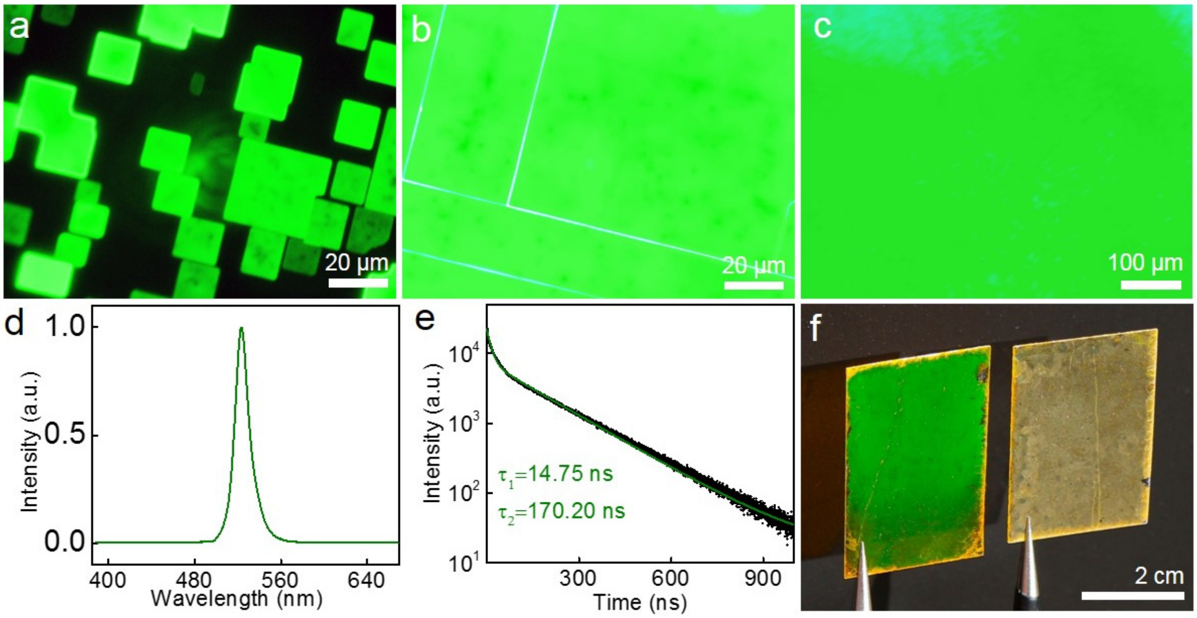

Figure 3.3. Optical characterizations. Photoluminescence image of (a) the separated $CsPbBr_3$ microplates grown on muscovite, (b) uncompleted film with unmerged gutters, and (c) completed thin film. All of these photoluminescence images correspond to the optical microscope images shown in **Figure 3.1(a), (b)** and **(c)**, respectively. (d) Photoluminescence emission spectrum of the $CsPbBr_3$ thin film; (e) Time resolved photoluminescence (TRPL) decay measurement to determine the carrier lifetime; (f) Photograph of the as-grown $CsPbBr_3$ thin film (left) and spin coating thin film (right) under direct sunlight illumination. Some non-uniformity seen in the photograph is attributed to long-range non-evenness of the exfoliated muscovite substrate (with slightly different scattering at different angles) and accidental scratches when handling with tweezers instead of the intrinsic optical quality of the material.

Photoluminescence images and spectroscopy studies show bright green light emission in both the isolated domains and the continuous thin film (**Figure 3.3(a), (b)** and **(c)**) with a single emission peak at about 530 nm (**Figure 3.3(d)**), consistent with the previously reported emission wavelength of $CsPbBr_3$[31]. The gutters in incomplete thin film apparently show stronger emission than the surrounding area. This phenomenon can be attributed to the optical cavity effect of the thin film with the gutters forming the terminal edges of the cavity, which is an indicator of the high crystalline quality and high photoluminescence efficiency of the $CsPbBr_3$ thin film.

To further evaluate the optical quality of the resulting thin film, we have conducted TRPL decay measurements to determine the carrier lifetime under the excitation of a 375 nm laser (working at 0.125 MHz) with a pulse width of 91.5 ps and a photon density of 5.17×10^{14} photons/cm^2. The TRPL shows bi-exponential decay versus time with two time constants of 14.75 ns and 170.20 ns, respectively[23, 32] (**Figure 3.3(e)**). The short decay component can be attributed to the radiative recombination from the surface of the thin films, and the long component is regarded as a result of the bulk recombination from the inner part of the material. Both the surface and the bulk radiative recombination lifetime are considerably longer than those of the spin-coated thin films and compare well with those of the highest quality bulk monocrystals[23, 33-40], suggesting few trap states and high optical quality of the resulting thin film material[33, 39].

The size of the as-grown $CsPbBr_3$ thin film can be readily scaled up to be as large as multi-centimeter scale, which is only limited by the inner diameter of quartz tube of the CVD system. Notably, the photograph of the as-grown film under direct sunlight (2:00 pm in Los Angeles) shows a bright green light emission over the entire substrate (left sample in **Figure 3.3(f)**). In contrast, the spin coated $CsPbBr_3$ thin film on muscovite does not show apparent green emission under the same condition (right sample in **Figure 3.3(f)**). The bright green light emission under natural sunlight illumination without any optical filtration suggests the emission dominates the reflection/absorption/scattering of the white light and gives a direct visual evidence of the high optical quality of the resulting thin film[49,50].

The as-deposited thin film shows extraordinary stability and can be stored in air without apparent quality degrading for at least 3 months, which is verified by unchanged PXRD and PL studies, demonstrating the high moisture stability. The PXRD and PL of film before and after being heated at 220 °C for 30 min in atmosphere don't change apparently, confirming the tolerance to intense heat (**Figure 3.4**), which is in stark contrast to hybrid perovskite.

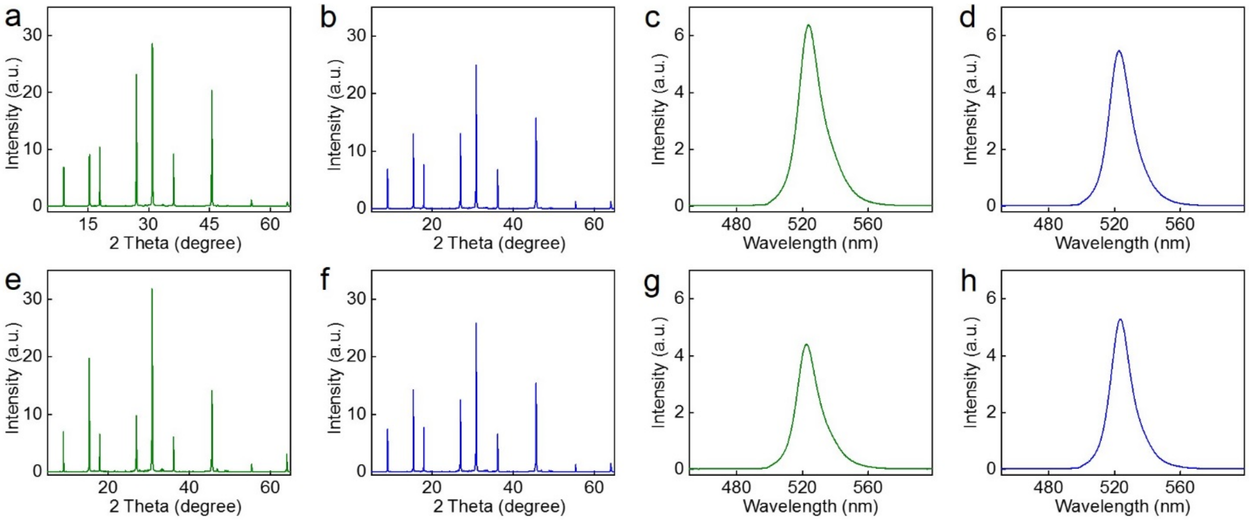

Figure 3.4. Stability test of $CsPbBr_3$ film with XRD and PL. (a) XRD of $CsPbBr_3$ film originally grown for stability test in air; (b) XRD of corresponding film stored in air for 3 months; (c) PL of corresponding $CsPbBr_3$ film originally grown; (d) PL of corresponding film stored in air for 3 months; (e) XRD of $CsPbBr_3$ film originally grown for thermal stability test; (f) XRD of corresponding film heated at 220 °C in air for 0.5 h; (g) PL of corresponding $CsPbBr_3$ film originally grown for thermal stability test; (h) PL of corresponding film heated at 220 °C in air for 0.5 h.

The resulting $CsPbBr_3$ film can be further converted into $CsPbI_3$ with anion-exchange process. The resulting thin film shows prominent red emission at 690 nm (**Figure 3.5**), consistent with expected PL emission from $CsPbI_3$.

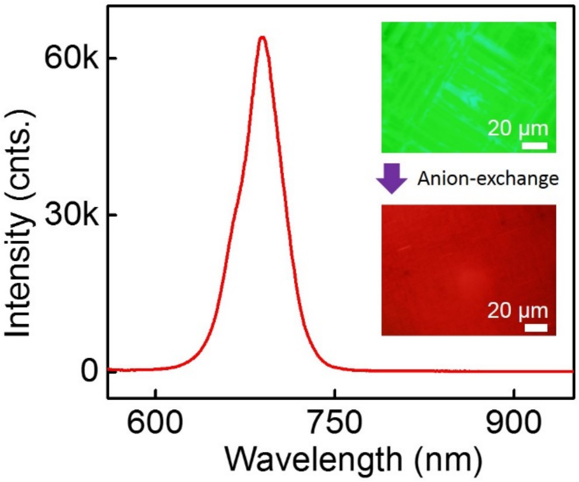

Figure 3.5. PL of $CsPbI_3$ converted from $CsPbBr_3$ by anion exchange. Inset: PL images of $CsPbBr_3$ film before and after anion exchange.

Taking a step further, by using lithographic patterning process, the ion exchange can be conducted in selected region to produce $CsPbBr_3$-$CsPbI_3$ lateral heterojunctions (**Figure 3.6**).

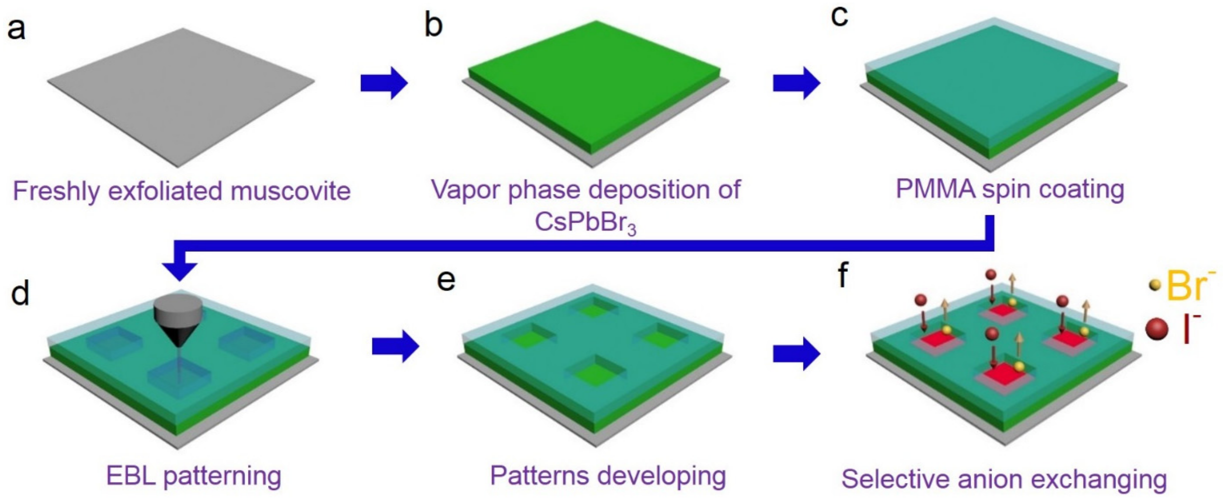

Figure 3.6. Schematic illustration of selective anion-exchange. (a) Muscovite is exfoliated first for the deposition of $CsPbBr_3$; (b) $CsPbBr_3$ thin film was grown on muscovite by vapor phase deposition; (c) PMMA EBL resist was coated on as grown $CsPbBr_3$ thin film; (d) Patterns were defined with EBL; (e) Patterns were developed and area of interest is exposed; (f) Anion exchange was conducted in saturated CsI/IPA solution.

In particular, the fresh mica substrate is first exfoliated for the growth of the $CsPbBr_3$ thin film. Then, a layer of PMMA is spun coating to cover the whole $CsPbBr_3$ thin film, following with the standard electron beam lithography to generate desired patterns which open window for the anion-exchange. The CsI methanol solution is used for the anion-exchange. Since there is a large amount of I^- in the methanol solution and the solubility of CsBr in methanol is comparable to that of CsI, Br^- in the $CsPbBr_3$ lattice will diffuse into the solution with their positions occupied by the I^-. Due to the balance of Br^- and I^- in both the solution and lattice, the Br^- in the lattice cannot be completely replaced by I^-, while the concentration of I^- in solution is considerably higher than Br^-, the Br^- remaining in the lattice is negligible. The area without anion-exchange still emits the green light centered at about 530 nm, corresponding to a bandgap of 2.37 eV. This value is consistent with the original film, indicating that $CsPbBr_3$ is not influenced by PMMA coating. While the area after anion-exchange emits red light centered at about 690 nm, corresponding to a band gap of 1.82 eV (**Figure 3.7(a)**). The two types of material in the heterojunction are shown spatially in PL images. Squares array (**Figure 3.7(b)**), chessboard-like pattern (**Figure 3.7(c)**), and "UCLA" pattern (**Figure 3.7(d)**) are all created after anion-exchange.

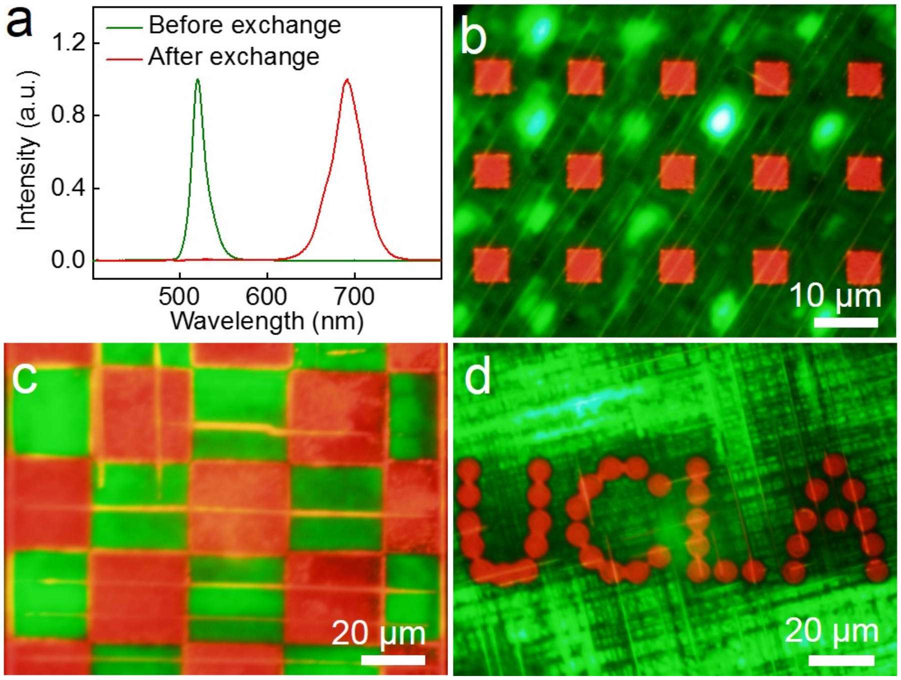

Figure 3.7. PL analyses of $CsPbBr_3$ thin film with selective anion exchange. (a) PL from the original film covered by PMMA and the area after anion-exchange; (b) PL images of squares array pattern with different magnifications; (c) PL image of the chessboard-like pattern; (d) PL images of "UCLA" pattern.

Furthermore, we have conducted electrical measurement across the heterostructure interface, the device structure is shown by PL image in **Figure 3.8(a)**, a clear rectification has been observed (**Figure 3.8(b)**), which can be attributed to the relative band alignment between $CsPbBr_3$-$CsPbI_3$ heterojunction interfaces (**Figure 3.8(c)**). The light illumination will reduce the Schottky barrier formed between the $CsPbI_3$ and Au electrode.

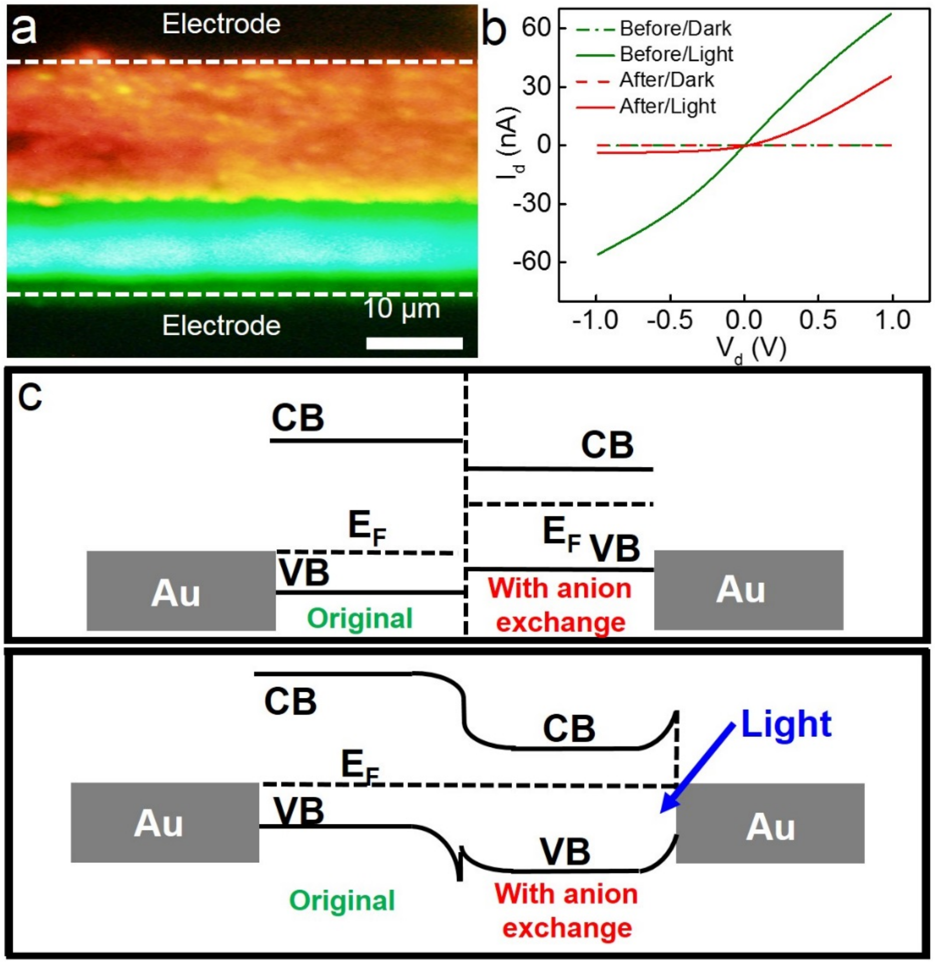

Figure 3.8. Two-terminal I-V measurement before and after anion-exchange and the proposed band alignment. (a) PL image of the heterojunction area after anion exchange. Au electrode regions are dark; (b) Rectification behavior from the heterojunction; (c) Proposed band alignment of $CsPbBr_3/CsPbI_3$ heterostructure, the upper part shows the original alignment without equilibrium and the lower part shows the band alignment at equilibrium.

3.4. Conclusion

In summary, we have demonstrated a single-step vapor phase deposition method for large-scale epitaxial growth of monocrystalline $CsPbBr_3$ thin film with an improved stability towards moisture and heat. We show highly aligned micro-crystal domains can be readily grown on muscovite mica substrates, which can further grow and eventually merge into a large-area monocrystalline $CsPbBr_3$ thin film with an excellent optical quality. The as-grown film provides a critical platform for the device fabrication. Furthermore, we show the $CsPbBr_3$ thin film be readily converted into $CsPbI_3$ through an anion exchange approach, by using the standard electron beam lithography to enable the selective anion-exchange, we demonstrate $CsPbBr_3$/$CsPbI_3$ heterojunction can be produced with arbitrary geometry by design. The capability to grow the monocrystalline $CsPbBr_3$ thin film in a large area and conduct the selective anion-exchange to produce well-defined heterostructures provides a powerful platform for the fundamental investigations on the intrinsic properties of perovskite materials and opens up exciting opportunities to develop optoelectronic devices on the basis of perovskite materials.

3.5 References

1. Kojima, A.; Teshima, K.; Shirai, Y.; Miyasaka, T. *J. Am. Chem. Soc.* **2009,** *131*, 6050-6051.

2. Lee, M. M.; Teuscher, J.; Miyasaka, T.; Murakami, T. N.; Snaith, H. J. *Science* **2012,** *338*, 643-647.

3. Burschka, J.; Pellet, N.; Moon, S.-J.; Humphry-Baker, R.; Gao, P.; Nazeeruddin, M. K.; Grätzel, M. *Nature* **2013,** *499*, 316-319.

4. Docampo, P.; Ball, J. M.; Darwich, M.; Eperon, G. E.; Snaith, H. J. *Nat. Commun.* **2013,** *4*, 2761.

5. Bai, S.; Wu, Z.; Wu, X.; Jin, Y.; Zhao, N.; Chen, Z.; Mei, Q.; Wang, X.; Ye, Z.; Song, T. *Nano Res.* **2014,** *7*, 1749-1758.

6. Manser, J. S.; Kamat, P. V. *Nat. Photonics* **2014,** *8*, 737-743.

7. Nie, W.; Tsai, H.; Asadpour, R.; Blancon, J.-C.; Neukirch, A. J.; Gupta, G.; Crochet, J. J.; Chhowalla, M.; Tretiak, S.; Alam, M. A. *Science* **2015,** *347*, 522-525.

8. Yan, W.; Li, Y.; Li, Y.; Ye, S.; Liu, Z.; Wang, S.; Bian, Z.; Huang, C. *Nano Res.* **2015,** *8*, 2474-2480.

9. Yang, W. S.; Noh, J. H.; Jeon, N. J.; Kim, Y. C.; Ryu, S.; Seo, J.; Seok, S. I. *Science* **2015,** *348*, 1234-1237.

10. Tsai, H.; Nie, W.; Blancon, J.-C.; Stoumpos, C. C.; Asadpour, R.; Harutyunyan, B.; Neukirch, A. J.; Verduzco, R.; Crochet, J. J.; Tretiak, S. *Nature* **2016,** *536*, 312-316.

11. Bush, K. A.; Palmstrom, A. F.; Zhengshan, J. Y.; Boccard, M.; Cheacharoen, R.; Mailoa, J. P.; McMeekin, D. P.; Hoye, R. L.; Bailie, C. D.; Leijtens, T. *Nat. Energy* **2017,** *2*, 17009.

12. Yang, W. S.; Park, B.-W.; Jung, E. H.; Jeon, N. J.; Kim, Y. C.; Lee, D. U.; Shin, S. S.; Seo, J.; Kim, E. K.; Noh, J. H. *Science* **2017,** *356*, 1376-1379.

13. Xing, J.; Liu, X. F.; Zhang, Q.; Ha, S. T.; Yuan, Y. W.; Shen, C.; Sum, T. C.; Xiong, Q. *Nano Lett.* **2015,** *15*, 4571-4577.

14. Zhu, H.; Fu, Y.; Meng, F.; Wu, X.; Gong, Z.; Ding, Q.; Gustafsson, M. V.; Trinh, M. T.; Jin, S.; Zhu, X. *Nat. Mater.* **2015,** *14*, 636-642.

15. Ma, D.; Fu, Y.; Dang, L.; Zhai, J.; Guzei, I. A.; Jin, S. *Nano Res.* **2017,** *10*, 2117-2129.

16. Si, J.; Liu, Y.; Wang, N.; Xu, M.; Li, J.; He, H.; Wang, J.; Jin, Y. *Nano Res.* **2017,** *10*, 1329-1335.

17. Eperon, G. E.; Paterno, G. M.; Sutton, R. J.; Zampetti, A.; Haghighirad, A. A.; Cacialli, F.; Snaith, H. J. *J. Mater. Chem. A* **2015,** *3*, 19688-19695.

18. Liang, J.; Wang, C.; Wang, Y.; Xu, Z.; Lu, Z.; Ma, Y.; Zhu, H.; Hu, Y.; Xiao, C.; Yi, X. *J. Am. Chem. Soc.* **2016,** *138*, 15829-15832.

19. Chen, J.; Fu, Y.; Samad, L.; Dang, L.; Zhao, Y.; Shen, S.; Guo, L.; Jin, S. *Nano Lett.* **2016**.

20. Wang, Y.; Guan, X.; Li, D.; Cheng, H.-C.; Duan, X.; Lin, Z.; Duan, X. *Nano Res.* **2017,** *10*, 1223-1233.

21. Bekenstein, Y.; Koscher, B. A.; Eaton, S. W.; Yang, P.; Alivisatos, A. P. *J. Am. Chem. Soc* **2015,** *137*, 16008-16011.

22. Chen, X.; Peng, L.; Huang, K.; Shi, Z.; Xie, R.; Yang, W. *Nano Res.* **2016,** *9*, 1994-2006.

23. Eaton, S. W.; Lai, M.; Gibson, N. A.; Wong, A. B.; Dou, L.; Ma, J.; Wang, L.-W.; Leone, S. R.; Yang, P. *Proc. Natl. Acad. Sci. U.S.A.* **2016,** *113*, 1993-1998.

24. Fu, Y.; Zhu, H.; Stoumpos, C. C.; Ding, Q.; Wang, J.; Kanatzidis, M. G.; Zhu, X.; Jin, S. *ACS Nano* **2016,** *10*, 7963-7972.

25. Li, X.; Wu, Y.; Zhang, S.; Cai, B.; Gu, Y.; Song, J.; Zeng, H. *Adv. Funct. Mater.* **2016**.

26. Makarov, N. S.; Guo, S.; Isaienko, O.; Liu, W.; Robel, I.; Klimov, V. I. *Nano Lett.* **2016,** *16*, 2349-2362.

27. Zhang, D.; Yang, Y.; Bekenstein, Y.; Yu, Y.; Gibson, N. A.; Wong, A. B.; Eaton, S. W.; Kornienko, N.; Kong, Q.; Lai, M. *J. Am. Chem. Soc.* **2016,** *138*, 7236-7239.

28. Zhang, D.; Yu, Y.; Bekenstein, Y.; Wong, A. B.; Alivisatos, A. P.; Yang, P. *J. Am. Chem. Soc.* **2016,** *138*, 13155-13158.

29. Song, J.; Cui, Q.; Li, J.; Xu, J.; Wang, Y.; Xu, L.; Xue, J.; Dong, Y.; Tian, T.; Sun, H. *Adv. Opt. Mater.* **2017,** *5*, 1700157.

30. Zhang, L.; Shao, Y.; Hao, X.; Wu, Y.; Zhang, H.; Qu, S.; Chen, X.; Xu, X. *CrystEngComm* **2011,** *13*, 5001-5004.

31. Zhang, Q.; Su, R.; Liu, X.; Xing, J.; Sum, T. C.; Xiong, Q. *Adv. Funct. Mater.* **2016,** *26*, 6238-6245.

32. James, D. R.; Liu, Y.-S.; De Mayo, P.; Ware, W. R. *Chem. Phys. Lett.* **1985,** *120*, 460-465.

33. Rakita, Y.; Kedem, N.; Gupta, S.; Sadhanala, A.; Kalchenko, V.; Böhm, M. L.; Kulbak, M.; Friend, R. H.; Cahen, D.; Hodes, G. *Cryst. Growth Des.* **2016,** *16*, 5717-5725.

34. Cha, J.-H.; Han, J. H.; Yin, W.; Park, C.; Park, Y.; Ahn, T. K.; Cho, J. H.; Jung, D.-Y. *J. Phys. Chem. Lett.* **2017,** *8*, 565-570.

35. Chen, J.; Morrow, D. J.; Fu, Y.; Zheng, W.; Zhao, Y.; Dang, L.; Stolt, M. J.; Kohler, D. D.; Wang, X.; Czech, K. J. *J. Am. Chem. Soc.* **2017,** *139*, 13525-13532.

36. Saidaminov, M. I.; Haque, M. A.; Almutlaq, J.; Sarmah, S.; Miao, X. H.; Begum, R.; Zhumekenov, A. A.; Dursun, I.; Cho, N.; Murali, B. *Adv. Opt. Mater.* **2017,** *5*.

37. Shoaib, M.; Zhang, X.; Wang, X.; Zhou, H.; Xu, T.; Wang, X.; Hu, X.; Liu, H.; Fan, X.; Zheng, W. *J. Amer. Chem. Soc.* **2017,** *139*, 15592-15595.

38. Yang, B.; Zhang, F.; Chen, J.; Yang, S.; Xia, X.; Pullerits, T.; Deng, W.; Han, K. *Adv. Mater.* **2017,** *29*.

39. He, Y.; Matei, L.; Jung, H. J.; McCall, K. M.; Chen, M.; Stoumpos, C. C.; Liu, Z.; Peters, J. A.; Chung, D. Y.; Wessels, B. W. *Nat. Commun.* **2018,** *9*, 1609.

40. Zhang, L.; Yang, X.; Jiang, Q.; Wang, P.; Yin, Z.; Zhang, X.; Tan, H.; Yang, Y. M.; Wei, M.; Sutherland, B. R. *Nat. Commun.* **2017,** *8*, 15640.

Chapter 4. Electrical transport probing carrier and photocarrier dynamics in lead halide perovskite thin films with van der Waals contacts

4.1. Introduction

Lead halide perovskites have emerged as an attractive class of low cost, low-temperature processable materials for high performance photovoltaics[1-14], light emitting diodes[15-21] and radiation detection devices[22-25]. Despite tremendous success in the proof-of-concept devices, the fundamental understanding of their charge transport properties is lagging far behind largely due to the extreme difficulties to form high quality electrical contacts. In particular, the halide perovskites are generally soluble in various solvents and incompatible with typical lithography processes that are necessary for microscopic device fabrications; and are highly delicate and prone to degradation during the conventional vacuum metal deposition processes[26-29], which typically involve high-energy atom/cluster bombardments and strong local heating that could seriously damage the underlying halide perovskite materials. Thus, it remains a standing challenge to use conventional lithography to create reliable electrical contacts to halide perovskites. For this reason, the intrinsic electrical transport properties of such perovskite materials are often seriously convoluted/plagued by poor electrical contacts (often with a contact resistance > 3 orders magnitude larger than the intrinsic material resistance) and not fully understood to date.

For example, the space charge limited current (SCLC) model based on Mott-Gurney law are frequently used for evaluating the carrier density and mobility of various perovskites due to the simplicity of the device structure (with perovskite layer sandwiched by two metal electrodes, closely mimicking the well-developed solar cell devices), while this model is only valid for deriving the carrier density and mobility with several critical assumptions. For instance, if the contacts are not Ohmic, the Mott-Gurney law cannot be directly used without accounting for non-ideal injection. Even worse for the typical perovskite devices, substantial current-voltage (I-V) hysteresis loop emerging under large bias voltage could also further convolute with SCLC, bringing additional complications in interpreting the I-V characteristics and compromising the accuracy of the SCLC modeling and the relevant derivations[30-32]. Furthermore, it’s difficult to establish the relationships of light illumination, carrier generation/recombination and carrier transport with SCLC method since the measurements are required to conducted in dark, though such relationships are critical in most optoelectronic applications of perovskites. On the other hand, the non-contact spectroscopic techniques have been explored to probe the basic charge carrier behavior without the contact complication, although these approaches only give an indirect evaluation of local carrier dynamics and often require complex mathematic modeling and derivations[33-35]. A more direct electrical probing long-range charge transport properties is desirable but remains challenging to date.

Hall measurements represent the most direct and preferred method for probing charge carrier behavior with minimum derivations and reduced uncertainties, as well demonstrated and adopted for the evaluation of most conventional semiconductors such as Si and GaAs[36-38]. Despite some pioneering efforts in Hall measurements of perovskite materials with shadow-mask evaporation defined electrodes, these studies are usually complicated and sometimes dictated by the excessive contact resistance, raising uncertainties on the accuracy of the Hall measurements[39, 40]. For example, an analysis of the four-terminal voltage measurement suggests that a reasonably low contact resistance (R_c) and a small contact resistance variation (□R_c) is strictly required in order to accurately determine the intrinsic materials resistance (R_{xx}) and Hall resistance (R_{xy}). An excessive contact resistance or contact resistance variation could lead to substantial errors or even totally invalidate the measurements and the relevant derivations (**Figure 4.2**).

Additionally, it is well known that the halide perovskites feature an ionic “soft-lattice”, with considerable ion movement and current drift at room temperature, which further complicates the accurate measurements and analyses. To address this problem, measurements at the cryogenic temperatures that can reduce or even completely freeze the ion movement, are highly desired for probing the intrinsic charge transport characteristics. However, the quality of electrical contacts usually degrades rapidly with decreasing temperature, for example, the Schottky barrier could dominate the contact at 150 K even though the contact appears Ohmic at room temperature[41, 42]. Therefore, for more reliable measurement and understanding of the fundamental charge transport properties in perovskites, it is critical to create high quality contacts that can sustain cryogenic conditions with reasonably low contact resistance.

Herein, we present a systematic investigation of the long-range carrier and photocarrier transport properties of lead halide perovskite thin films by exploiting high-quality vdW contacts that are reliable from room temperature to cryogenic temperature. Using a vapor phase deposition method, we prepare large-area monocrystalline all-inorganic perovskite thin films with ultra-smooth surface, onto which the prefabricated thin film gold electrodes are directly laminated to form vdW contacts without direct lithography process[43, 44]. Transmission electron microscopy (TEM) studies demonstrate the vdW contacts exhibit an atomically clean interface, in contrast to the deposited contacts with highly disordered interface. Photoluminescence (PL) studies further demonstrate the vdW contacting approach is essentially damage free with no apparent PL degradation, in contrast to the nearly completely quenched PL in perovskites with deposited contacts. Electrical and photoelectrical transport studies with vdW contacts show linear I-V characteristics at both the room temperature and cryogenic temperature, with contact resistance 2-3 orders of magnitude lower than that of the deposited contacts throughout the measurement temperature regime. The vdW-contacted Hall bar devices allow us to conduct highly reliable transport studies at low temperatures, where ion movements are suppressed and the resistance drift is minimized for accurate and robust Hall density and mobility determination. The temperature-dependent carrier mobility studies reveal two scattering regimes: acoustic phonon-dominated scattering regime above 80 K and impurity-dominated scattering regime below 80K, revealing a record-high carrier mobility exceeding 2,000 cm^2/Vs in perovskite thin films at T = 80 K, a large polaron-protected ultralow bimolecular recombination rate of 3.5×10^{-15} cm^3/s at room temperature, and a record-high photocurrent gain of 10^6-10^7 in perovskite thin films. Furthermore, enabled by high quality contacts at the cryogenic temperature, magnetotransport studies for the first time **reveal a quantum interference induced weak localization behavior** in halide perovskite materials with a coherence length up to 49 nm at 3.5 K, comparable to black phosphorus or InSe at a similar carrier density[45, 46], establishing the "soft-lattice" halide perovskites as an exciting class of electronic materials. The preparation of large-area monocrystalline perovskite thin films and the development of damage-free metal integration approach mark important steps toward both the fundamental investigation of the intrinsic electronic properties and exploration of new physics and functions in this unique class of "soft-lattice" materials.

4.2. Experimental section

Chemicals. Hexamethyldisilazane (HMDS, ≥99.0% (GC)).

Materials growth. $CsPbBr_3$ thin film was grown using the same method described in Chapter 3.

Device fabrication. Au electrodes of different geometries with 50-nm thickness are first prepared on silicon substrate with atomically flat surface using standard photolithography and high vacuum e-beam evaporation. Next, a HMDS layer is applied to functionalize the whole wafer and then a

PMMA layer is spin-coated on top of Au electrodes. With the pre-functionalization of HMDS, the PMMA layer has weak adhesion to the sacrifice substrate and can be mechanically picked up using thermal release tape, together with metal electrodes embedded underneath. For large-area transfer on the entire electrode array embedded in the PMMA layer, the thermal release tape with electrodes is laminated to the film directly and heated up to 90 °C to release the PMMA layer. EBL is applied to make windows on PMMA layer, exposing the embedded electrode pads for the following electrical measurement. We note the Au released using this method is atomically flat (replicating the atomically flat surface of the sacrificial wafer), which ensures intimate contact with atomically flat $CsPbBr_3$ thin film. *Deposit approach:* The control device was prepared in an electron beam evaporator. *Mesa isolation:* Hall bar electrodes were prepared with transfer approach and deposit approach mentioned above respectively. The isolation gaps of the mesa and gaps between each electrode were patterned with EBL and developed in 3:1 isopropanol/MIBK developer. The exposed $CsPbBr_3$ was washed away with 1:1 isopropanol/H_2O solution.

Device characterizations. The device characterization was carried out in a commercial PPMS by Quantum Design, Inc. The illumination source is a blue LED installed on the chip carrier, next to the Hall bar, so the relative position between LED and the Hall bar device was fixed no matter how we flipped the chip carrier in the magnetic field. We also added a black box to cover the device and LED on the rotation stage to prevent any change in reflection from the system chamber. The power density of illumination was determined with a power meter (Newport Optical Power Meter 1916-R with measurement head 818-SL). The electrical measurement was conducted with precision source/measure unit (Agilent, B2902A) for DC measurement and with SR830 lock-in preamplifier connected with DL1201 voltage pre-amplifier for low frequency AC measurement. The four-terminal measurement was performed with an excitation current from 10 nA to 50 nA.

The transient photocurrent measurement was carried out by applying a constant voltage (Yokogawa, GS200) to the device, and a pulsed voltage with 10 μs width and 50 ms period (Agilent, 33220A) to the LED. The photocurrent was then amplified through DL1201 current pre-amplifier and recorded using oscilloscope (Agilent, DSO3202A). The equivalent circuit diagram is shown in **Figure 4.1**.

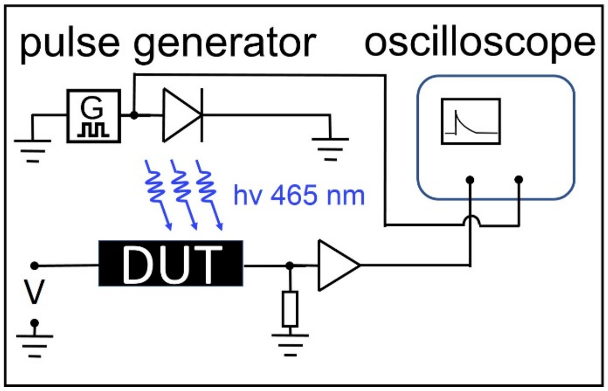

Figure 4.1. The equivalent circuit diagram of transient photo current measurement.

Measurement accuracy analysis. In a standard four-terminal measurement, current is sent through source-drain contacts and voltage drop across the sample is measured using two voltage probes. However, if these two voltage probes have large contact resistance and are not identical, measurement accuracy could be compromised, especially when sample resistance is small compared with the contact resistance. Below, we will discuss this argument in detail.

By analyzing four-terminal measurement schematic (**Figure 4.2(a)**), the accuracy of measurement, defined as $\frac{V_{measure}}{V_{real}}$, can be expressed in the following format:

$$V_{real} = V_2 - V_1 \tag{1}$$

$$V_{measure} = V_4 - V_3 = \left(\frac{V_2}{R_c+\delta R_c+R_{im}} - \frac{V_1}{R_c+R_{im}}\right) \cdot R_{im} \tag{2}$$

So that

$$\frac{V_{measure}}{V_{real}} = \frac{(R_c+R_{im})R_{im}-R_c^2 R_{im} R_{xx}\frac{\delta R_c}{R_c}}{(R_c+R_{im})(R_c+R_c\frac{\delta R_c}{R_c}+R_{im})} \qquad (3)$$

Typically, 10 GΩ is the internal impedance of equipment such as Keysight SMU B2902A and Keithy 2401. For lock-in amplifier, for example SR830 and 5210, the internal impedance is 10 MΩ, and can be extended to 10 GΩ if connected in series with voltage pre-amplifier.

In this way, the accuracy of measurement using R_{im}=10 GΩ can be calculated at various contact resistance (R_c) and contact resistance variation ($\delta R_c/R_c$) for different sample resistance R_{xx}=1.34 kΩ and 25.7 kΩ, and plotted in color scale in **Figure 4.2(b), (c),** respectively. In these plots, the green highlights the measurement window with small errors, and red and blue show regimes with increasing positive and negative errors, and the white area highlights invalid measurement regime. Here 1.34 kΩ is the room temperature sample resistance under 18.8 mW/cm^2 illumination intensity; 25.7 kΩ is the resistance under the same illumination condition but measured at 3.5 K. These plots suggest that in order to accurately measure smaller resistance it requires smaller contact resistance or contact resistance variation, manifested as smaller green area in **Figure 4.2(b)** than in **Figure 4.2(c)**. The black solid lines and the red dashed lines correspond to typical R_c of vdW and deposited contact in ease case. These analyses highlight that, with much lower contact resistance, the vdW-contact devices have sufficient large window (the green area) for accurate measurement of the intrinsic transport properties of perovskites materials. For example, when R_{xx}=25.7 kΩ, R_c is 96 kΩ and $\delta R_c/R_c$ is 0.83 (in the sample with vdW contact $\delta R_c/R_c$ changes from 0.16 at room temperature to 0.83 at 3.5 K), correspond to $\frac{V_{measure}}{V_{real}} = 1.0$ (**Figure 4.2(c)**). On the other hand, there is a little window to achieve accurate measurement with the deposited contact due to excessive contact resistance. For example, if contact resistance is 232 MΩ, a valid voltage measurement is possible only if $\delta R_c/R_c$ is close to zero (**Figure 4.2(c)**), which is not readily achievable in practice. A slight variation of contact resistance with $\delta R_c/R_c = 0.1$ lead to considerable measurement error, with $\frac{V_{measure}}{V_{real}} = -19$.

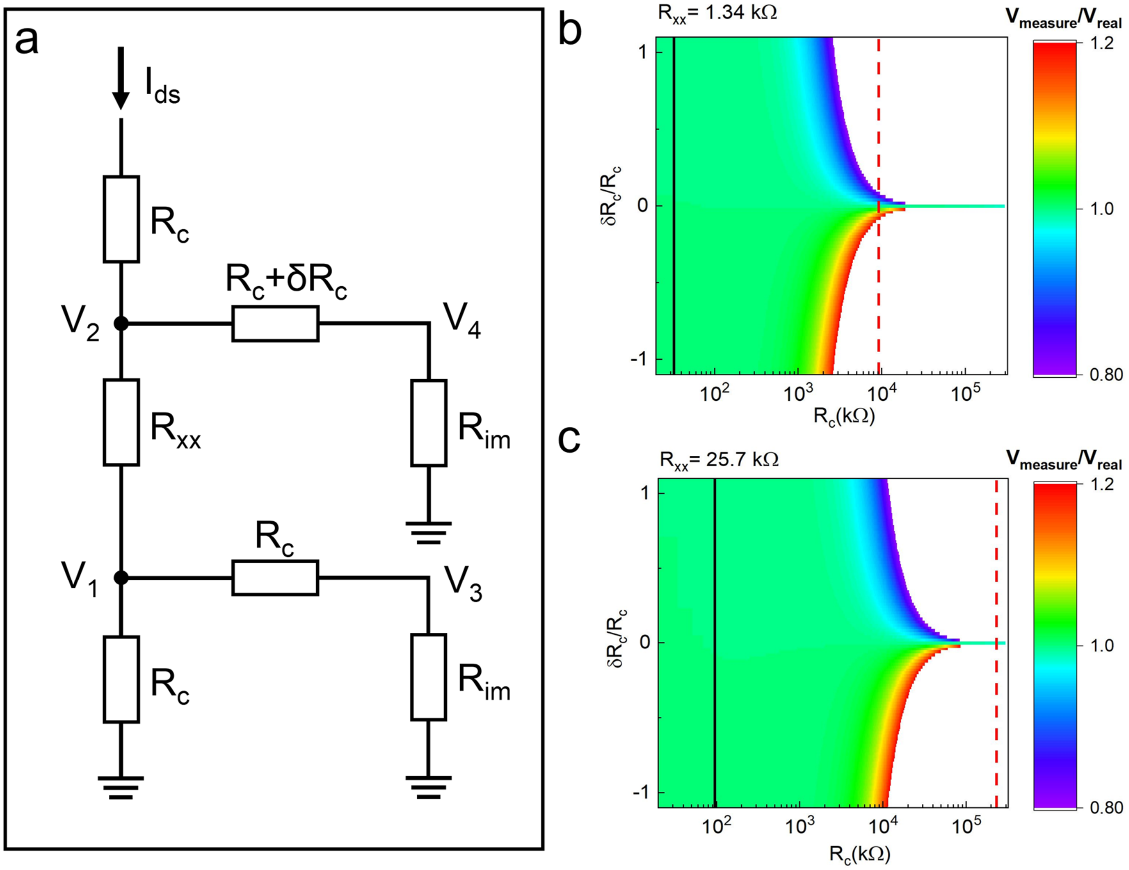

Figure 4.2. Calculation of four-terminal voltage measurement accuracy, in terms of the contact resistance (R_c) and the contact resistance variation ($\delta R_c/R_c$). (a) The equivalent circuit diagram of four-terminal voltage measurement; The red to purple color in (b) and (c) indicates the ratio of measured voltage $V_{measure}$ to the real voltage V_{real} is between 1.2 and 0.8, in which range we assume the measurement is valid. The calculation was performed with instrument impedance R_{im}=10 GΩ and different sample resistance R_{xx}: (b) R_{xx}=1.34 kΩ; (c) R_{xx}=25.7 kΩ. The black solid lines correspond to typical R_c of transferred contact in each case; The red dashed lines are R_c of deposited contact. These analyses highlight that, with much lower contact resistance, the vdW-contacted devices have sufficient large window (the green area) for accurate measurements of the transport properties of charge carriers, while there is a little window to achieve accurate measurements with the deposited contacts due to excessive contact resistance (R_c > 10 MΩ).

4.3. Results and discussion

To evaluate the electronic properties of the resulting $CsPbBr_3$ film, we have fabricated electrical devices for charge transport studies. Since the perovskite thin film is soluble in various solvents, it is not compatible with typical lithography processes that require multiple solvent steps. Additionally, the halide perovskites are rather delicate and may be easily damaged by typical metal deposition processes that usually involve high-energy atom/cluster bombardments and strong local heating[26-29]. Such damage could produce a highly disordered layer seriously plaguing the charge transport across metal/perovskite interface and preventing direct electrically probing the transport properties of such materials. To avoid such complications, we have adopted a vdW integration approach[43], where the prefabricated atomically flat thin film gold electrodes are laminated onto the large area perovskite thin films without any lithography or solvent steps directly performed on perovskites. In brief, gold thin film electrodes with designed geometrical configurations are first prepared on silicon substrate using standard photolithography and high vacuum electron-beam evaporation deposition, and then mechanically released from the substrate and directly transferred onto the perovskite thin film using thermal releasing tape (see **Figure 4.3(a)** and **Experimental section**). The simple physical transfer approach allows the scalable integration of electrode arrays on perovskite thin films over the entire centimeter-scale substrate via the weak vdW interaction (**Figure 4.3(b), (c)**).

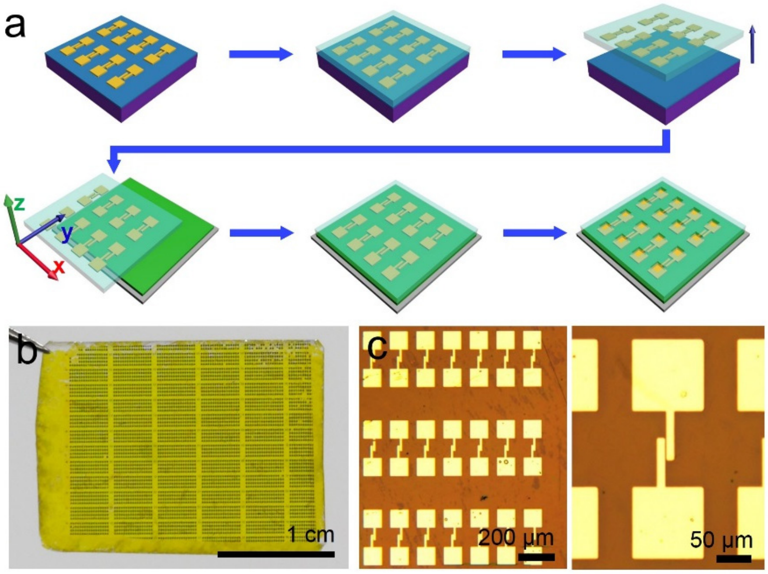

Figure 4.3. Fabrication of damage-free vdW-contacts by transfer approach. (a) Schematic diagram for the transfer contact approach. Au electrodes were firstly prepared on sacrifice substrate; The electrodes were picked up by PMMA layer and thermal release tape; The PMMA layer was transferred to the area of interest; Windows were opened to have external connection to complete electrical measurements; (b) Photograph of transferred electrode arrays on the entire substrate; (c) Photograph of Au electrode arrays transferred on perovskite thin film and zoom-in image of two-terminal device with 2-µm channel.

We have first used PL studies to evaluate the impact from different metal integration approaches. For comparison, we have fabricated electrodes on perovskite thin film by using the conventional vacuum deposition (**Figure 4.4(a)**) and vdW integration approach (**Figure 4.4(c)**). Before the electrodes were peeled off, the photoluminescence images show little emission in the area covered by the metal electrode for both the deposited and vdW contacts due to the blockage of the light by the Au electrodes. We have next tried to peel off the electrodes from the perovskite thin films to expose the underlying perovskite for photoluminescence studies. Apparently, the vdW contacts can be readily peeled off (**Figure 4.4(d)**), while it is much more difficult to peel off the deposited contacts (with much lower peeling off yield) (**Figure 4.4(b)**), suggesting a much stronger interaction between the perovskites and the deposited contacts. Notably, for the area the deposited contacts got peeled off, little photoluminescence emission is observed in the area that was initially covered by the deposited electrodes (outlined by the white dashed lines in **Figure 4.4(b)**) even though there is no apparent optical contrast with surrounding area that was not covered by deposited electrode, suggesting the photoluminescence emission is largely quenched and the underlying perovskite thin film is seriously damaged by the metal deposition process. In contrast, for the area covered by the transferred vdW-contacts, the photoluminescence is essentially unchanged after removing the electrodes (outlined by the white dashed lines in **Figure 4.4(d)**), suggesting that the vdW-contact approach is essentially damage free and exerts no obvious impact to the underlying perovskite thin film, which is also demonstrated in the corresponding photoluminescence spectra (**Figure 4.4(e)**).

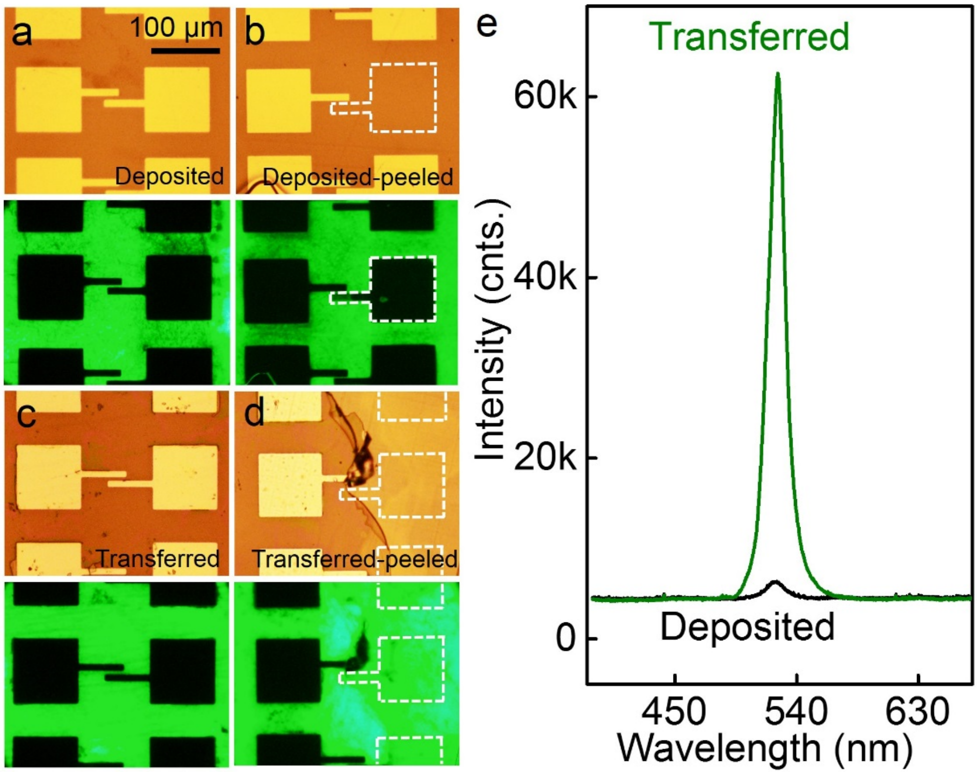

Figure 4.4. PL studies on different metal integration approaches. Photograph (upper panel) and photoluminescence images (lower panel) of deposited electrodes on perovskite thin film before (a) and after (b) the electrodes were peeled off. Photograph and photoluminescence images of transferred electrodes on perovskite thin film before (c) and after (d) the electrodes were peeled off; (e) Photoluminescence emission spectra from the areas where deposited (black) and transferred (green) electrodes were peeled.

We have also conducted cross-sectional TEM studies to examine and compare the structural details of metal/perovskite interfaces obtained by the conventional metal deposition approach and the vdW integration approach. The cross-sectional scanning TEM image of the interface with the deposited gold clearly shows an additional interfacial layer (~ 20-30 nm thick) (**Figure 4.5(a),** with the dash line highlighting zigzag heterogeneous interfacial layer), while the interface with the transferred electrode show a straight sharp interface without obvious interfacial layer (**Figure 4.5(b)**). The HRTEM studies further confirm that the deposited interface is highly disordered (partly amorphous), while the vdW interface show atomically clean and atomically sharp transition from Au lattice to perovskite lattice with no apparent impurities/disorder in-between (**Figure 4.5(c), (d)**). Together, these studies clearly demonstrate that the vdW integration approach offers a damage-free metal-integration process to enable disorder-free metal/perovskite interface that is critical for creating high performance electrical contacts for fundamental investigation of the intrinsic charge transport properties of these delicate materials.

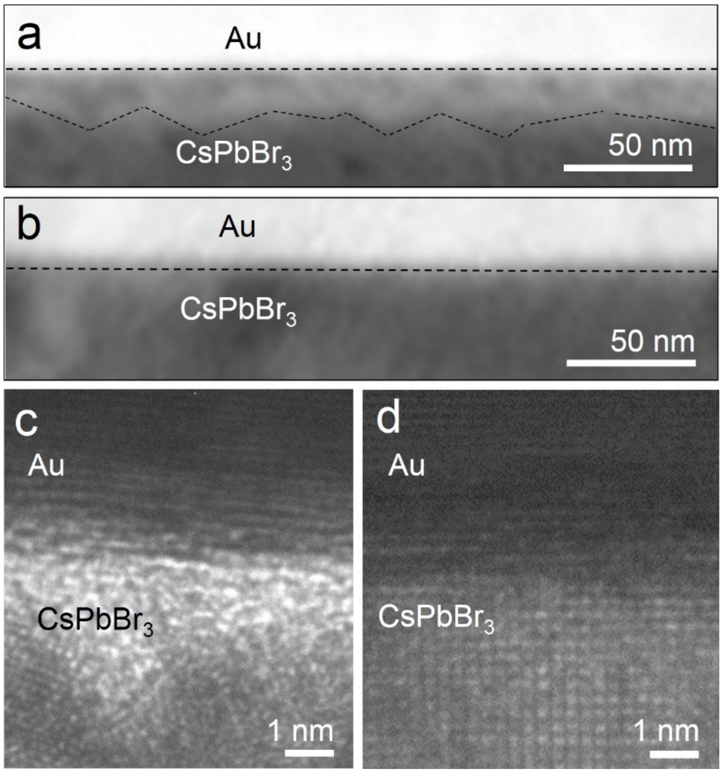

Figure 4.5. Cross-sectional TEM studies on metal/perovskite interfaces obtained by the conventional metal deposition approach and the vdW integration approach. STEM images of the cross-section of $CsPbBr_3$ thin film with the (a) deposited electrodes and (b) vdW-electrodes; The deposited interface shows an additional interfacial layer highlighted by the zigzag lines, and the transferred contact show a straight interface; (c) HRTEM images of the cross-section of $CsPbBr_3$ thin film with deposited electrodes showing disordered interface under electrodes and (d) transferred electrodes showing atomically sharp interfaces.

To verify quality of the vdW-contacts, we have fabricated standard Hall bar devices (**Figure 4.7(a)**) for basic two-terminal current-voltage (I-V) measurements as well as more systematic Hall measurements. The Hall bar electrodes were prepared following the procedures shown in **Figure**

4.3(a), and the mesa of the Hall bar was completely isolated from the surrounding material. For comparison, we have also prepared similar devices with deposited electrodes.

The perovskite devices usually exhibit a rather high two-terminal resistance on the order of GΩ at room temperature that rapidly increases to ~100 GΩ at lower temperatures in dark conditions (**Table 4.1** and **Figure 4.6(a), (b))**, which exceeds the internal impedance of the typical voltmeters and makes it highly unreliable to perform accurate four-terminal measurement to decouple the contact resistance from the intrinsic material resistance, as clearly analyzed in **Figure 4.2**. Therefore, in order to reduce measurement error over a wide temperature range and allow reliable analysis of carrier dynamics over different carrier concentration, we have used variable light illumination to generate and tune the carrier density in perovskite devices to reduce the resistance and enable the measurements (**Figure 4.6(c)**).

Table 4.1. Room temperature two-terminal sheet resistance, apparent resistivity, along with device geometry and two-terminal current of perovskite devices in dark reported previously and this work.

Materials	Channel length, width and thickness	Dark current (nA/V)	Two terminal sheet resistance (GΩ/□)	Resistivity (Ω·cm)	Ref.
$MAPbBr_3$ single crystal	500 µm, 750 µm, 250 µm	0.13	**10.65**	2.7×10^8	40
$MAPbBr_3$ single crystal	Two corners in vdP, 2000 µm, 2000 µm	6.13	**0.19**	3.8×10^7	47
$MAPbBr_3$ single crystal	5 µm, 1000 µm, 50 µm	0.5	**400**	2×10^9	48
$CsPbBr_3$ single crystal	100 µm, 300 µm, 0.5 µm	0.01	**300**	1.5×10^7	49
$CsPbBr_3$ single crystal	1000 µm, 150000 µm, 1000 µm	~1	**~150**	1.5×10^{10}	50

$CsPbBr_3$ monocrystalline film	5 µm, 1000 µm, 200 µm	~1	**~200**	4×10^9	51
$CsPbBr_3$ monocrystalline film	150 µm, 100 µm, 1 µm	0.32	**2.1**	2.1×10^5	This work

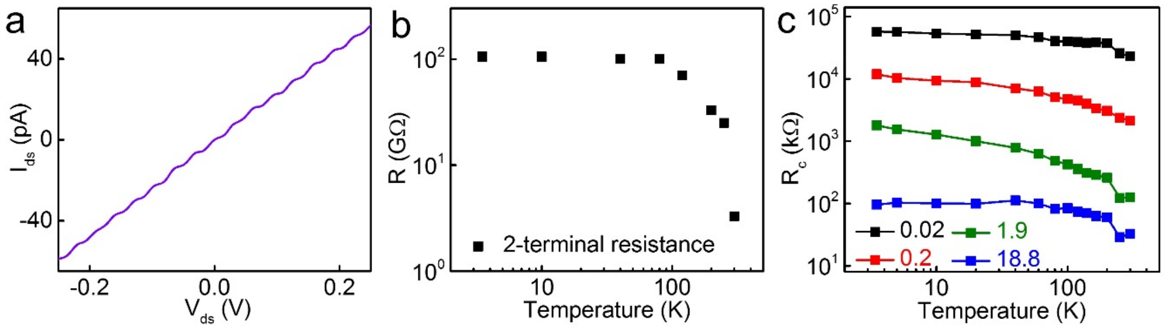

Figure 4.6. Temperature-dependent resistance measurement. (a) Dark I-V curves measured at room temperatures; (b) Two-terminal resistance in dark at different temperatures. The two-terminal resistance increased dramatically with decreasing temperature; (c) Contact resistance vs. temperature under different illumination power density. The contact resistance shows similar temperature dependent trend at different illumination power density.

The simple two-terminal I-V of a device with deposited contacts at 300 K (under a blue LED illumination at 18.8 mW/cm^2) shows non-linear I-V behavior with a typical two-terminal sheet resistance > 20 MΩ/□ (blue curve in **Figure 4.7(b)**). The two-terminal resistance obtained with deposited contact is largely consistent with previous studies (**Table 4.2**). In contrast, two-terminal I-V measurement of the device with vdW contacts under the same conditions exhibits linear I-V behavior with the two-terminal sheet resistance on the order of **100 kΩ/□** (red curve in **Figure 4.7(b)**), about two orders of magnitude lower than that of the device with deposited contacts. The much higher sheet resistance observed in the same material with deposited contacts suggests the charge transport in such devices is dictated by the contact resistance rather than the intrinsic material resistance. At the same time, much higher current observed in the vdW-contacted devices indicates the contact resistance is greatly reduced.

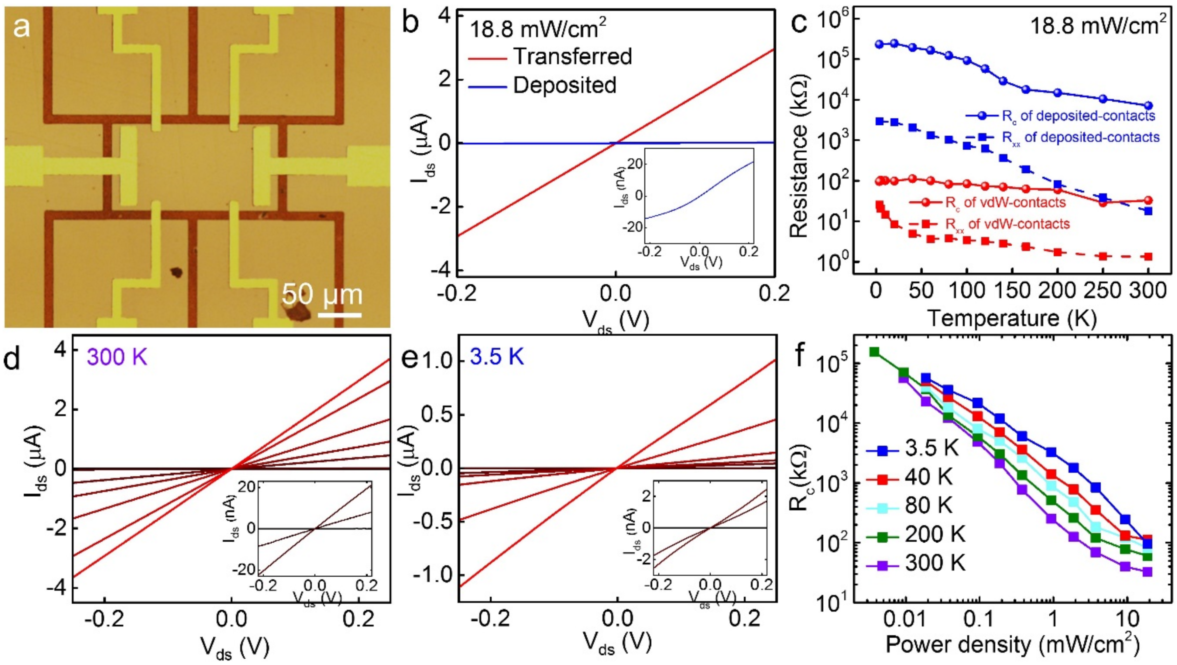

Figure 4.7. Performance of the vdW contacts. (a) Photograph of a typical Hall bar device prepared by vdW-contact approach; (b) Room temperature I-V of the devices with deposited (blue) and vdW (red) contacts under a blue LED illumination power density of 18.8 mW/cm^2; Inset: zoomed in IV plots for device with deposited contacts. (c) Comparison of the contact (dot) and channel (square) resistance of the devices with deposited and vdW-contacts at various temperatures; (d, e) I-V characteristics of the vdW-contacted device at room temperature (d) and 3.5 K (e) under various illumination intensities; the power density for each curve (from back to red) is 0, 0.01, 0.1, 0.9, 1.9, 3.8, 9.4, 18.8 mW/cm^2 respectively; Insets: zoomed in I-V plots under 0 (**Figure 4.6(a)**), 0.01 and 0.1 mW/cm^2 illumination. (f) Illumination power dependent contact resistance of the vdW contacts at different temperatures.

Table 4.2. Room temperature two-terminal sheet resistance, resistivity, along with device geometry, and two-terminal current of $CsPbBr_3$ devices under similar illumination, reported in the literature and this work.

Materials	Channel length, width and thickness	Illumination power density (mW/cm^2)	Current (nA/V)	Two terminal sheet resistance (MΩ/□)	Resistivity (Ω·cm)	Ref.
$CsPbBr_3$ bulk single crystal	1000 μm, 150000 μm, 1000 μm	106	2000	**75**	7.5×10^6	50
$CsPbBr_3$	5 μm,	2.7	1500	**133**	2.66×10^6	51

film by micro plates	1000 µm, 200 µm					
$CsPbBr_3$ monocrystal line film	50 µm, 1000 µm, 7 µm	100	438	**46**	3.22×10^4	7
$CsPbBr_3$ monocrystal line film,	150 µm, 100 µm, 1 µm	18.8	75	**20**	2×10^3	This work, deposited contact
$CsPbBr_3$, monocrystal line film,	150µm, 100 µm, 1 µm	18.8	17500	**0.04**	4	This work, vdW contact

We have further derived and compared the contact resistance observed in the devices with deposited and vdW-integrated contacts (**Figure 4.7(c)**). To this end, we have first obtained the channel resistance R_{xx} using four-probe measurements with the standard Hall bar device (**Figure 4.7(a)**). The contact resistance was then calculated by subtracting the channel resistance (R_{xx}) from two-terminal resistance (dV/dI near zero voltage). The contact resistance for the deposited contact is on the order of 10-100 MΩ, while that for the vdW-contact is on the order of 100 kΩ. Throughout the entire measurement regime, the contact resistance of vdW-contacted devices is ~2-3 orders of magnitude lower than that of the deposited contacts, which may be largely attributed to the atomically clean interface at the vdW contacts[43, 44]. The channel resistance (R_{xx}) measured from the devices with vdW-contacts or deposited-contacts show a similar trend with temperature, but with R_{xx} value determined from deposited contacts more than 10 times larger (**Figure 4.7(c)**), which might be partly attributed to deposition-induced material damage beyond the direct contacting region (as also indicated by dark streaks between contact pads in PL images in **Figure**

4.4(a), (b)). Additionally, the R_{xx} determined from deposited contacts might not be so accurate due to the excessive contact resistance (particularly in the low temperature regime) based on our analysis shown in **Figure 4.2**. Notably, the measured channel resistance (1-100 kΩ) is much lower than the contact resistance (**Figure 4.7(c)**), further confirming the typical two-terminal transport is dictated by the contact resistance, especially in the samples with deposited contacts.

To further evaluate the quality of the vdW-contacts, the illumination intensity-dependent I-V were collected from 18.8 mW/cm^2 to completely dark. The I-V remain linear at all illumination conditions (**Figure 4.7(d)** and **Figure 4.6(a)**). Temperature dependent studies further show that linear I-V characteristics persist even at the base temperature of our measurement system (3.5 K) in the vdW-contacted devices (**Figure 4.7(e)**), which is an important prerequisite for performing reliable four-terminal resistance study at low temperature. The summary of the contact resistance under variable light illumination conditions and different temperatures is shown in **Figure. 4.7(f)**. Here the R_{xx} measurements were conducted with an illumination power above 0.003 mW/cm^2 to ensure a more reliable evaluation of the carrier and photocarrier transport characteristics. At all temperatures, the contact resistance decreases with increasing illumination power, indicating the importance of carrier generation for reducing contact resistance. At a fixed illumination power density, the R_c increases monotonically with decreasing temperature (**Figure 4.6(c)**). The increases of contact resistance at the lower temperature regime is not surprising, since current passing through a Schottky barrier is proportional to $T^2\exp(\frac{\phi_B}{kT})$, where k is the Boltzmann constant and ϕ_B is the Schottky barrier height[42].

With our unique contact and measurement approach, we have conducted systematic Hall measurements to probe the long-range carrier transport characteristics in such perovskite materials. To conduct reliable Hall measurements, it is critical to maintain a stable sample condition during the magnetic field sweeping process, so that the R_{xx} and R_{xy} can be accurately determined without other extrinsic variations. This is particularly challenging for halide perovskite materials due to considerable bias-induced ion movement and current drift over time. To this end, we have first monitored sample resistance drift vs. time at different temperatures (**Figure 4.8(a)**). Expectedly, there is a large R_{xx} drift at 300 K, consistent with previous studies and may be attributed to ion movement in such "soft-lattice" materials under a constant bias[52, 53], which can be suppressed at low temperature. Indeed, such drift rapidly decreases at lower temperature and essentially vanishes below 200 K.

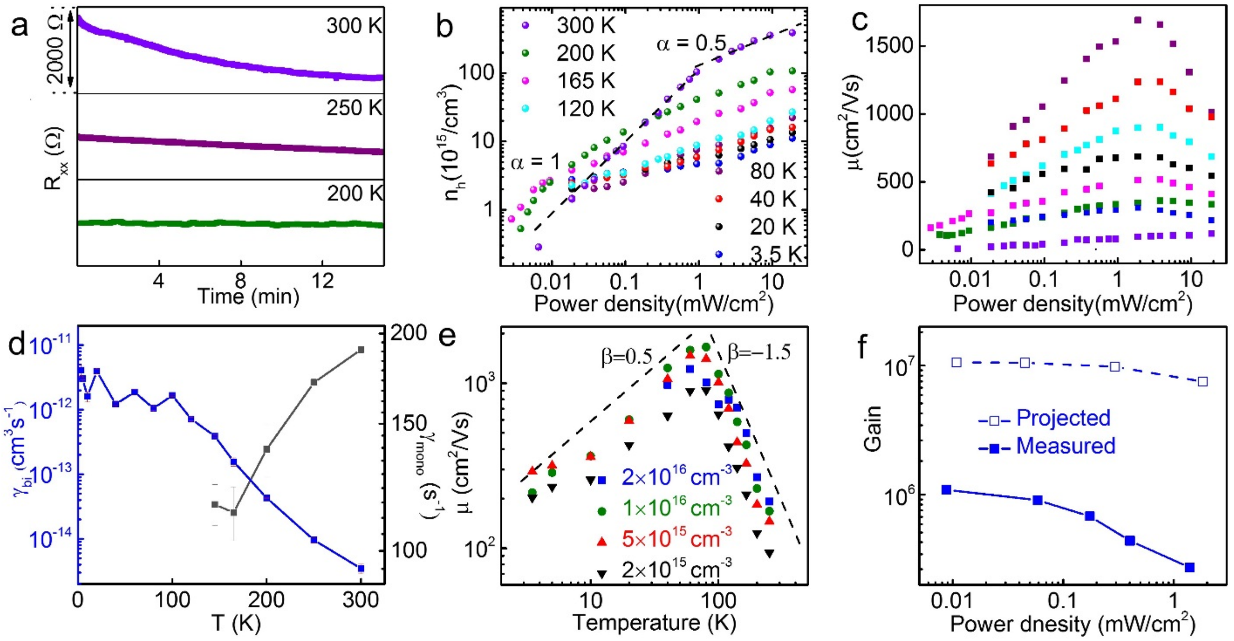

Figure 4.8. Electrical probing the intrinsic transport properties of perovskites using vdW-contacts. (a) Resistance drift at different temperatures, highlighting considerable resistance drift due to bias-induced ion movements at room temperature, which can be completely frozen out with no drift below 200 K; (b) Illumination power dependent carrier density n_h at different temperatures, the dashed lines follow P and $P^{0.5}$; (c) Illumination power dependent Hall mobility at different temperatures (same color code as that shown in (b)); (d) The extracted temperature dependent mono-molecular (black) and bi-molecular (blue) electron-hole recombination rate from (b); (e) Hall mobility as a function of temperature at different carrier densities. The dashed lines follow $T^{0.5}$ and $T^{-1.5}$. (f) Photocurrent gain values of device with 2 μm channel length. The calculated result using $\tau_{\text{lifetime}}/\tau_{\text{transit}}$ is plotted in dashed line.

For a robust Hall measurement, a linear relationship between Hall resistance R_{xy} vs. magnetic field B with a constant Hall slope is needed for deriving the carrier density and mobility. However, due to the considerable resistance drift at room temperature, we were not able to accurately derive Hall resistance R_{xy} while sweeping the magnetic field over a finite amount of time (on the order of 10 minutes during which there is usually serious bias-induced drift at room temperature), since magnetic field induced change of R_{xy} would inevitably convolute with the much larger bias-induced drift (**Figure 4.9(a)**). To this end, to minimize the bias-induced drift during the relatively long time period needed to sweep the magnetic field, we mechanically flipped the device in a fixed magnetic field to measure the abrupt change of Hall resistance when the magnetic field was inversed in a much shorter time scale (< 10 seconds) to avoid the complication from the slow ionic movement induced resistance drift (**Figure 4.9 (b)**). In this way, a linear R_{xy}-B relationship with a constant Hall slope can be obtained at room temperature both in dark and under light illumination (**Figure 4.9 (c), (d)**). In particular, the Hall measurement gives a dark carrier density (4.8×10^{13} cm^{-3}) and mobility (7.5 cm^2/Vs) without illumination.

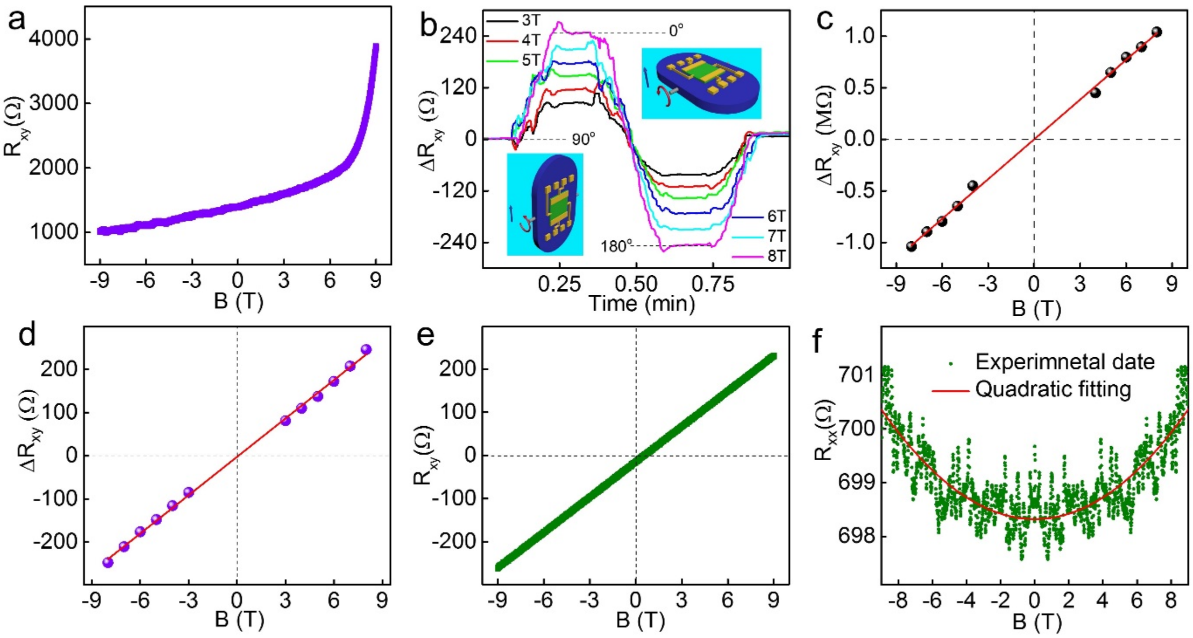

Figure 4.9. Representative magnetoresistance at both room temperature and low temperature. (a) Room temperature Hall resistance R_{xy} measured with sweeping magnetic field. The magnetic field induced change of R_{xy} is highly convoluted with the much larger ion-movement induced drift, and may not be used to accurately determine the Hall resistance; (b) Change of R_{xy} at room temperature by mechanically flip the device in a constant magnetic field; Inset: cartoon of measurement set up. (c), (d) Reduced room temperature Hall resistance ΔR_{xy} measured with flipping the device in different magnetic field measured in dark (c) and under 2.7 mW/cm^2 illumination (d) Red lines are the linear fit of data, which give Hall slopes of 130000 Ω/T and 29.7 Ω/T; (e) Linear response of R_{xy} while magnetic field is varied continuously at 200 K, where ion movement induced drift is minimized; (f) Longitudinal magnetoresistance and its quadratic fitting. Data in (e) and (f) was taken at T = 200 K under illumination power density of 2.7 mW/cm^2 in sample B.

On the other hand, when resistance drift is eliminated below 200 K, we can conduct the reliable Hall measurements using the standard approach with the sweeping magnetic field. Nonetheless, no consistent Hall slope can be achieved at lower temperature in dark due to rapidly increasing resistance (e.g., 35 GΩ at 200K) and the associated measurement errors (**Figure 4.6(b)**). Therefore, to ensure more reliable measurements and more accurate analyses of carrier dynamics across a wide temperature range, we have conducted systematic Hall measurement under variable light illumination. The R_{xy} taken while sweeping magnetic field at 200 K shows a perfect linear relationship vs. magnetic field B with a constant Hall slope and nearly zero intercept at B = 0 T and (**Figure 4.9(e)**), demonstrating highly reliable Hall measurements with the vdW-contacted device at low temperature. To the best of our knowledge, such a linear relationship with a constant Hall slope and a nearly zero intercept has not been reported for the similar halide perovskites before, highlighting the importance to achieve high quality contacts for reliable Hall measurements at low temperature where ion movements are frozen.

With the established measurement protocols for reliable determination of Hall slope at both room temperature and low temperature, we can derive carrier density and mobility at various illumination conditions. The Hall measurement indicates that the transport is dominated by holes.

Here we show the demonstration of decoupling of electron and hole mobility with magnetoresistance measurement (**Figure 4.9(e), (f)**) as followed.

The analysis was conducted by considering two possible scenarios. First, if we assume both types of photo-generated carriers are free carriers, these two types of carriers have the same density ($\Delta n_p = \Delta n_e$) since the photogenerated carriers are greatly more than the dark carriers. Based on this assumption, our two-carrier Hall measurement and analysis reveals that the hole mobility is much greater than the electron mobility (~60 times), i.e., the hole mobility dictates the overall Hall mobility. The rather low electron mobility suggests that most electrons are not very mobile or likely trapped in electron deep levels, the method is shown in detail, the longitudinal and transverse magnetoresistance can be written as[42]:

$$\rho_{xx} = \rho_0\left(1 + \mu_p\mu_n B^2\right) = \rho_0 + AB^2 \qquad (4)$$

$$\rho_{xy} = \mathrm{B}\,\rho_0(\mu_p - \mu_n) \qquad (5)$$

And hereby,

$$\mu_p = \frac{R_H + \sqrt{R_H^2 + 2A\rho_0}}{2\rho_0},\ \mu_n = \frac{A}{2\rho_0\mu_p} \qquad (6)$$

where μ_p and μ_n are hole and electron mobility, respectively. R_H is the Hall slope and ρ_0 is the sample resistance at zero magnetic field. Parameter A can be obtained by quadratic fitting of R_{xx} vs. B curve and R_H can be calculated using Hall trace. This offers a way to decouple hole and electron mobility from Hall mobility. Following this method and using data shown in **Figure 4.9(e), (f)**, we got μ_p equal to 395.5 cm^2/Vs, much greater than μ_n which is 4.537 cm^2/Vs. Here μ_n is only 1.5% of μ_p.

Second, if we treat the trapped electrons as fixed charges instead of mobile charge carriers, we have $\Delta n_p \gg \Delta n_e$, the measured Hall mobility simply represents hole mobility. Thus in either case, our studies suggest that the overall transport is dictated by hole transport, and the Hall mobility gives a rather accurate measure of the *hole* mobility. On the other hand, since the transport is dominated by the holes in our system, the electron mobility cannot be accurately determined, as is the case for any semiconductors.

Therefore, we conclude that the dominated transport carriers are holes. Since we do not know the exact density of mobile electrons, we cannot derive the exact mobile electron mobility. **The decoupled electron mobility from our method represents the "average" mobility of trapped electrons and mobile electrons**, which is very small compare to the "average" hole mobility.

We note that the electron/hole mobility difference has been recognized in other experiments. For example, the THz measurements with extra porous TiO_2 or AlO_x layer as filters to enable selective measurements in $MAPbI_3$ reveals an electron mobility/hole mobility ratio ranging from 1/1.3[54] to 1/6[55] (with total mobilities ranging from 800 $cm^2V^{-1}s^{-1}$ to 20 $cm^2V^{-1}s^{-1}$)[55, 56] . Other contactless method such as photo illumination quench method reported that the electron and hole mobility in $FAPbI_3$ have a ratio of less than 1/15[57]. Overall, these studies show a trend that hole mobility is generally higher than electron mobility, but the actual ratio and exact value are quite different from each other, which further highlight the complexity of the matter and the critical need to conduct more reliable measurements to fully understand the transport dynamics in halide perovskites.

With carrier concentration (n_h) increases with increasing illumination, following $n_{\mathrm{h}} \propto \frac{P}{\gamma_{\mathrm{mono}}}$ in the low illumination regime (e. g. $P < 1$ mW/cm^2 at room temperature) where the trap assisted electron-hole recombination dominates; and $n_{\mathrm{h}} \propto (\frac{P}{\gamma_{\mathrm{bi}}})^{0.5}$ in the high illumination regime where the band to band electron-hole recombination dominates (**Figure 4.8(b)**)[39]. Here, P is the illumination power density, γ_{mono} and γ_{bi} represent single molecule and bi-molecule recombination rate, respectively.

The γ_{mono} and γ_{bi} show distinct temperature dependence (**Figure 4.8(d)**). The γ_{mono} becomes smaller at lower temperature, suggesting a reduced single molecular recombination probability when the kinetic energy is suppressed. The transition point of monomolecular to bimolecular recombination regime moves to lower illumination power density with decreasing temperature. Below 140 K the bimolecular recombination dominations the whole measurement range, therefore we couldn't acquire γ_{mono}. On the other hand, γ_{bi} show a monotonic increase with reducing temperature. This trend cannot be explained by previously suggested spin-split indirect band picture [58] or mobility dependent picture[59]. On the other hand, it has been proposed that electrons and holes are dressed in phonon excitations in the "soft lattice" halide perovskite materials, forming polarons. Such electron and hole polarons have different effects on structural bending, so it is energetically more favorable if they are spatially separated. The reduced carrier-phonon coupling at low temperature weakens the polaronic effect and hence increases bimolecular recombination rate. Such a picture is consistent with our observed temperature dependent trend (**Figure 4.8(d)**, blue line). Moreover, within the electron and hole polaron picture, a spacing is needed to be overcome before they recombine, which could greatly slow the bimolecular recombination rate[53, 60]. Indeed, a bimolecular recombination rate as low as $3.5 \times 10^{-15} cm^3/s$ is observed at room temperature, which is about 4 orders of magnitude lower than that of typical direct band semiconductors (e.g., $\sim 10^{-10} cm^3/s$ in GaAs) and nearly comparable to that in indirect bandgap semiconductors ($10^{-14} - 10^{-15} cm^3/s$ in 10^{-14}-10^{-15}cm$^3/s$ in Si and Ge). Additionally, this recombination rate is also about 2 orders of magnitude lower than that in hybrid perovskite $CH_3NH_3PbI_3$[55, 61, 62].

Based on the recombination rate, we have further extracted carrier recombination lifetime. We extracted the carrier recombination lifetime $\tau_{lifetime}$ through the carrier recombination rate following:

$$\frac{1}{\tau_{lifetime}} = \gamma_{mono} + \frac{\gamma_{bi}}{n} \tag{7}$$

And from the transient photocurrent following:

$$I(t) = I_0 \exp(-t/\tau_{lifetime}) \tag{8}$$

where I_o is the maximum two-terminal current after pulsed LED illumination.

The photocurrent gain then can be calculated using:

$$G = \frac{\tau_{lifeitme}}{\tau_{transit}} = \frac{\tau_{lifetime}\mu V_s}{l^2} \tag{9}$$

Where V_s is the voltage drop across sample and l is the device channel length. Thus, within the same material, the photocurrent gain of two devices with different channel length l_1 and l_2 should have $\frac{G_1}{G_2} = \frac{l_2^2}{l_1^1}$.

On the other hand, the photocurrent gain at a fixed voltage can be directly deducted from IV characteristic, following:

$$G = \frac{hc}{e\lambda}\frac{I}{PA} \tag{10}$$

where A is the channel area, P is the illumination power density, h is the Planck constant, c is the velocity of light, e is the elementary charge, and λ is the wavelength of incident light.

The recombination life time τ_{lifetime} decreases from 5.3 ms to 0.6 ms as illumination power density increases from 0.01 mW/cm^2 to 18.8 mW/cm^2, which is consistent with previous study[9], and matches well with the extracted carrier lifetime from transient photocurrent decay measurement (**Figure 4.10**).

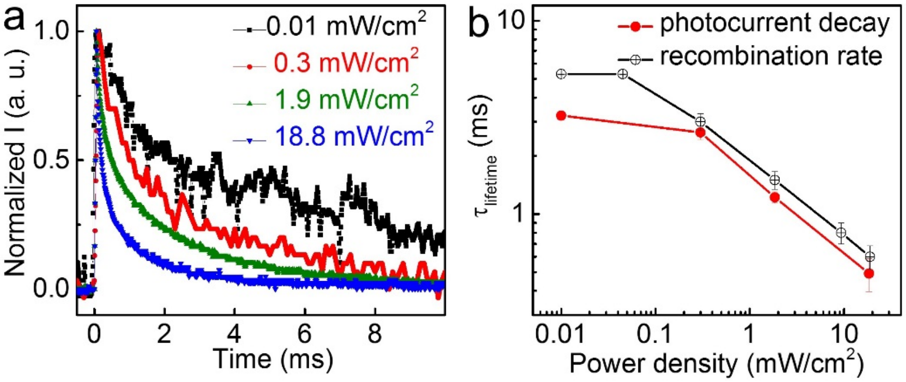

Figure 4.10. Transient photocurrent and carrier lifetime at room temperature. (a) The normalized photocurrent responses under different illumination intensities; (b) Comparison between the extracted carrier recombination lifetime from the photocurrent in (a) and from the recombination rate in **Figure 4.8(d)**.

The reliable Hall measurements allows to further derive the carrier mobility at various temperature and illumination intensity. A Hall mobility > 100 cm^2/Vs at room temperature, which increases up to 1650 cm^2/Vs at 80 K (**Figure 4.8(c)**). At each temperature, the mobility first increases with the increasing illumination power, which is because larger carrier density increases Fermi wave vector, and thus reduces back-scattering probability. On the other hand, as density further increases, carrier-carrier interaction starts to play a dominant role, leading to reduced mobility under even stronger illumination conditions (**Figure 4.8(c)**)[63]. The highest mobility achieved among all measured samples is 2080 cm^2/Vs at 80 K.

At a given carrier density (**Figure 4.8(e)**), for example at $n_h = 1 \times 10^{16}$ cm^{-3}, the mobility vs. temperature relationship above 80 K follows a negative power law: $\mu \propto T^{-\beta}$ with $\beta \sim 1.46$. This power law is consistent with the classical theory of acoustic phonon-electron scattering dominated scheme, where $\mu \propto T^{-1.5}$ is expected[42], however the theoretically predicted room temperature mobility within this picture exceeds 1,000 cm^2/Vs in $MAPbI_3$ and $MASnI_3$ perovskites[64-67], while our highest mobility measured at room temperature is 120 cm^2/Vs. On the other hand, the negative scaling law can also be explained by the formation of large polaron in halide perovskite[53]. In particular, the polaronic effect involving acoustic phonons would also give the same power law $T^{-1.5}$ scaling behavior. With this picture, a much lower mobility value is predicted due to increased electron-phonon interaction and increased effective mass (10 cm^2/Vs at 300 K and 150 cm^2/Vs at 100 K)[68], but we should note that the exact calculated mobility value could vary substantially depending on the effective mass and assumed impurity density used in the calculation. By considering the polaronic effect involving polar-optical phonons, theoretical studies predict $T^{-0.5}$ scaling relationship above 100 K and an increased power factor at lower temperature[69], thus we cannot completely exclude the polar-optical phonon scattering model simply based on the temperature scaling behavior. Below 80 K, our studies show the mobility decreases with reducing temperature at all illumination conditions, which suggests that the classical impurity scattering process dominates the back-scattering related transport in this temperature region[42].

The growth of high-quality perovskite thin film with excellent optical and electronic quality and the integration of van der Waals contacts open exciting opportunities for creating high performance optoelectronic devices. For example, in the simplest photoconductor, the critical device parameter, photocurrent gain, is directly determined by the carrier lifetime τ_{lifetime} and transit time τ_{transit}, which is in turn related to carrier mobility (μ), the bias voltage (V) and the channel length (L) following the equation below.

$$G = \frac{\tau_{\text{lifeitme}}}{\tau_{\text{transit}}} = \frac{\tau_{\text{lifetime}}\mu V}{L^2} \qquad (11)$$

With the unusual combination of long carrier lifetime and high carrier mobility, the perovskite thin films exhibit an unusually large value of $\tau_{\text{lifetime}}\mu$ product and thus offers the material foundation for an exceptionally high photocurrent gain. To further push the limit of the photocurrent gain, it is necessary to shorten the channel length and reduce the transit time, which has been difficult to achieve in perovskite materials due to its incompatibility with the typical lithography process that are necessary for creating high-resolution devices (previous devices was usually fabricated using shadow mask approach with channel length of ~50 μm or larger). With our vdW-integration approach using photolithography patterned electrodes, the channel length can be readily scaled to micrometer scale to achieve ultrahigh gain.

To this end, we have fabricated a two-terminal device with 2 μm channel length and studied its photoresponse characteristics (**Figure 4.11**). Based on the lifetime and mobility obtained from Hall measurements, we can calculate the upper limit of the photocurrent gain based on the same device geometry (**Figure 4.8(f),** dashed line). The calculated photocurrent gain exceeds 10^7 at 2V bias, and decreases with increasing illumination power density, which is resulted from the sub-linear behavior of photocurrent. Remarkably, the measured photocurrent gain shows a similar trend (solid line in **Figure 4.8(f)**), with a highest gain of 1.2×10^6 achieved at 2 V bias at 0.01 mW/cm^2 illumination. To the best of our knowledge, the gain of $>10^6$ represents the highest value ever reported among all photoconductors made from perovskite materials (~10^0-10^5 under similar illumination conditions reported previously, see **Table 4.3** for more details). It is noted that our measured photocurrent gain values are about one orders of magnitude smaller than the calculated ones. This difference is because our calculation assumes 2V bias drop entirely on the perovskite channel, while the actual voltage drop on the channel of the two-terminal device is much smaller due to considerable contact resistance (about one order of magnitude higher than the channel resistance, see **Figure 4.7(c)**). We also note that the difference between calculated and measured gain values becomes smaller at lower illumination, which may be partly attributed to higher R_{xx}/R_c ratio at lower illumination and larger fraction of voltage drop in the channel. To this end, by further reducing the illumination, an even higher gain of 8.7×10^6 is achieved (**Figure 4.11**). This analysis demonstrates that despite considerable improvement and record high gain achieved in our device, the ultimate material potential is not yet reached, and the gain can be further improved significantly by further optimizing the contact.

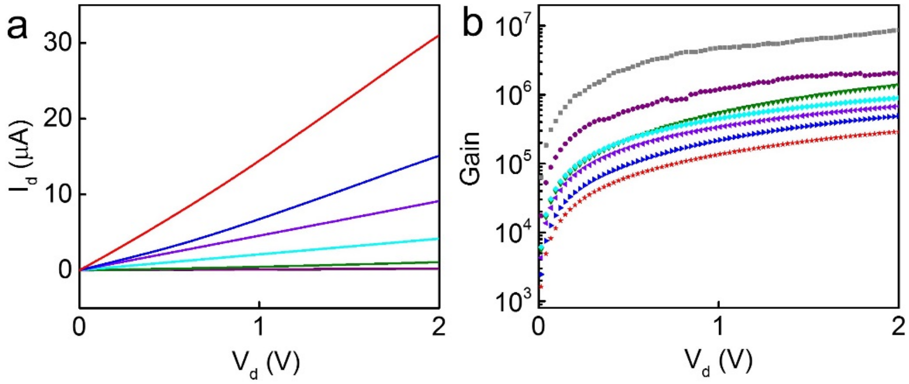

Figure 4.11. I-V and corresponding photocurrent gain of a two-terminal device. The illumination power densities are 0 (black), 0.00005 mW/cm^2 (gray), 0.0005 mW/cm^2 (purple), 0.009 mW/cm^2 (green), 0.059 mW/cm^2(light blue), 0.174 mW/cm^2 (violet), 0.401 mW/cm^2 (dark blue), 1.4 mW/cm^2 (red) respectively. (a) I-V and (b) gain of device with geometry of 2 μm (L) ×10 μm (W).

Table 4.3. Comparison of photocurrent gain reported in the literature and this work. The device configurations, material types, responsivities are also provided.

Device configuration	Material type	Responsivity (A/W)	Gain	Ref.

ITO/$CsPbBr_3$/ITO	Nanosheets film	0.64 (10 V)	0.54	70
Au/$CsPbBr_3$/Au	Nanoparticle film	0.18 (10 V)	0.41	71
Au/$CsPbBr_3$/Au	Porous film	2.7 (9 V)	6.6	72
Au/$CsPbBr_3$/Au	Single crystal	2 (5 V)	4.7	50
Ag/$CsPbBr_3$/Ag	Single crystal	6 (10 V)	13.6	73
Au/$MAPbI_3$/Au	Nano arrays	1.3×10^4 (5 V)	2.5×10^4	74
ITO/$MAPbI_3$/ITO*	Poly-film	1.6×10^3 (5 V)	2.5×10^3	75
ITO/$MAPbI_3$/ITO*	Poly-film	4×10^3 (5 V)	1.4×10^4	48
ITO/$CsPbBr_3$/ITO*	Nanosheets film	6×10^3 (3 V, 10 μW/cm^2)	1.5×10^4	51
ITO/$CsPbBr_3$/ITO*	Nanosheets film	7×10^4 (3 V, 200 nW/cm^2)	2×10^5	51
Au/$CsPbBr_3$/Au	Monocrystalline film	4.6×10^5 (2 V, 8.8 μW/cm^2)	**1.2×10^6**	This work
Au/$CsPbBr_3$/Au	Monocrystalline film	3.31×10^6 (2 V, 40 nW/cm^2)	**8.7×10^6**	This work

These devices use transparent ITO electrodes while only the device channel area is accounted for light absorption. The material covered by the transparent ITO electrodes may also participate in light absorption, leading to a possible underestimation of the light absorption area and overestimation of the photocurrent gain.

The achievement of reliable vdW contacts down to base temperature allows us to conduct magnetoresistance (MR) studies and probe the quantum transport properties in the perovskite materials for the first time (Figure 4.12(a)). At T = 3.5 K, the device shows a negative MR at a low field, which switches to a positive MR at higher field. The higher resistance at zero field can be attributed to a quantum interference induced weak localization effect: the constructive interference of backscattered electronic wave functions increases the probability of localizing an electron and hence a higher resistance at zero magnetic field[76]. While the presence of magnetic field breaks phase coherence and such interference effect, leading to a reduced resistance and negative MR. This feature becomes less significant with increasing temperature and disappears above 20 K, as the phase coherence length l_φ becomes comparable to the mean free path l_μ .

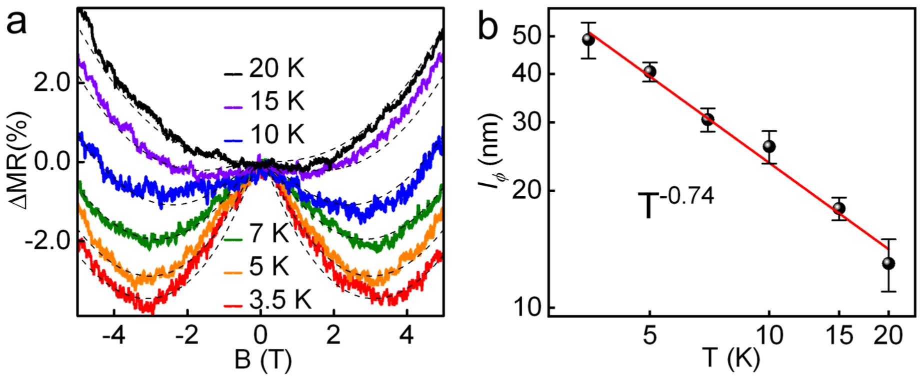

Figure 4.12. Magnetoresistance at the lowest temperatures. (a) Weak localization signal from 20 K to 3.5 K, $\Delta MR=(R_{xx}-R_{xx,B=0T})/R_{xx,B=0T}$. The dashed lines are fitting at each temperature; (b) Phase coherence length as a function of temperature. Red line is the linear fit.

Based on the MR data, we can extract phase coherence length l_φ at each temperature using the following equations[77-79] :

$$\Delta\mathrm{MR}\% = -\alpha\rho_0 \frac{e^2}{2\pi^2\hbar}\sqrt{\frac{eB}{\hbar}F(x)}+\beta B^2 \qquad (12)$$

Where e is the electronic charge, ρ_0 is the zero-field resistivity, ħ is the reduced Planck constant, α is a fitting parameter due to Coulomb screening, the last term βB^2 is a correction of magnetoresistance due to the bulk contribution, and F(x) is the Hurwitz zeta function, which can be expressed as:

$$F(x) = \sum_{n=0}^{\infty}[2\left(n+1+\frac{1}{x}\right)^{\frac{1}{2}} - 2\left(n+\frac{1}{x}\right)^{\frac{1}{2}} - \left(n+\frac{1}{2}+\frac{1}{x}\right)^{-\frac{1}{2}}] \qquad (13)$$

And

$$x = \frac{4el_\varphi^2}{\hbar} \qquad (14)$$

Here we obtain β at 20 K where WL contribution to the MR is suppressed and fix the value of β through all the temperature range. By tuning the value of x and α, we can obtain the best fitting of ΔMR%. The l_φ at each temperature then can be derived from the corresponding x.

We obtained a phase coherence l_φ of 49 nm and 12 nm length at 3.5 K and 20 K, respectively (**Figure 4.12(b)**). Remarkably, we found those length scales are comparable to those of the covalent 2D semiconductors such as black phosphorus or InSe at a similar carrier density, suggesting electronic quality of the ionic "soft-lattice" perovskites are nearly comparable to the high quality 2D semiconductors**.** The linear fit in log-log plot of the phase coherence l_φ vs. temperature follows $l_\varphi \sim T^{-0.74}$, in good agreement with the localization theory in 3D system (where a -0.75 power law dependence is expected[77]) and indicating carrier-carrier interaction dominates the phase coherence behavior. However, in our measurement regime, we didn't observe the weak anti-localization effect predicted in perovskite material[80]. It is likely that the spin orbital coherence length l_{so} is always greater than l_φ throughout our measurement regime. Additional quantum transport studies at lower temperature would be an interesting topic to explore for this unique class of material systems. Although similar weak localization behavior has been observed in more conventional covalent semiconductors, our study presents the first observation of such phenomenon in the "soft-lattice" halide perovskites, which are substantially different from conventional covalent semiconductors. This observation will certainly inspire critical new thinking about how quantum phenomena develops in such material systems.

4.4. Conclusion

Together, by preparing ultra-smooth large-area monocrystalline $CsPbBr_3$ thin films and creating high quality vdW-integrated electrical contacts, we have conducted systematic transport studies to probe the intrinsic carrier and photocarrier dynamics in lead halide perovskites. Robust Hall measurements conducted in standard Hall bar devices reveal a record-high mobility of 2080 cm^2/Vs observed in perovskite thin films to date. Furthermore, magnetotransport studies reveal a weak localization effect with a phase coherence length up to 49 nm at 3.5 K, comparable to those of high quality covalent 2D semiconductors. The robust observation of high Hall mobility and quantum interference induced weak localization effect in "soft-lattice" ionic halide perovskites is exciting, and suggests perovskites as a unique material platform for the fundamental transport studies and exploration of new physics beyond conventional covalent semiconductors. The damage-free integration of metal contacts on delicate halide perovskites may be extended for creating other functional contacts (e.g., ferromagnetic or superconducting metal contact) with highly transparent interface and enable probing other exotic properties in halide perovskites. Beyond high performance photovoltaics and LEDs, halide perovskites have also been suggested to exhibit many other attractive attributes. For example, optical spectroscopic studies of hybrid halide perovskites have revealed a giant Rashba splitting with the largest Rashba spin-orbit coupling parameter (11±4 eVÅ) among all known semiconductors[81], which could promise high performance spintronic device, such as the spin-orbital torque device or spin transistors, and could substitute the traditional material with strong Rashba field like heavy metal and topological insulator (< 4 eVÅ)[78]. However, despite the exciting prospects from optical studies, the relevant transport studies to date have been largely plagued by poor contacts. The ability to make high quality contacts is critical for reliable spin transport studies to fully unlock the potential of this unique class of materials, and thus opening up an exciting new chapter for halide perovskites beyond current focus on photovoltaics and LEDs. Lastly, this vdW-integration approach is also generally applicable for various delicate materials, including organic crystals and molecular monolayers. The ability to make high performance contacts on such delicate materials will open up exciting opportunities to fully unlock the potential of these unconventional electronic materials for both the fundamental studies and high-performance devices.

4.5. References

1. Kojima, A.; Teshima, K.; Shirai, Y.; Miyasaka, T. *J. Am. Chem. Soc.* **2009,** *131*, 6050-6051.

2. Lee, M. M.; Teuscher, J.; Miyasaka, T.; Murakami, T. N.; Snaith, H. J. *Science* **2012**, 643-647.

3. Burschka, J.; Pellet, N.; Moon, S.-J.; Humphry-Baker, R.; Gao, P.; Nazeeruddin, M. K.; Grätzel, M. *Nature* **2013,** *499*, 316-319.

4. Nie, W.; Tsai, H.; Asadpour, R.; Blancon, J.-C.; Neukirch, A. J.; Gupta, G.; Crochet, J. J.; Chhowalla, M.; Tretiak, S.; Alam, M. A. *Science* **2015,** *347*, 522-525.

5. Yang, W. S.; Noh, J. H.; Jeon, N. J.; Kim, Y. C.; Ryu, S.; Seo, J.; Seok, S. I. *Science* **2015,** *348*, 1234-1237.

6. Tsai, H.; Nie, W.; Blancon, J.-C.; Stoumpos, C. C.; Asadpour, R.; Harutyunyan, B.; Neukirch, A. J.; Verduzco, R.; Crochet, J. J.; Tretiak, S. *Nature* **2016,** *536*, 312-316.

7. Bush, K. A.; Palmstrom, A. F.; Zhengshan, J. Y.; Boccard, M.; Cheacharoen, R.; Mailoa, J. P.; McMeekin, D. P.; Hoye, R. L.; Bailie, C. D.; Leijtens, T. *Nat. Energy* **2017,** *2*, 17009.

8. Yang, W. S.; Park, B.-W.; Jung, E. H.; Jeon, N. J.; Kim, Y. C.; Lee, D. U.; Shin, S. S.; Seo, J.; Kim, E. K.; Noh, J. H. *Science* **2017,** *356*, 1376-1379.

9. Dong, Q.; Fang, Y.; Shao, Y.; Mulligan, P.; Qiu, J.; Cao, L.; Huang, J. *Science* **2015,** *347*, 967-970.

10. Zhou, H.; Chen, Q.; Li, G.; Luo, S.; Song, T.-b.; Duan, H.-S.; Hong, Z.; You, J.; Liu, Y.; Yang, Y. *Science* **2014,** *345*, 542-546.

11. Peng, W.; Wang, L.; Murali, B.; Ho, K. T.; Bera, A.; Cho, N.; Kang, C. F.; Burlakov, V. M.; Pan, J.; Sinatra, L. *Adv. Mater.* **2016,** *28*, 3383-3390.

12. Chen, Z.; Dong, Q.; Liu, Y.; Bao, C.; Fang, Y.; Lin, Y.; Tang, S.; Wang, Q.; Xiao, X.; Bai, Y. *Nat. Commun.* **2017,** *8*, 1890.

13. Luo, D.; Yang, W.; Wang, Z.; Sadhanala, A.; Hu, Q.; Su, R.; Shivanna, R.; Trindade, G. F.; Watts, J. F.; Xu, Z. *Science* **2018,** *360*, 1442-1446.

14. Jena, A. K.; Kulkarni, A.; Miyasaka, T. *Chem. Rev.* **2019,** *5*, 3036-3103.

15. Cao, Y.; Wang, N.; Tian, H.; Guo, J.; Wei, Y.; Chen, H.; Miao, Y.; Zou, W.; Pan, K.; He, Y. *Nature* **2018,** *562*, 249.

16. Abdi-Jalebi, M.; Andaji-Garmaroudi, Z.; Cacovich, S.; Stavrakas, C.; Philippe, B.; Richter, J. M.; Alsari, M.; Booker, E. P.; Hutter, E. M.; Pearson, A. J. *Nature* **2018,** *555*, 497.

17. Zhu, H.; Fu, Y.; Meng, F.; Wu, X.; Gong, Z.; Ding, Q.; Gustafsson, M. V.; Trinh, M. T.; Jin, S.; Zhu, X. *Nat. Mater.* **2015,** *14*, 636.

18. Luo, J.; Wang, X.; Li, S.; Liu, J.; Guo, Y.; Niu, G.; Yao, L.; Fu, Y.; Gao, L.; Dong, Q. *Nature* **2018,** *563*, 541.

19. Xing, J.; Zhao, Y.; Askerka, M.; Quan, L. N.; Gong, X.; Zhao, W.; Zhao, J.; Tan, H.; Long, G.; Gao, L. *Nat. Commun.* **2018,** *9*, 3541.

20. Leng, K.; Abdelwahab, I.; Verzhbitskiy, I.; Telychko, M.; Chu, L.; Fu, W.; Chi, X.; Guo, N.; Chen, Z.; Chen, Z. *Nat. Mater.* **2018,** *17*, 908-914

21. Fu, Y.; Zhu, H.; Chen, J.; Hautzinger, M. P.; Zhu, X.-Y.; Jin, S. *Nat. Rev. Mater.* **2019,** *4*, 169-188.

22. Wei, H.; Fang, Y.; Mulligan, P.; Chuirazzi, W.; Fang, H.-H.; Wang, C.; Ecker, B. R.; Gao, Y.; Loi, M. A.; Cao, L. *Nat. Photonics* **2016,** *10*, 333-339.

23. Fang, Y.; Dong, Q.; Shao, Y.; Yuan, Y.; Huang, J. *Nat. Photonics* **2015,** *9*, 679-686.

24. Yang, Z.; Deng, Y.; Zhang, X.; Wang, S.; Chen, H.; Yang, S.; Khurgin, J.; Fang, N. X.; Zhang, X.; Ma, R. *Adv. Mater.* **2018,** *30*, 1704333.

25. He, Y.; Matei, L.; Jung, H. J.; McCall, K. M.; Chen, M.; Stoumpos, C. C.; Liu, Z.; Peters, J. A.; Chung, D. Y.; Wessels, B. W. *Nat. Commun.* **2018,** *9*, 1609.

26. Zan, R.; Ramasse, Q. M.; Jalil, R.; Georgiou, T.; Bangert, U.; Novoselov, K. S. *ACS Nano* **2013,** *7*, 10167-10174.

27. Spicer, W.; Chye, P.; Garner, C.; Lindau, I.; Pianetta, P. *Surf. Sci.* **1979,** *86*, 763-788.

28. Haick, H.; Niitsoo, O.; Ghabboun, J.; Cahen, D. *J. Phys. Chem. C* **2007,** *111*, 2318-2329.

29. Haick, H.; Ambrico, M.; Ghabboun, J.; Ligonzo, T.; Cahen, D. *Phys. Chem. Chem. Phys.* **2004,** *6*, 4538-4541.

30. Mott, N. F.; Gurney, R. W., *Electronic processes in ionic crystals*. 1940.

31. Murgatroyd, P. *J. Phys. D* **1970,** *3*, 151-156.

32. Mark, P.; Helfrich, W. *J. Appl. Phys.* **1962,** *33*, 205-215.

33. Herz, L. M. *ACS Energy Lett.* **2017,** *2*, 1539-1548.

34. Manser, J. S.; Kamat, P. V. *Nat. Photonics* **2014,** *8*, 737-743.

35. Guo, D.; Bartesaghi, D.; Wei, H.; Hutter, E. M.; Huang, J.; Savenije, T. J. *J. Phys. Chem. Lett.* **2017,** *8*, 4258-4263.

36. Umansky, V.; Heiblum, M.; Levinson, Y.; Smet, J.; Nübler, J.; Dolev, M. *J. Cryst. Growth.* **2009,** *311*, 1658-1661.

37. Green, M. A. *J. Appl. Phys.* **1990,** *67*, 2944-2954.

38. Putley, E.; Mitchell, W. *Proc. Phys. Soc.* **1958,** *72*, 193-200.

39. Chen, Y.; Yi, H.; Wu, X.; Haroldson, R.; Gartstein, Y.; Rodionov, Y.; Tikhonov, K.; Zakhidov, A.; Zhu, X.-Y.; Podzorov, V. *Nat. Commun.* **2016,** *7*, 12253.

40. Yi, H. T.; Wu, X.; Zhu, X.; Podzorov, V. *Adv. Mater.* **2016,** *28*, 6509-6514.

41. Padovani, F.; Stratton, R. *Solid-State Electron.* **1966,** *9*, 695-707.

42. Sze, S. M.; Ng, K. K., *Physics of semiconductor devices*. John wiley & sons: 2006.

43. Liu, Y.; Guo, J.; Zhu, E.; Liao, L.; Lee, S.-J.; Ding, M.; Shakir, I.; Gambin, V.; Huang, Y.; Duan, X. *Nature* **2018,** *557*, 696-700.

44. Liu, Y.; Huang, Y.; Duan, X. *Nature* **2019,** *567*, 323-333.

45. Du, Y.; Neal, A. T.; Zhou, H.; Peide, D. Y. *2D Materials* **2016,** *3*, 024003.

46. Zeng, J.; Liang, S.-J.; Gao, A.; Wang, Y.; Pan, C.; Wu, C.; Liu, E.; Zhang, L.; Cao, T.; Liu, X. *Phys. Rev. B* **2018,** *98*, 125414.

47. Shi, D.; Adinolfi, V.; Comin, R.; Yuan, M.; Alarousu, E.; Buin, A.; Chen, Y.; Hoogland, S.; Rothenberger, A.; Katsiev, K. *Science* **2015,** *347*, 519-522.

48. Saidaminov, M. I.; Adinolfi, V.; Comin, R.; Abdelhady, A. L.; Peng, W.; Dursun, I.; Yuan, M.; Hoogland, S.; Sargent, E. H.; Bakr, O. M. *Nat. Commun.* **2015,** *6*, 8724.

49. Yang, Z.; Xu, Q.; Wang, X.; Lu, J.; Wang, H.; Li, F.; Zhang, L.; Hu, G.; Pan, C. *Adv. Mater.* **2018,** *30*, 1802110.

50. Song, J.; Cui, Q.; Li, J.; Xu, J.; Wang, Y.; Xu, L.; Xue, J.; Dong, Y.; Tian, T.; Sun, H. *Adv. Opt. Mater.* **2017,** *5*, 1700157.

51. Yang, B.; Zhang, F.; Chen, J.; Yang, S.; Xia, X.; Pullerits, T.; Deng, W.; Han, K. *Adv. Mater.* **2017,** *29*, 1703758.

52. Li, D.; Wu, H.; Cheng, H.-C.; Wang, G.; Huang, Y.; Duan, X. *ACS Nano* **2016,** *10*, 6933-6941.

53. Miyata, K.; Atallah, T. L.; Zhu, X.-Y. *Sci. Adv.* **2017,** *3*, e1701469.

54. Guzelturk, B.; Belisle, R. A.; Smith, M. D.; Bruening, K.; Prasanna, R.; Yuan, Y.; Gopalan, V.; Tassone, C. J.; Karunadasa, H. I.; McGehee, M. D. *Adv. Mater.* **2018,** *30*, 1704737.

55. Oga, H.; Saeki, A.; Ogomi, Y.; Hayase, S.; Seki, S. *J. Am. Chem. Soc.* **2014,** *136*, 13818-13825.

56. Valverde-Chávez, D. A.; Ponseca, C. S.; Stoumpos, C. C.; Yartsev, A.; Kanatzidis, M. G.; Sundström, V.; Cooke, D. G. *Energy Environ. Sci.* **2015,** *8*, 3700-3707.

57. Eperon, G. E.; Stranks, S. D.; Menelaou, C.; Johnston, M. B.; Herz, L. M.; Snaith, H. *Energy Environ. Sci.* **2014,** *7*, 982-988.

58. Azarhoosh, P.; McKechnie, S.; Frost, J. M.; Walsh, A.; Van Schilfgaarde, M. *APL Mater.* **2016,** *4*, 091501.

59. Milot, R. L.; Eperon, G. E.; Snaith, H. J.; Johnston, M. B.; Herz, L. M. *Adv. Funct. Mater.* **2015,** *25*, 6218-6227.

60. Miyata, K.; Meggiolaro, D.; Trinh, M. T.; Joshi, P. P.; Mosconi, E.; Jones, S. C.; De Angelis, F.; Zhu, X.-Y. *Sci. Adv.* **2017,** *3*, e1701217.

61. Wehrenfennig, C.; Liu, M.; Snaith, H. J.; Johnston, M. B.; Herz, L. M. *Energy Environ. Sci.* **2014,** *7*, 2269-2275.

62. Gunawan, O.; Pae, S. R.; Bishop, D. M.; Lee, Y. S.; Virgus, Y.; Jeon, N. J.; Noh, J. H.; Shao, X.; Todorov, T.; Mitzi, D. *arXiv* **2018**, 1802.07910.

63. Hendry, E.; Koeberg, M.; Pijpers, J.; Bonn, M. *Phys. Rev. B* **2007,** *75*, 233202.

64. He, Y.; Galli, G. *Chem. Mater.* **2014,** *26*, 5394-5400.

65. Zhao, T.; Shi, W.; Xi, J.; Wang, D.; Shuai, Z. *Sci. Rep.* **2016,** *6*, 19968.

66. Wang, Y.; Zhang, Y.; Zhang, P.; Zhang, W. *Phys. Chem. Chem. Phys.* **2015,** *17*, 11516-11520.

67. Mante, P.-A.; Stoumpos, C. C.; Kanatzidis, M. G.; Yartsev, A. *Nat. Commun.* **2017,** *8*, 14398.

68. Zhang, M.; Zhang, X.; Huang, L.-Y.; Lin, H.-Q.; Lu, G. *Phys. Rev. B* **2017,** *96*, 195203.

69. Frost, J. M. *Phys. Rev. B* **2017,** *96*, 195202.

70. Song, J.; Xu, L.; Li, J.; Xue, J.; Dong, Y.; Li, X.; Zeng, H. *Adv. Mater.* **2016,** *28*, 4861-4869.

71. Li, X.; Yu, D.; Cao, F.; Gu, Y.; Wei, Y.; Wu, Y.; Song, J.; Zeng, H. *Adv. Funct. Mater.* **2016,** *26*, 5903-5912.

72. Xue, J.; Gu, Y.; Shan, Q.; Zou, Y.; Song, J.; Xu, L.; Dong, Y.; Li, J.; Zeng, H. *Angew. Chem. Int. Ed.* **2017,** *56*, 5232-5236.

73. Dirin, D. N.; Cherniukh, I.; Yakunin, S.; Shynkarenko, Y.; Kovalenko, M. V. *Chem. Mater.* **2016,** *28*, 8470-8474.

74. Deng, W.; Huang, L.; Xu, X.; Zhang, X.; Jin, X.; Lee, S.-T.; Jie, J. *Nano Lett.* **2017,** *17*, 2482-2489.

75. Saidaminov, M. I.; Haque, M. A.; Savoie, M.; Abdelhady, A. L.; Cho, N.; Dursun, I.; Buttner, U.; Alarousu, E.; Wu, T.; Bakr, O. M. *Adv. Mater.* **2016,** *28*, 8144-8149.

76. Ihn, T., *Semiconductor Nanostructures: Quantum states and electronic transport*. Oxford University Press: 2010.

77. Lee, P. A.; Ramakrishnan, T. *Rev. Mod. Phys.* **1985,** *57*, 287.

78. Likovich, E. M.; Russell, K. J.; Petersen, E. W.; Narayanamurti, V. *Phys. Rev. B* **2009,** *80*, 245318.

79. Kawabata, A. *J. Phys. Soc. Jpn.* **1980,** *49*, 628-637.

80. Kepenekian, M.; Even, J. *J. Phys. Chem. Lett.* **2017,** *8*, 3362-3370.

81. Niesner, D.; Wilhelm, M.; Levchuk, I.; Osvet, A.; Shrestha, S.; Batentschuk, M.; Brabec, C.; Fauster, T. *Phys. Rev. Lett.* **2016,** *117*, 126401.

Chapter 5. Conclusion

Here we have presented a single-step vapor phase synthesis developed to prepare single-crystalline $CsPbX_3$ microplates, which is the starting point of this dissertation. High quality squared microplates with a smooth surface were produced with an edge length on the order of 10 μm and thickness around 1 μm. PL images and spectroscopic studies showed excellent optical properties with uniform and intense blue, green, and red emissions for $CsPbCl_3$, $CsPbBr_3$, and $CsPbI_3$, respectively. Owing to the high optical quality, the squared microplate structure with a smooth surface can function as an excellent optical whispering gallery mode cavity with a quality factor up to 2,863 to support laser emission at room temperature. Lastly, we demonstrated that such microplates can be readily grown on a variety of substrates, including silicon, graphene, and other 2D materials such as MoS_2, readily allowing the construction of heterostructure optoelectronic devices, including a graphene/perovskite/graphene vertical stack photodetector with a high photoresponsivity $> 10^5$ A/W (corresponding to a gain of 3.9×10^5). The extraordinary optical properties of $CsPbX_3$ microplates, combined with their ability to be grown on diverse materials to form functional heterostructures, could lead to exciting opportunities for broad optoelectronic applications. The vapor phase deposition method could be expanded to the growth of cesium lead halides with different cation or anion compositions and fully tunable optical and electronic properties. Other lead-free all-inorganic perovskites may also be prepared using a single-step vapor phase deposition approach.

Taking a step forward, we also expanded the vapor phase synthesis to the deposition of large-scale epitaxial growth of monocrystalline $CsPbBr_3$ thin film with an improved stability towards moisture and heat. The deposition of $CsPbBr_3$ on muscovite was demonstrated as epitaxial growth with X-ray diffraction and electron diffraction characterization. I also presented highly aligned micro-crystal domains nucleating initially on muscovite, forming oriented microplates, which can further grow and eventually merge into a large-area monocrystalline $CsPbBr_3$ thin film with excellent optical quality. Possessing two-dimensional morphology, the as-grown film provides a critical platform for the device fabrication. Furthermore, we show the $CsPbBr_3$ thin film could be readily converted into $CsPbI_3$ through an anion exchange approach. By using the standard electron beam lithography to enable the selective anion-exchange, we demonstrate $CsPbBr_3$/$CsPbI_3$ heterojunction can be produced with arbitrary geometry by design. The capability to grow the monocrystalline $CsPbBr_3$ thin film in a large area and conduct the selective anion-exchange to produce well-defined heterostructures provides a powerful platform for the fundamental investigations on the intrinsic properties of perovskite materials and opens up exciting opportunities to develop optoelectronic devices on the basis of perovskite heterostructures such as LED illumination, displaying and lasering.

To further probe the intrinsic properties of metal halide perovskites, we created high quality vdW-integrated electrical contacts with the ultra-smooth large-area monocrystalline $CsPbBr_3$ thin films. Systematic transport studies to probe the intrinsic carrier and photocarrier dynamics in lead halide perovskites have been conducted with the vdW contacts. Robust Hall measurements conducted in standard Hall bar devices reveal a record-high mobility of 2080 cm^2/Vs observed in perovskite thin films to date. Furthermore, a weak localization effect with a phase coherence length up to 49 nm at 3.5 K, comparable to those of high quality covalent 2D semiconductors has been revealed with magnetotransport studies. The robust observation of high Hall mobility and quantum interference induced weak localization effect in “soft-lattice” ionic halide perovskites is exciting, and suggests perovskites as a unique material platform for the fundamental transport studies and exploration of new physics beyond conventional covalent semiconductors. The damage-free integration of metal contacts on delicate halide perovskites may be extended for creating other functional contacts (e.g., ferromagnetic or superconducting metal contact) with highly transparent interface and enable probing other exotic properties in halide perovskites. Beyond high performance photovoltaics and LEDs, halide perovskites have also been suggested to exhibit many other attractive attributes. For example, optical spectroscopic studies of hybrid halide perovskites have revealed a giant Rashba splitting with the largest Rashba spin-orbit coupling parameter among all known semiconductors, which could promise high performance spintronic device, such as the spin-orbital torque device or spin transistors, and could substitute the traditional material with strong Rashba field like heavy metal and topological insulator. However, despite the exciting prospects from optical studies, the relevant transport studies to date have been largely plagued by poor contacts. The ability to make high quality contacts is critical for reliable spin transport studies to fully unlock the potential of this unique class of materials, and thus opening up an exciting new chapter for halide perovskites beyond current focus on photovoltaics and LEDs. Lastly, this vdW-integration approach is also generally applicable for various delicate materials, including organic crystals and molecular monolayers. The ability to make high performance contacts on such delicate materials will open up exciting opportunities to fully unlock the potential of these unconventional electronic materials for both the fundamental studies and high-performance devices.